UNIVERSITY OF OKLAHOMA

GRADUATE COLLEGE

GRAY BOX DYNAMIC MODELING OF VAPOR COMPRESSION SYSTEMS FOR CONTROL OPTIMIZATION

A DISSERTATION

SUBMITTED TO THE GRADUATE FACULTY

in partial fulfillment of the requirements for the

Degree of

DOCTOR OF PHILOSOPHY

By

HAOPENG LIU
Norman, Oklahoma
2022

GRAY BOX DYNAMIC MODELING OF VAPOR COMPRESSION SYSTEMS FOR CONTROL OPTIMIZATION

A DISSERTATION APPROVED FOR THE
SCHOOL OF AEROSPACE AND MECHANICAL ENGINEERING

BY THE COMMITTEE CONSISTING OF

Dr. Jie Cai, Chair

Dr. Wilson Merchan-Merchan

Dr. Paul Moses

Dr. Hamidreza Shabgard

Acknowledgments

I would like to express my highest respect and sincere appreciation to my advisor Dr. Jie Cai who creates an excellent research environment and training platform that greatly improve my scientific research ability. Dr. Cai is knowledgeable and enthusiastic, always giving me tremendous supports, positive feedbacks and constant encouragements during my research exploring. Many problems have been solved after the creative and patient discussions with him which benefit my academic career greatly. Without his valuable guidance and insights, this work would not be completed.

I would also like to thank Dr. Wilson Merchan-Merchan, Dr. Paul Moses and Dr. Hamidreza Shabgard for serving on my advisory committee and providing helpful feedback and warm support.

I am also grateful for all faculties and staffs in aerospace and mechanical engineering department. I appreciate them for their assistance and support during my time at OU.

Special thanks to my dearest labmates, colleagues, it is their companionship that makes my PhD life an enjoyable experience and a lasting memory.

Thank all my family members for their understanding and support for me. Their selfless tolerance, care and dedication have always warmed me and inspired me to move forward. It is their love that makes me break through the difficulties in my life and move towards a better tomorrow.

Table of Contents

List of Figures

List of Tables

Abstract

Buildings account for 75% of electricity use in the U.S. and more than 24% of building electrical energy is consumed by vapor compression equipment, including air-conditioners, refrigerators/freezers and heat pumps. Dynamic modeling of vapor compression systems (VCS) is particularly important for developing and validating optimal control strategies to maximize the system efficiency and reliability. However, existing modeling techniques are rarely used in control practices because of the significant model development effort and requirement of high computational resources.

This dissertation presents an efficient and robust gray-box dynamic modeling approach for VCS to support control optimization. The presented methodology allows automated construction of data-driven VCS models with minimum training data and human inputs. The overall approach incorporates a multi-stage training procedure with separate estimation of the steady-state and dynamic model parameters along with a finite control volume scheme to achieve good model identifiability while ensuring adequate prediction accuracy. The training procedure consists of 1) identification of component sub-models from quasi-steady-state performance data, 2) system model integration through continuity equations between the various components and 3) fine tuning of thermal capacitances of the evaporator and condenser to capture the system dynamic responses. To improve model reliability, the modeling approach incorporates sensitivity analysis and de-correlating steps in a preconditioning procedure to avoid over-parameterization. The system-level training identifies the refrigerant charge that minimizes the steady-state simulation errors while the dynamic modeling stage transforms the established steady-state system model into a dynamic counterpart, in which the optimal thermal capacitances of the heat exchanger walls are identified to best reproduce system transient responses.

This hierarchical training procedure was validated through experimental tests of a

3-ton variable-speed heat pump and proved to be capable of accurately predicting the system steady-state and transient behaviors over a wide range of operating conditions. The developed gray box dynamic model has been utilized for three different control applications, namely digital feedback control stability analysis, improved superheat control during provision of fast load balancing services, and active charge management for efficiency enhancement.

In the first control application, the dynamic VCS model was leveraged for stability analysis of a digital Proportional Integral (PI) controller for superheat regulation, with a specific goal of determining a proper control execution time step to prolong the electronic expansion valve (EXV) lifetime while ensuring control stability. Linear system theory was applied to the gray-box model after linearization at given operating conditions to assess the feedback stability under different control execution time steps. Case study results showed that the stable control execution time step could change significantly, from 3 sec to 19 sec, as the operating conditions and control settings vary, and a proper selection of the execution time step is critical to ensure stable and reliable operations.

VCS loads can be used to attenuate fluctuations of renewable energy generation and mitigate the adverse impact on the electric grid reliability, which is often referred to as fast load balancing services. However, during fast load balancing control, maintaining a stable and non-zero superheat is a challenging task with traditional feedback controllers. In the second control application, the gray box dynamic model has been combined with a gain-scheduled feedforward and PI controller to mitigate the superheat disturbance caused by provision of fast load balancing service. Test results have shown that the proposed controller is effective in improving the superheat regulation performance for three load balancing scenarios, i.e., compressor speed step changes, frequency regulation and photovoltaic smoothing. The demonstrated performance gains include fast post-disturbance recovery of the superheat with the settling time shortened by 63% to 83%, complete avoidance of wet compression

and enhanced transient energy efficiency.

The third control application concerns active refrigerant charge management by using the accumulator as a refrigerant reservoir. The established gray box dynamic model has been combined with a nonlinear state observer to enable estimation of the refrigerant liquid level of accumulator in real-time from refrigerant pressure and temperature measurements, which are readily available in modern VCS. This virtual liquid level detection technique supports zero-superheat and dynamic charge control to maximize the system efficiency. Experimental tests have demonstrated the accuracy of the accumulator liquid level estimator and shown that the zero-superheat and active charge control strategy could improve the system efficiency by up to 10.5%.

Chapter 1: Introduction

Vapor compression system (VCS) models have been rarely used in control practices due to the following barriers: (1) traditional black-box models for VCS require large training data sets to ensure prediction accuracy, with data acquisition cost prohibitively high for engineering applications; (2) white-box modeling approach assumes complex mathematical descriptions and require significant computational resources and engineering efforts for model development; (3) design of optimal VCS controllers calls for reliable dynamic models that can capture system transient behaviors but the high computational burden has limited their real-time applications such as controls; (4) calibration of dynamic models with field data is particularly challenging due to its numerical complexity.

This dissertation aims to address the aforementioned issues through development of a robust gray-box VCS dynamic modeling methodology. Towards this goal, the following unique contributions are made:

- Integration of sensitivity analysis and de-correlating steps prior to model training to ensure model identifiability and accommodate applications with limited training data;
- Proposal of gray-box models for the major components of a VCS including evaporator, condenser, compressor and expansion valve;
- Development of a hierarchical model training procedure that achieves separate identification of the component steady-state models, the system steady-state model and the system dynamic model.

Applications of the developed gray-box model in control optimization include stability

analysis of digital feedback controllers, superheat control strategies for disturbance mitigation during provision of fast load balancing services, and active refrigerant charge management.

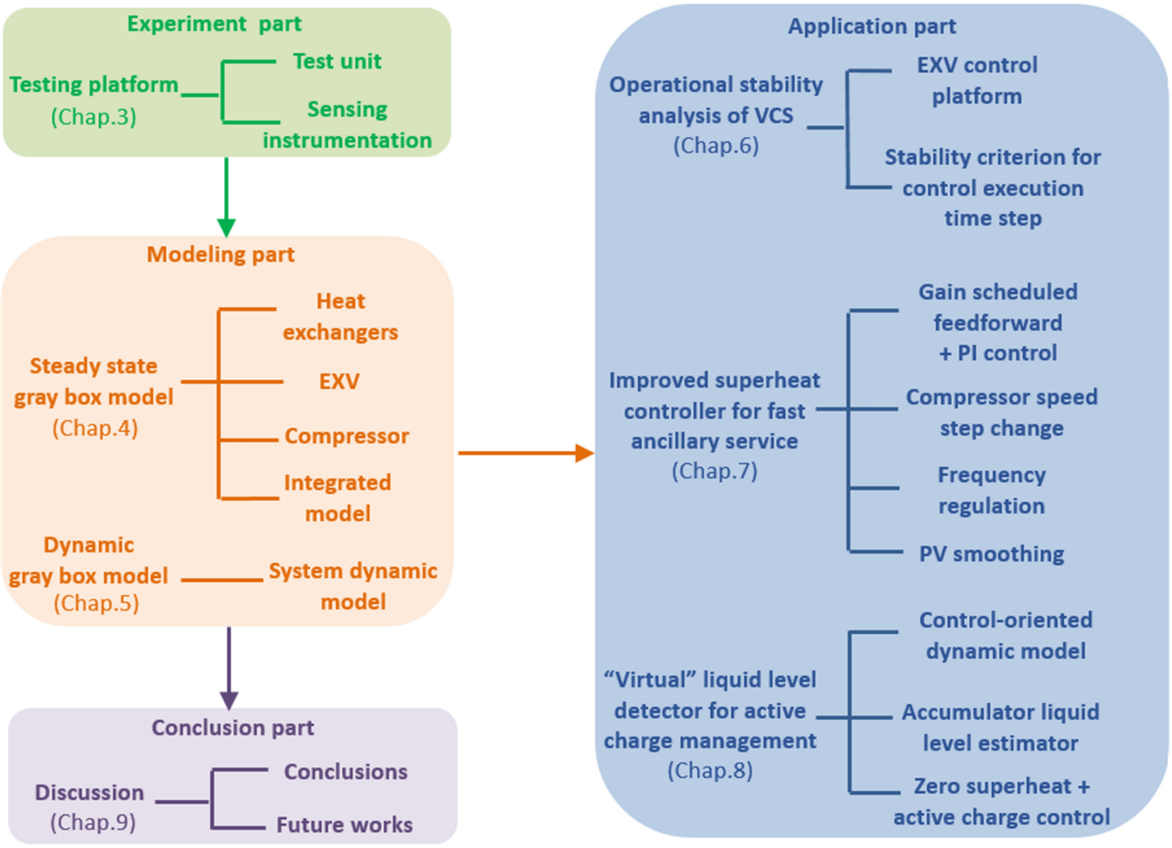

Figure 1.1: A tree diagram for the structure of this dissertation.

Figure 1.1 shows the overall structure of the dissertation, which begins with the description of an experimental platform for a 3-ton variable-speed heat pump in Chapter 3. This test rig has been extensively used throughout my Ph.D. work supporting the development and validation of the modeling and control methodologies. Then, a dual stage steady-state model training scheme is elaborated in Chapter 4, where the component models are identified separately, and then integrated through continuity constraints to establish a system model trained on a higher level. Chapter 5 describes the multi-stage dynamic VCS modeling methodology that transforms the developed steady-state system model into a dynamic one described by

state-space governing equations. Chapter 6 presents the application of the developed VCS dynamic model for digital control analysis, with a specific focus on the determination of proper control execution time step. Chapter 7 starts with an introduction of fast load balancing control of VCS equipment and reports the superheat control issue that was observed in previous experiments. Then it presents a new gain scheduled feed-forward and feedback control strategy, to attenuate the disturbance effect associated with sudden compressor speed changes during provision of fast balancing services. Chapter 8 focuses on the development of a “virtual" accumulator liquid level detection method, which combines the control-oriented dynamic model of evaporator and accumulator with a nonlinear state observer, to enable the zero-superheat and active charge management. Concluding remarks and future work are discussed in Chapter 9.

Chapter 2: Literature Review

A critical literature review on the modeling methodology of VCS and the control applications, including operational stability analysis, superheat regulation and active charge management, is presented in this chapter. The literature review is followed by a summary of research gaps that are to be addressed by the dissertation. The major outcome of the presented work is a robust gray-box VCS modeling toolkit that supports control algorithm development to enable optimized VCS operations and provision of fast ancillary services to the electric grid.

2.1 Steady-State VCS Modeling Methodology

White-box or physics-based models are commonly used to support optimized VCS design. Nevertheless, white-box models typically assume complex mathematical descriptions and require significant computational resources. Uncertainties in the model parameters very often result in degraded accuracy and reliability. Because of these drawbacks, the white-box approach is not appropriate for modeling of existing equipment and real-time model-assisted applications. Black-box models rely on pure empirical correlations to predict system behaviors and belong to the broader family of data-driven models. With minimum computing power requirements, black-box models are suitable for online applications such as optimized control and fault detection and diagnostics (FDD). The major issues for their practical implementations are the poor extrapolating performance and requirements of large training data sets. Lack of interpretability raises reliability concerns and represents another technical barrier for real-world applications. Gray-box modeling approach, which combines

the underlying physics and empirical correlations derived from actual operation data, offers a variety of benefits including high computational efficiency, reduced engineering efforts for model development, improved reliability and reduced training data requirements.

A majority of previous work on data-driven modeling of VCS focused on characterization of system-level performance, such as cooling capacity and compressor power, under variable operating conditions. Gordon and Kim (1994)[1] proposed a linear correlation for predicting a chiller's coefficient of performance (COP) from the cooling load and saturated condensing/evaporating temperatures, over a wide range of operating conditions. To better capture nonlinear characteristics, Li and Braun (2002)[2] presented a hybrid modeling approach that combines a low-order polynomial with a general regression neural network to improve both the interpolating and extrapolating performance for prediction of rooftop air conditioners' COP and cooling capacity. Breuker and Braun (1998)[3] introduced a lookup table-based model in support of automated FDD; the model relates the critical temperatures (e.g. superheat and subcooling) to air side operating conditions (e.g. dry-bulb and wet-bulb temperatures) for fixed-speed direct expansion (DX) systems, which can then be used for detection of charge-related faults. Swider (2003)[4] conducted a comprehensive survey of regression-based steady-state models for VCS and presented performance comparison results of a range of modeling forms, including simple linear regression, multivariate polynomial, radial basis function neural network model, etc. These models were applied for prediction of a chiller's COP by using inputs that are readily known to operating engineers, such as chilled water and condensing water inlet temperatures. To capture other system characteristics in addition to COP, Cabello et al. (2005)[5] introduced a regression model that uses the refrigerant-side variables such as evaporating/condensing pressures and superheat, and returns the refrigerant mass flow rate, cooling capacity and compressor power consumption. Although system performance models are easy to implement and widely used for first-order estimation of energy efficiency, these models are typically designed for specific applications and are not suitable for general-purpose controls or FDD.

On the other hand, process oriented models are able to capture the underlying thermodynamics of VCS and thus, have much improved extrapolating performance. Process oriented models are typically established with two stages: component models are developed separately and then integrated together to build a complete system model through energy and mass balances. Process oriented models often appear in the form of gray-box models, where key correlation parameters are estimated from experimental data, publicly available catalog data or research articles. Previously developed gray-box process oriented models often utilized semi-empirical correlations for modeling of compressors and expansion valves but employed heat exchanger models of various forms and complexities. Yu and Chan (2006)[6] developed an air-cooled chiller model to facilitate identification of favorable operating conditions for improved energy efficiency. The heat exchangers were modeled based on a lumped approach, where a single control volume is assumed and the combined heat transfer coefficient (HTC) is linearly correlated with mass flow rates of refrigerant and air. Cai (2015)[7] developed a semi-empirical model for multi-stage DX systems with variable air volume for supervisory control optimization. The HTCs of the evaporator and condenser were correlated with the air flow rate in an exponential form and the key parameters were estimated from field data. Although the lumped method involves lower computing power, it can't capture the thermodynamic gradients in the flow directions and thus, is not able to provide accurate representations of heat transfer processes. Besides, the lumped method is not suitable for FDD applications where accurate prediction of superheat and subcooling is needed.

An improved version of the lumped parameter approach is the moving boundary (MB) method, in which the heat exchanger is divided into a few thermal regions defined by the refrigerant phase and a lumped analysis is applied to each region. The MB approach features a good tradeoff between accuracy and computational complexity. Built on top of the previous work (Browne and Bansal, 1998[8]) that utilized the lumped method for heat exchanger models, Browne and Bansal (2001)[9] developed a MB heat exchanger model in combination with semi-empirical compressor/expansion valve models for prediction of the chiller COP. Lee

and Yoo (2000)[10] demonstrated a modeling method to investigate the effects of condenser size and refrigerant charge on the performance of automobile air conditioning systems, where the refrigerant side HTC of condenser was obtained empirically with a MB scheme. Jabardo et al. (2002)[11] proposed an empirical form for the evaporator/condenser HTC based on the MB method, and the effects of operational parameters such as compressor speed and return air temperature on system cooling capacity and COP were experimentally investigated. Fu et al. (2002)[12] presented a chiller model with and without subcooled economizer in a wide range of operating conditions and design configurations to investigate whether the economizer can help increase the cooling capacity and COP, where the MB method was applied to obtain empirical correlations for the heat exchangers. Cheung and Braun (2013)[13] proposed gray-box models for different types of VCS using a two-stage bottom-up scheme: component models were developed separately, with MB forms for the evaporator and condenser, and then integrated through continuity constraints. The established model was able to capture system behaviors under a range of faulty operations. Although the MB method features improved accuracy compared to the lumped approach, averaging of the HTC and thermal properties in each phase region is still needed, representing a major source of model inaccuracy.

To achieve higher model accuracies, some studies resorted to the high-fidelity finite control volume approach. For example, Rossi (1995)[14] further broke down the heat exchangers into a number of segments and in each segment, the effectiveness-NTU method was applied where the HTC was estimated from data-driven correlations based on local thermal properties. To mitigate discontinuity of the HTC during phase transition, linear interpolation was applied to the HTC when the quality is less than 0.1 or greater than 0.9. Haberschill et al. (2002)[15] proposed a finite control volume model which regards each channel of a plate heat exchanger as a control volume with energy conservation applied for each segment. The study applied HTC interpolation for a wider range of quality to further improve the smoothness of model with the key parameters of the condenser HTC correlation experimentally identified.

Process oriented models typically require design parameters (e.g., fin pitch and thickness for fin-tube heat exchangers, compressor displacement volume), acquisition of which can be time consuming or impossible for existing systems with limited access to relevant components. When performance data is available, data-driven models can be established, which typically involve relatively complex correlations to capture the energy performance at variable control settings, e.g., performance curves for DX equipment utilized by EnergyPlus (Crawley et al., 2001[16]). To mitigate possible over-parameterization, a large training data set is often a necessity but the data acquisition cost can be prohibitively high.

2.2 Dynamic VCS Modeling Methodology

Given that the dynamics associated with the heat transfer processes in evaporators and condensers play a dominant role in the overall system transience, dynamic performance characterization of heat exchangers has been a primary focus of prior dynamic modeling efforts, especially on the two-phase flow dynamics which to a large extent affect the evolution of system pressures (Bendapudi and Braun, 2002[17], Rasmussen, 2012[18]). Catano et al. (2013)[19] proposed a lumped-parameter dynamic model of DX systems to facilitate development of gain scheduling controllers. The entire heat exchangers were assumed to operate under two-phase. Quasi-steady-state models were adopted for the compressor and EXV. Although the obtained model is computationally efficient with very few governing equations, the lumped approach results in low prediction accuracy and is not able to capture important dynamics, e.g., phase transition point oscillations at low superheat. Through division of a heat exchanger according to the different phase regimes, the MB method seeks to capture the major dynamics of multi-phase heat exchangers while preserving the simplicity of the lumped approach. For example, Chen and Deng (2006)[20] developed a MB-based dynamic model of variable-air-volume DX systems for control analysis, with an empirical heat transfer correlation for each phase regime of the heat exchangers. The nonlinear dy-

namic features such as hysteresis and dead band were also taken into consideration. The major drawback of the MB method lies on the numerical instability when a single phase region disappears or reappears; to resolve this issue, an improved version of the MB approach, termed switched MB, was proposed by Li and Alleyne (2010)[21], which switches between the two-region and one-region model forms for the evaporator by comparing the length of the single-phase region to a pre-determined threshold. Kim et al. (2021)[22] also proposed an approach that combines MB models with the fuzzy modeling technique to overcome the numerical challenges associated with mode switching. A natural extension of the MB approach is the finite control volume method that utilizes a larger number of control volumes to capture system dynamic characteristics at a higher granularity and thus, offers improved model accuracy. Kapadia et al. (2009)[23] presented a finite control volume model of DX air conditioning systems to predict system transient characteristics during system start-up. Beghi and Cecchinato (2009)[24] used a similar finite control volume model to assist design of an auto-tuned proportional-integral-derivative (PID) controller for EXV, where actuation constraints such as upper bound and hysteresis were accounted for explicitly.

2.3 VCS Operational Stability Analysis

Dynamic models have been successfully used for VCS operational stability analysis. Root causes of VCS instability can be classified into two groups: the first is associated with inherent characteristics of the two-phase flow in an evaporator or condenser and the second category corresponds to sensing delays (e.g., superheat measurement delays) and improper controller design. The first category is closely related to the concept of minimal stable superheat (MSS) theory , which was first introduced by Huelle (1967)[25] and has been extensively studied since then, e.g., Huelle (1972)[26], Chen et al. (2002, 2008)[27, 28]. The MSS is defined as a critical minimal superheat at which the VCS operation becomes unstable; this instability is caused by chattering of the refrigerant-to-tube wall heat transfer coefficient due

to mode changes between nucleate boiling and convective boiling. This characteristic is inherent to the evaporation heat transfer process and is not directly related to control actions. The latter category, i.e., control instability of VCS, has attracted significant research interests more recently, mainly driven by the popularization of EXVs and variable-speed drives. Relevant research work addressed the VCS control stability issues from different perspectives, e.g., the impact of the sensing bulb dynamics in a thermostatic expansion valve (TXV)-controlled VCS (Eames et al., 2014[29]), design of control gains (Xia and Deng, 2016[30]) and superheat nonlinearity exhibited under different operating conditions (Elliott and Rasmussen, 2010[31], Xia et al., 2019[32]). For example, Xia and Deng (2016)[30] investigated the influences of PI gain settings and superheat sensing dynamics on the operational stability of a DX system, using the Nyquist diagram. Both simulation and experimental results showed that a larger P or I gain would lead to a higher chance of system instability. In a follow-up study (Xia et al., 2019[32]), the authors investigated the effects of superheat sensor dynamics and operating conditions on the operational stability of a DX system, using a dynamic VCS model extended from the one developed by (Chen and Deng, 2006[20]) by adding a sub-model to capture the superheat sensor dynamics. It was found through simulation tests that the increase of the time constant of temperature sensor or the supply fan speed could provide larger stability margins.

2.4 Control Strategies for Superheat Regulation

There is rich literature on control algorithm design of EXV for evaporator superheat regulation. PID controllers are most commonly used for control of systems with moderate nonlinearity. To better handle plant nonlinearities, advanced control algorithms have been proposed that adapt the control policy with variable operational conditions. For example, Outtagarts and Lallemand (1997)[33] developed a PID controller with gain scheduling for evaporator superheat control. The transfer function of the EXV-evaporator system was es-

tablished from experimental data in a simple form of first-order system subject to time delays. A functional relationship was proposed to vary the PI gains with the evaporating temperature and compressor speed. Elliott et al. (2009)[34] and Elliott and Rasmussen (2010)[31] proposed a new design and controller of expansion valve that combines mechanical and electronic regulation mechanisms. The new device, named hybrid expansion valve (HEV), consists of an inner control loop relying on the diaphragm of a traditional TXV to regulate evaporator pressure and an outer loop that adjusts the desired pressure to control evaporator superheat. The pressure setpoint is adjusted by an additional spring driven by a stepper motor. The claimed advantages of the HEV include less actuation of the stepper motor and extremely fast response. The experimental results demonstrated the efficacy of the HEV in improving system stability compared to traditional TXV and EXV. In Chen et al. (2005)[35], the authors implemented a dual single-input single-output (SISO) control strategy for multi-evaporator air conditioners, to achieve individual room temperature control; the suction pressure is controlled by the compressor speed to modulate the cooling capacity and the EXV openings are controlled to regulate the room temperatures rather than superheat. A self-tuning fuzzy control algorithm was incorporated to modify the control gains with variable loads. Marcinichen et al. (2008)[36] applied a similar dual SISO control strategy to regulate the superheat and brine (secondary fluid) exit temperature, through modulating the expansion valve opening and compressor speed, respectively. In Orhan et al. (2010)[37], three different control algorithms, namely PI, fuzzy logic and artificial neural network (ANN), were compared for control of EXV and compressor speed of a chiller and the ANN controller was shown to provide better superheat regulation against sudden changes in load.

In the aforementioned work, superheat regulation was achieved by controlling the expansion valve only in the context of SISO control and did not explicitly consider the cross couplings between different control channels. Proper coordination between the valve opening, compressor speed and fan speed can provide optimal superheat regulation performance and improve the system's ability to withstand external disturbances. Multi-input multi-output

(MIMO) control techniques are readily available to serve this purpose. He et al. (1997)[38] presented a moving boundary model for characterizing the dynamics of a VCS. The model was used in deriving transfer function matrices via linearization of the model at nominal operation points, and the relative gain array was adopted to measure the interactions of different input-output pairs. The results revealed strong cross-couplings between inputs, such as valve opening and compressor speed, and outputs including evaporating pressure and superheat, which indicate the limitation of independent SISO control techniques. In a follow-on study by He et al. (1998)[39], a MIMO control strategy was developed for VCS to achieve more accurate load matching and superheat regulation. The MIMO controller was implemented in a residential air conditioner and compared with the SISO control through experiments. The results showed improved performance of the MIMO control in disturbance rejection and response acceleration. In Rasmussen and Alleyne (2009)[40], the authors proposed a MIMO gain-scheduled control strategy to achieve desired cooling capacity while ensuring an appropriate level of superheat. The obtained nonlinear controller calculates the control command as a weighted sum of the outputs of individual linear controllers corresponding to different operating conditions, with the weights determined by the Youla parameterization method (Niemann and Stroustrup, 1999[41]). The above-mentioned MIMO controllers treat the compressor speed as a controllable input rather than a disturbance and thus, cannot be directly used for disturbance mitigation control, although the transfer function matrices obtained as part of MIMO controller synthesis provide direct information of the disturbance effect.

In variable-speed VCS operations, the compressor speed may be dictated by other control objectives (e.g., evaporating pressure regulation or grid service provision) and its variation would become a disturbance for superheat control. Very few publications can be found addressing the disturbance effect of fluctuating compressor speed on superheat control. Somehow relevant, Michael et al. (2006)[42] proposed a superheat regulation strategy for automotive VCS that combines a feedforward controller and a traditional PI controller, to mitigate the disturbance effect arising from the variation of engine speed of a vehicle. The

feedforward transfer function was devised for a nominal operation point and the performance at other conditions was not discussed.

2.5 Dynamic Active Charge Management

The VCS energy efficiency is highly dependent on the refrigerant charge. Research studies have shown that over- or under-charging the system can reduce the system efficiency by as much as 16% (Choi and Kim, 2002[43], Farzad and O'Neal, 1994[44]). Relationships between the charge level and system COP were found to exhibit a concave curve with the peak COP occurring at an intermediate charge level (Kim and Braun, 2012[45]). Some studies focused on the charge impact on energy performance of miniature VCS commonly used for electronic device cooling, since they are much more sensitive to the refrigerant charge compared to regular VCS. Through parametric simulation tests, Wu and Du (2011)[46] found that both the charge level and length of the capillary tube affect the system COP of a miniature VCS. Yuan et al. (2015)[47] employed a similar parametric simulation-based approach for identification of the optimal charge level that results in the maximum COP at rated operating conditions.

The bulk of previous studies on refrigerant charge aimed to identify the optimal charge level of a VCS that can inform field technicians or manufacturers in determining how much refrigerant should be added to the system under the rated conditions. However, the VCS characteristics and thereby the optimal charge level vary with operating conditions, especially the outdoor temperature. If the active charge, defined as the total mass accumulated in the primary refrigeration circuit of a VCS (mainly the heat exchangers), can follow the dynamically varying optimal charge, the time-averaged system efficiency can be significantly enhanced. Dynamic active charge management can be achieved by proper control of the inlet conditions of refrigerant tanks, e.g. the high-side receiver or low-side accumulator,

which are commonly used in the VCS as a means of storing excess refrigerant and ensuring safe operations. Prior studies made attempts to use both the receiver and accumulator for dynamic active charge control. For example, Jensen and Skogestad (2007)[48] utilized the receiver at the outlet of the condenser to hold excess refrigerant and added an extra valve before the receiver to adjust the refrigerant liquid level therein and to achieve the desired subcooling. The study found that a subcooling of 5K could provide 2% COP improvement compared to a zero subcooling for the specific operating condition under study. Koeln and Alleyne (2014)[49] considered a similar system configuration and proposed two strategies for determination of the optimal active charge that maximizes the system COP. The first strategy identifies the subcooling corresponding to the optimal active charge using an offline simulation analysis and uses a PI controller to modulate the EXV upstream of the receiver to achieve the desired subcooling. The second strategy adopts the extreme seeking control (ESC) approach as an online model-free optimizer that directly drives the EXV opening to the COP maximizing point. The latter strategy is suitable for practical implementations as it allows online control optimization of systems with unknown dynamics. However, the dither signal used by the ESC results in constant actuation of the EXV which can significantly impact its lifespan. Both simulation and experimental tests showed that a 9% improvement in the system efficiency could be achieved compared to a conventional operation strategy with zero subcooling. These studies proved the effectiveness of using receivers for active charge management. The dual EXV design allows simultaneous control of the superheat and subcooling which can offer ample performance enhancement. However, only subcooling was controlled in the aforementioned studies.

The dynamics of the low-pressure accumulator and its use for charge management have also been studied. Eldredge et al. (2008)[50] established a dynamic model for the evaporator and accumulator set using the moving-boundary approach, targeting dynamic control and stability analysis. Kim and Braun (2012)[45] added accumulators in air conditioning and heat pump systems as a means to change the system active charge, allowing experimental

assessments of the impact of charge level on the system energy efficiency under different combinations of indoor and outdoor temperatures. It was found from the experimental results that refrigerant charge below 80% of its nominal level can cause significant reductions (approximately 15%) in the system COP, while an overcharge by 30% could reduce the COP by 10%. The nominal charge in Kim and Braun's study was from manufacturer recommendations, which was not necessarily equal to the optimal charge achieving the maximum COP. Very few publications can be found using accumulators for dynamic active charge control. The most relevant is the study by Menken et al. (2014)[51], which investigated the feasibility of modulating EXV to achieve dynamic charge control with an accumulator. Experimental tests were conducted in which the EXV was actuated to vary the subcooling and active charge by storing excess liquid refrigerant in the accumulator. However, the accumulator liquid level was not monitored during the experiments. The study also compared the effectiveness of accumulator and receiver control for active charge management. The advantage of utilizing accumulators for active charge control over the use of receivers is that the zero-superheat condition is automatically satisfied when the active charge control is enabled, which affords the maximum efficiency boost. For a receiver-equipped VCS, simultaneous charge and superheat control would require a secondary EXV; even when two EXVs are available, the superheat cannot be set too low as the system suffers from a higher risk of wet compression without the buffering zone provided by an accumulator.

2.6 Chapter Summary

From a thorough review of the literature, an efficient and robust gray-box VCS modeling method is lacking but can bring significant benefits in operational efficiency and reliability. Further, there has been limited research efforts in model-assisted VCS control development. This dissertation fills the void by presenting a gray-box dynamic modeling methodology for VCS to facilitate operational stability analysis and control algorithm de-

velopment to enable optimized operations. A hierarchical training procedure is proposed with separate estimation of the steady-state and dynamic model parameters along with a finite control volume scheme to ensure model identifiability and accuracy. The established dynamic model has been successfully applied in addressing control problems arising from several emerging VCS technologies, including disturbance mitigation for provision of fast load balancing services and active charge management in variable-speed equipment.

Chapter 3: Experimental Platform for Validation of the Modeling and Control Methods

This chapter introduces the experimental rig and the test unit used for development and validation of the modeling and control algorithms presented in this dissertation.

The test unit, depicted in Figure 3.1, is a variable speed split DX system with a rated cooling capacity of 3 tons. The split system has an indoor unit and an outdoor unit. The outdoor unit houses a variable-speed scroll compressor, a condenser coil and a condenser fan. The indoor unit packages an A-shaped evaporator coil, an Electronically Commutated Motor (ECM)-driven supply fan and an EXV. The gas and liquid lines connecting the indoor and outdoor units are both approximately 20' long. The indoor unit is connected to an indoor environment test loop (see Figure 3.2), which is available to accommodate flexible load testing with control accuracies of $\pm 0.2^{\circ}$C for dry bulb temperature and $\pm 0.5\%$ for relative humidity. The outdoor unit is placed in a psychrometric chamber (see Figure 3.3), which can reproduce a wide range of outdoor environmental conditions with identical control accuracies to those of the indoor test loop.

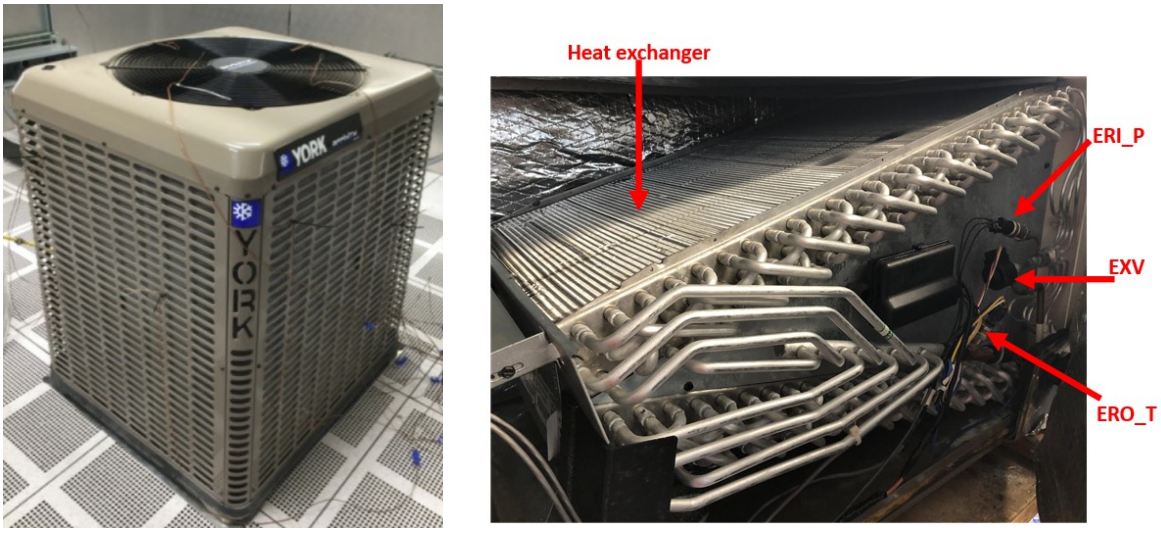

(a) (b)

Figure 3.1: Variable speed DX system. (a) Outdoor unit. (b) Indoor unit.

Figure 3.2: Indoor environment test loop.

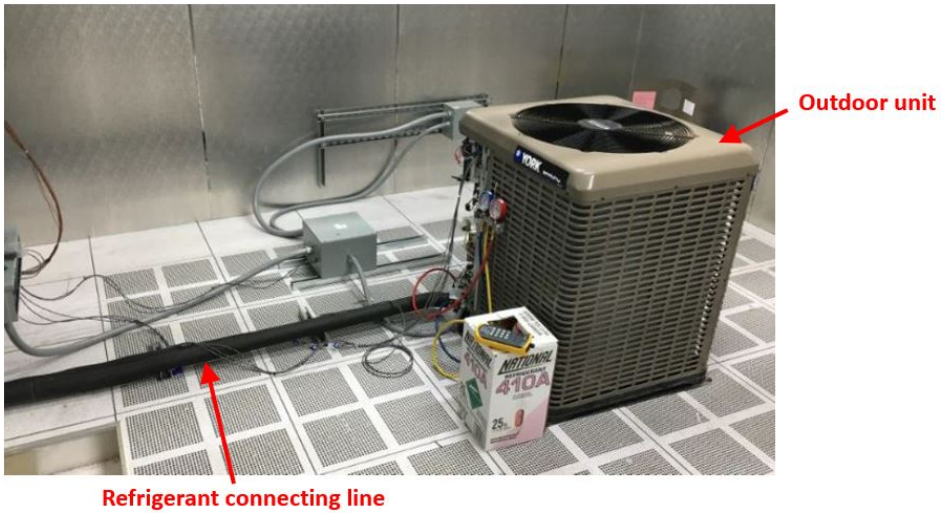

Figure 3.3: Psychometric test chamber with the outdoor unit inside.

The overall schematic diagram of the chamber and load test rig is shown in Figure 3.4. The test chamber is built with 6" thick polyurethane insulation panels with a combined R-value of 26, which can accommodate testing environments of -20°C to 60°C. The chamber environmental control is achieved through a variable-speed 18-ton medium-temperature refrigeration system combined with solid state relay (SSR)-controlled electrical heater and humidifier. A National Instruments CompactRIO controller is used with fine tuned PID blocks for accurate temperature and humidity control. Similarly, the indoor load test loop is comprised of a closed-loop duct that houses SSR-controlled heater and humidifier to simulate indoor sensible and latent loads.

Figure 3.5 shows a schematic diagram of the sensing instrumentation for the test DX system. The system consists of a single vapor compression circuit with R410A as the working fluid. Sensors have been installed to measure key operation variables such as pressures, temperatures, volumetric and mass flow rates, and power consumption. In Figure 3.5, letters 'E' and 'C' indicate the sensors for the evaporator and condenser, respectively; 'I' and 'O' indicate the inlet and outlet of a heat exchanger, respectively; 'R' and 'A' represent the refrigerant- and air-side measurements. 'T' and 'P' represent the temperature measure-

ment via thermocouples and pressure transducers, respectively. 'RH' stands for the relative humidity. Three power meters are available to monitor real-time power usage of the compressor, condenser fan and supply fan. Detailed sensor information and technical parameters are presented in Table 3.1.

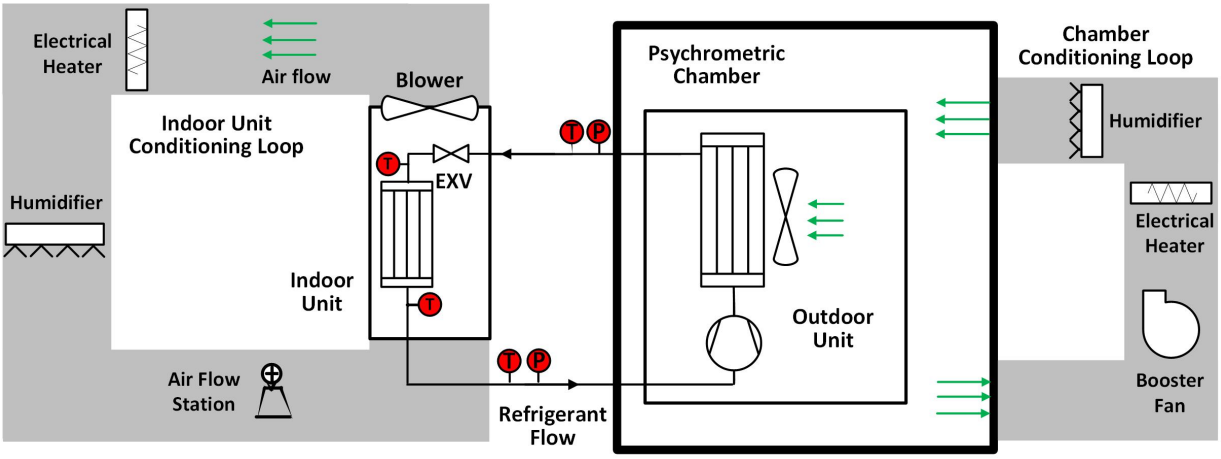

Figure 3.4: Overall schematic diagram of the chamber and load test rig.

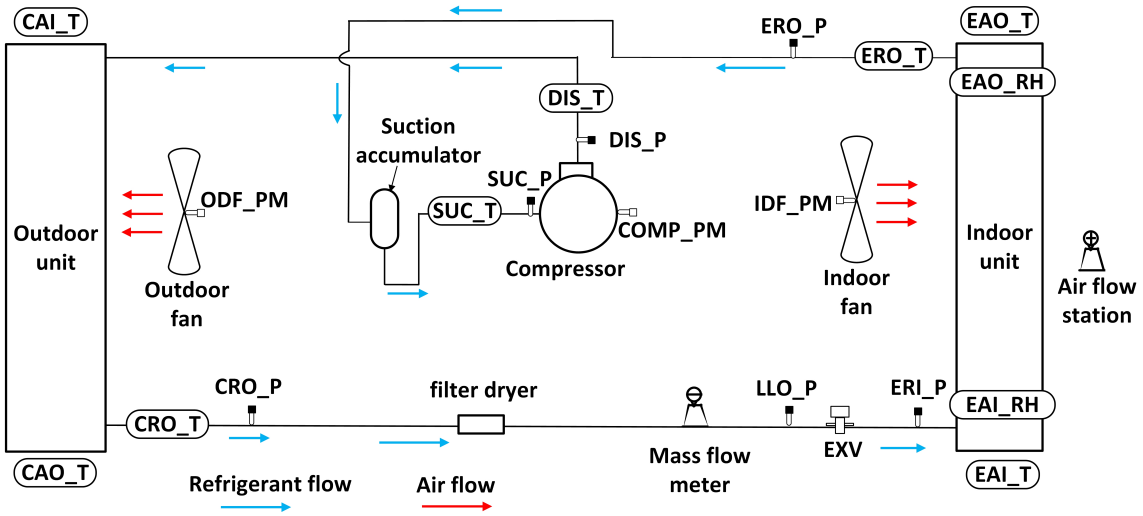

Figure 3.5: Test unit sensor instrumentation diagram.

Table 3.1: Sensor names and uncertainties

Measurement point	**Sensor type/ model number**	**Sensor/ model name in Figure 3.5**	**Notes**
Indoor/ outdoor fan power	Ohio Semitronics PC5-011C	IDF_PM/ ODF_PM	Uncertainty: ±0.5%
Compressor power	Ohio Semitronics PC5-113C	COMP_PM	Uncertainty: ±0.5%
Condensation/ evaporation pressure	Honeywell Piezoresistive pressure transducer	CRO_P, LLO_P, DIS_P/ SUC_P, ERO_P, ERI_P	Range: 0 ∼ 500 psi/ 0 ∼ 300 psi. Uncertainty: ±0.25% full scale pressure
Condensation/ evaporation temperature	Omega Type-T thermocouple	CRO_T, DIS_T/ ERO_T, SUC_T	Uncertainty: ±0.5°C
Return/ supply air temperature	Omega Type-T thermocouple	CAI_T, EAI_T/ CAO_T, EAO_T	Uncertainty: ±0.5°C
Return/ supply relative humidity	Vaisala Capacitive thin film polymer HMD70Y	EAI_RH/ EAO_RH	Uncertainty: ±2%
Supply air flow	Ebtron GTC116-P	-	Uncertainty: ±2% airflow ±0.08°C temperature
Refrigerant flow	Micromotion Coriolis mass flow meter R025S1113UR	-	Uncertainty: ±0.5%
Superheat	-	-	Uncertainty: ±0.51°C
COP	-	-	Uncertainty: ±0.0548

Note that both the superheat and COP are derivative variables. The superheat is derived from the refrigerant pressure and temperature measurements at the evaporator outlet and its uncertainty was calculated based on the two sensor uncertainties in combination with the refrigerant thermal property routine, i.e., CoolProp, which was used in estimation of the

partial derivative of the saturated evaporation temperature with respect to the evaporation pressure. The COP, on the other hand, is obtained from the sensors for refrigerant flow, condensation/evaporation temperature and pressure, as well as the compressor power meter; the COP uncertainty was calculated by aggregating all the sensors' uncertainties in combination with the CoolProp.

Chapter 4: Steady State Modeling of VCS

In this chapter, a gray-box steady-state modeling methodology for variable-speed DX systems is presented. The methodology incorporates a dual-stage training scheme, where component models are identified separately, and then integrated through continuity constraints to establish a system model trained on a higher hierarchy. To further improve model reliability and robustness, the training methodology incorporates two commissioning techniques, i.e., significance ranking and de-correlation, to down-select the estimation parameters according to the quality of the training data. To demonstrate the efficacy, the proposed modeling methodology was applied to the test heat pump introduced in Chapter 3. Qualities of the identified models were evaluated in terms of parameter accuracy and model prediction accuracy against variable training data sizes.

4.1 Parameter Reduction Algorithm

To mitigate potential over-parametrization issues for cases with limited training data, preconditioning of the parameter set is often required, such as down-selection and de-correlation of estimation parameters. This section describes two sequential techniques for parameter reduction to improve the computational efficiency of the training process and model identifiability.

A system simulation model has the following generic form:

$$y_i(\boldsymbol{\theta}) = F\left(\mathbf{U}_i, \boldsymbol{\theta}\right) + \varepsilon_i(\boldsymbol{\theta}) = \hat{y}_i(\boldsymbol{\theta}) + \varepsilon_i(\boldsymbol{\theta}), 1 \leq i \leq N \tag{4.1}$$

where $y_i(\boldsymbol{\theta})$ is the measured output for the i^{th} data point, $\hat{y}_i(\boldsymbol{\theta})$ or $F(\mathbf{U}_i, \boldsymbol{\theta})$ is the predicted output by the model, $\boldsymbol{\theta}$ is the vector of estimation parameters of dimension p, $\mathbf{U}$ is the collection of input variables to the model, N is the number of data points in the training data, and $\varepsilon_i(\boldsymbol{\theta})$ is the model prediction error. The model can be written in a compact matrix form of

$$\mathbf{y}(\boldsymbol{\theta}) = \hat{\mathbf{y}}(\boldsymbol{\theta}) + \mathbf{e}(\boldsymbol{\theta}) \tag{4.2}$$

where $\mathbf{y}(\boldsymbol{\theta})$ and $\hat{\mathbf{y}}(\boldsymbol{\theta})$ are vectors of observed and simulated outputs, respectively, and $\mathbf{e}(\boldsymbol{\theta})$ is the vector of model errors.

Defining

$$\mathbf{J}(\boldsymbol{\theta}) = \frac{\partial}{\partial \boldsymbol{\theta}}(\hat{\mathbf{y}}(\boldsymbol{\theta})) \tag{4.3}$$

$$\mathbf{M}(\boldsymbol{\theta}) = \mathbf{J}^{\mathsf{T}}(\boldsymbol{\theta})\mathbf{J}(\boldsymbol{\theta}) \tag{4.4}$$

where $\mathbf{J}$ is the Jacobian matrix of the model output with respect to the parameter vector and is thus called sensitivity matrix. The matrix $\mathbf{M}$, termed information matrix, approximates the Fisher information matrix up to a scalar when the parameter values are close to the ground truth. For unbiased estimators, this information matrix is also commonly used to approximate the inverse of the parameter covariance matrix, up to a scalar.

Since the parameters may have quite different scales, normalization is needed for the various parameters to account for the scaling effects and the normalized version of the information matrix is

$$\mathbf{M}_n(\boldsymbol{\theta}) = Diag(\boldsymbol{\theta})(\mathbf{J}^{\mathrm{T}}(\boldsymbol{\theta})\mathbf{J}(\boldsymbol{\theta}))Diag(\boldsymbol{\theta}) \tag{4.5}$$

where $Diag(\boldsymbol{\theta})$ represents the diagonal matrix constructed from the vector $\boldsymbol{\theta}$.

Define the significance vector as

$$\mathbf{s}(\boldsymbol{\theta}) = (\mathbf{M}_n(\boldsymbol{\theta}))_{jj}^{0.5} \tag{4.6}$$

where the operator $(.)_{jj}$ returns the diagonal elements of a given matrix and indicates the significance level for the j^{th} parameter in the model output. For linear regression (Kutner et al., 2005[52]), the square of the significance value is inversely proportional to the confidence interval of a specific parameter. An intuitive interpretation of the significance value is the root mean square of the difference in the model outputs when a specific parameter is perturbed by a given percentage. Therefore, a higher value of s_j indicates higher sensitivity and significance and corresponds to a smaller confidence interval for the j^{th} parameter.

Although the regression problem dealt with in this dissertation is nonlinear, linear regression theory is still applicable locally in the region close to the solution. The Working–Hotelling procedure can be applied to calculate the confidence region for parameter vector $\boldsymbol{\theta}$ for a confidence level $1 - \alpha$: (Donaldson et al., 1987[53])

$$(\boldsymbol{\theta} - \hat{\boldsymbol{\theta}})^{\mathrm{T}}(\mathbf{V}(\hat{\boldsymbol{\theta}}))^{-1}(\boldsymbol{\theta} - \hat{\boldsymbol{\theta}}) \leq pF_{p,N-p,1-\alpha} \tag{4.7}$$

where $\mathbf{V}(\hat{\boldsymbol{\theta}})$ is the parameter covariance matrix and $\hat{\boldsymbol{\theta}}$ is the ground truth parameter values (or best estimate). Since the Fisher information matrix $\mathbf{M}_F$ can be expressed as (Cai et al., 2016[54])

$$\mathbf{M}_F(\hat{\boldsymbol{\theta}}) = \tau Diag(\hat{\boldsymbol{\theta}})(\mathbf{J}^{\mathrm{T}}(\hat{\boldsymbol{\theta}})\mathbf{J}(\hat{\boldsymbol{\theta}}))Diag(\hat{\boldsymbol{\theta}}) = \tau\mathbf{M}_n(\hat{\boldsymbol{\theta}}) \tag{4.8}$$

where τ has a functional relationship with the probability distribution function of the model error ε. The Cramer-Rao inequality states that the inverse of the Fisher information matrix $\mathbf{M}_F$ lower bounds the parameter covariance matrix $\mathbf{V}(\hat{\boldsymbol{\theta}})$. For efficient estimators (e.g., maximum likelihood estimator or least-square estimator with Gaussian errors), the lower bound

would become tight and the following relationship between covariance matrix and normalized information matrix $\mathbf{M}_n$ can be obtained (Ljung, 1999[55])

$$\mathbf{V}(\hat{\boldsymbol{\theta}}) = \tau^{-1}(\mathbf{M}_n(\hat{\boldsymbol{\theta}}))^{-1} \tag{4.9}$$

Therefore, the confidence interval for an individual parameter can then be calculated as

$$\left|\theta_j - \hat{\theta}_j\right| \leq (\mathbf{V}(\hat{\boldsymbol{\theta}}))_{jj}^{0.5} t_{N-p,1-\frac{\alpha}{2}} = \tau^{-0.5}(\mathbf{s}_j(\hat{\boldsymbol{\theta}}))^{-1} t_{N-p,1-\frac{\alpha}{2}}, 1 \leq j \leq p \tag{4.10}$$

where $t_{N-p,1-\frac{\alpha}{2}}$ denotes the t distribution with the dimension of $N-p$ at confidence level $1-\frac{\alpha}{2}$, $\mathbf{s}_j$ is the significance value of the j^{th} parameter. From Equation 4.10, it can be concluded that a higher significance value indicates a smaller confidence interval for the corresponding parameter. Therefore, down-selection of estimation parameters can be done by eliminating those having low significance.

It may be noted that a large significance only indicates that the corresponding parameter is influential when it is estimated as the only estimation parameter. When estimation is carried out with other parameters, correlations could exist across multiple parameters. If a parameter is strongly correlated with others, its influence to the system characteristics can be represented by linear combinations of the correlated ones; estimation of correlated parameters could be ill-conditioned and cause deteriorated model accuracy. De-correlation is a critical step for further parameter reduction and improving the reliability of the estimated model.

A principal component analysis (PCA)-based approach (Cai et al., 2014[56]) was adopted to identify the highly correlated parameters. The method can be implemented with the following steps:

- Calculate the normalized information matrix $\mathbf{M}_n$ in Equation 4.5.

- Find the minimum eigenvalue and the corresponding eigenvector $\mathbf{v}$ of $\mathbf{M}_n$; then the maximum entry and the associated index k are located; the k^{th} parameter has the highest correlation with others and should be removed from the parameter set.
- Remove the k^{th} row and column of $\mathbf{M}_n$.
- Stop if the condition number of $\mathbf{M}_n$ is smaller than a pre-defined threshold; otherwise repeat step 2 with the reduced $\mathbf{M}_n$.

The steps can be carried out iteratively to find the most correlated parameters one by one, and the termination condition used in this dissertation is whether the condition number of the reduced information matrix $\mathbf{M}_n$ is below certain threshold.

The underlying principle of the de-correlation step is illustrated in Figure 4.1 for a simple case with two parameters. For this case, the confidence region is a 2-dimensional ellipse, the shape of which is characterized by the information matrix $\mathbf{M}_n$ as shown in Equation 4.7, where $\hat{\theta}_1$ and $\hat{\theta}_2$ indicate the estimated parameter values. Define $\Delta\boldsymbol{\theta} = \boldsymbol{\theta} - \hat{\boldsymbol{\theta}}$, and then the left hand side of Equation 4.7 would become $\Delta\boldsymbol{\theta}^{\mathrm{T}}\mathbf{M}_n\Delta\boldsymbol{\theta}$. Note that the eigenvalue decomposition of $\mathbf{M}_n$ is

$$\mathbf{M}_n = [\mathbf{e_1}\ \mathbf{e}_2] \begin{bmatrix} \lambda_1 & 0 \\ 0 & \lambda_2 \end{bmatrix} \begin{bmatrix} \mathbf{e}_1^{\mathrm{T}} \\ \mathbf{e}_2^{\mathrm{T}} \end{bmatrix} \tag{4.11}$$

where λ_1 and λ_2 are the eigenvalues and $\mathbf{e_1}$ and $\mathbf{e_2}$ are the corresponding eigenvectors. Then the characterization equation for the eclipse becomes

$$\begin{aligned} \Delta\boldsymbol{\theta}^{\mathrm{T}}[\mathbf{e_1}\ \mathbf{e}_2] \begin{bmatrix} \lambda_1 & 0 \\ 0 & \lambda_2 \end{bmatrix} \begin{bmatrix} \mathbf{e}_1^{\mathrm{T}} \\ \mathbf{e}_2^{\mathrm{T}} \end{bmatrix} \Delta\boldsymbol{\theta} &= \lambda_1 \Delta\boldsymbol{\theta}^{\mathrm{T}}\mathbf{e_1}\mathbf{e_1}^{\mathrm{T}}\Delta\boldsymbol{\theta} + \lambda_2 \Delta\boldsymbol{\theta}^{\mathrm{T}}\mathbf{e_2}\mathbf{e_2}^{\mathrm{T}}\Delta\boldsymbol{\theta} \\ &= \frac{(\mathbf{e_1}^{\mathrm{T}}\Delta\boldsymbol{\theta})^2}{(1/\sqrt{\lambda_1})^2} + \frac{(\mathbf{e_2}^{\mathrm{T}}\Delta\boldsymbol{\theta})^2}{(1/\sqrt{\lambda_2})^2} \end{aligned} \tag{4.12}$$

It is evident that the eigenvectors $\mathbf{e_1}$ and $\mathbf{e_2}$ provide the directions of the major and minor axes, whose lengths are $1/\sqrt{\lambda_1}$ and $1/\sqrt{\lambda_2}$. When the two eigenvalues differ significantly (i.e., a high condition number), the confidence region would become very skinny meaning the two parameters are highly correlated and the correlation is the strongest in the eigen-direction associated with the smaller eigenvalue (λ_1 in Figure 4.1). The parameter corresponding to the maximum entry of the dominant eigenvector (θ_2 in Figure 4.1) would have a larger confidence interval and lower identifiability and thereby needs to be removed from the estimation parameter pool to reduce the correlation. Removal of the highly correlated parameters does not affect the system behavior much since their influence to the model output can be captured by linear combinations of other parameters. When the eigenvalues of the information matrix are close to each other, the confidence region is close to a hyper-sphere meaning inter-parameter correlations are low and the de-correlation procedure can be terminated.

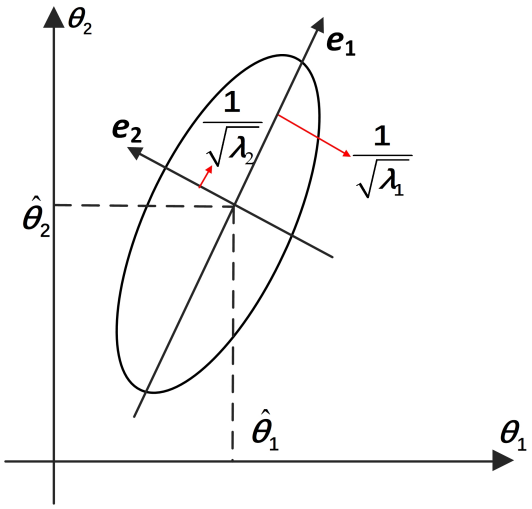

Figure 4.1: Confidence ellipse for two parameter estimation problems.

4.2 Methodology

Gray box models for the various components of a DX system are firstly presented. The models capture the underlying physics through heat and mass balances together with

empirical correlations whose parameters are trained with performance data obtained from experimental tests. High fidelity physics-based (white box) models are used to 1) derive simplified correlation forms for the gray box model, 2) analyze the structural identifiability and 3) identify the key influential parameters of the gray box model to be estimated in the training procedure. The identified component models are then integrated through continuity constraints to establish a complete system model.

Figure 4.2 shows a representative schematic of a vapor compression system and illustrates the modeling approach. The finite control volume method is utilized for modeling of the heat exchangers, where energy and mass balances are applied for each control volume to capture the heat transfer characteristics between the refrigerant and the overflowing air. The thermal status of refrigerant for each control volume is determined by comparing the local enthalpy with the saturated gas/liquid enthalpy, and appropriate heat transfer correlations are applied accordingly. A illustrative schematic of finite control volume method is shown in Figure 4.3.

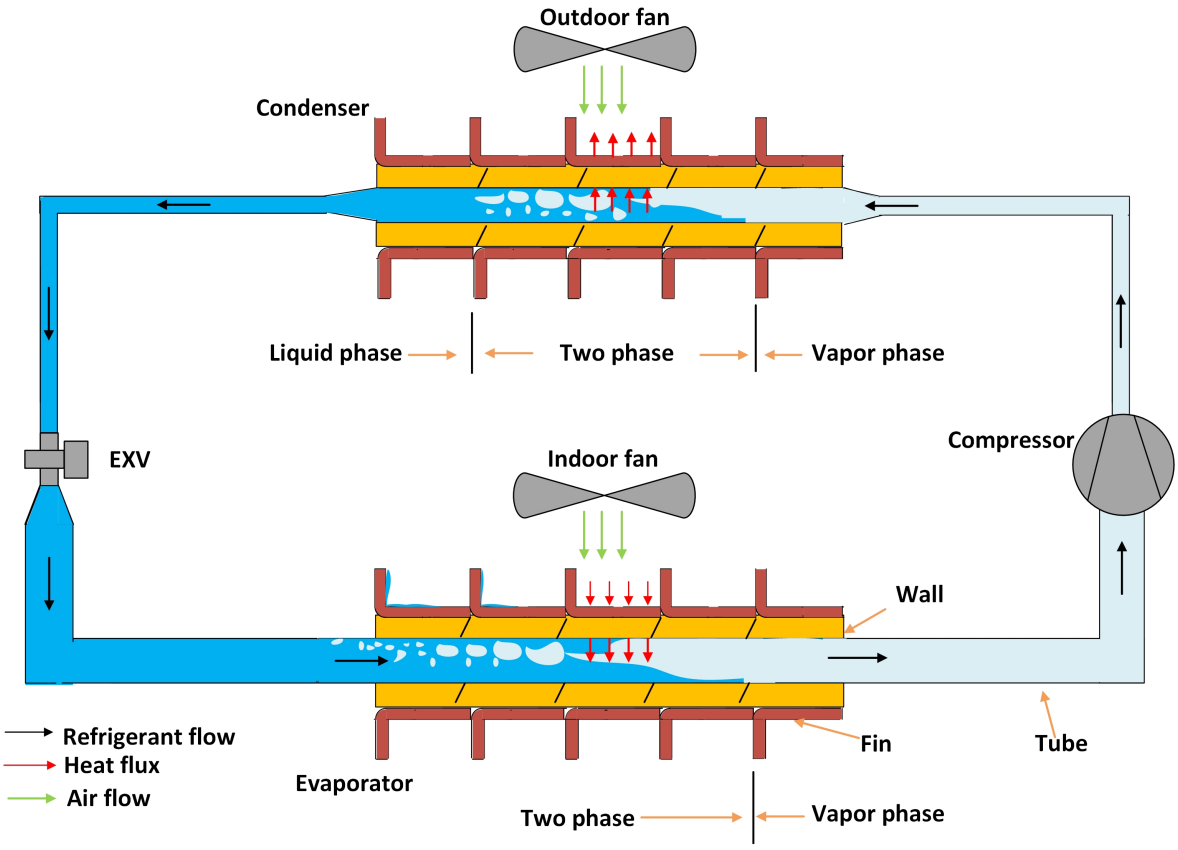

Figure 4.2: Schematic diagram for modeling of a vapor compression system.

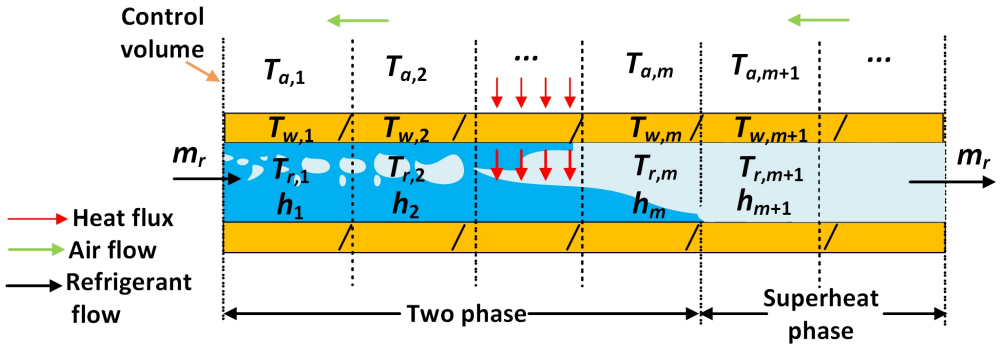

Figure 4.3: Schematic diagram for the finite control volume method adopted for modeling of the evaporator and condenser.

The following assumptions are made for the steady-state model of the system

- The EXV is not modeled explicitly; instead, the superheat is assumed to always match

the measured value, enforced by an equality constraint in the system integration process, and the expansion process is assumed to be isenthalpic.

- Refrigerant-side pressure drops are neglected for both the evaporator and condenser; the measured pressure drops in all the experimental tests were found to be less than 2.6% of the respective pressures.
- Counter-flow heat transfer is assumed for both heat exchangers; this is a reasonable assumption since the number of rows of tubes in the traverse direction for both evaporator and condenser is more than 3 (Belman et al., 2010[57]).
- Refrigerant inventory is constant, i.e., there is no refrigerant reservoir during steady-state operation.

For the m^{th} control volume, the following energy balance equation characterizes the heat exchange between the air and refrigerant:

$$\begin{aligned} Q_m = (\alpha_{r,m}A_{i,m})(T_{w,m} - T_{r,m}) &= (\alpha_{a,m}A_{o,m})(T_{a,m} - T_{w,m}) \\ &= m_r(h_m - h_{m-1}) = C_{p,a}m_a(T_{a,m+1} - T_{a,m}) \end{aligned} \tag{4.13}$$

where Q_m is the heat transfer rate, $\alpha_{r,m}$ and $\alpha_{a,m}$ represent the refrigerant- and air-side HTCs, respectively, $A_{i,m}$ and $A_{o,m}$ denote the inner and outer heat transfer areas, respectively, $T_{w,m}$, $T_{r,m}$ are tube wall and refrigerant temperatures, $T_{a,m+1}$ and $T_{a,m}$ are the air inlet and outlet temperatures, m_r and m_a are the mass flow rates of the refrigerant and air, and $C_{p,a}$ is the air specific heat. h_m is the refrigerant enthalpy of the m^{th} control volume, which is assumed to be identical across the whole control volume. Therefore, h_m can also be regarded as the outlet enthalpy of the m^{th} control volume and the corresponding refrigerant temperature ($T_{r,m}$) can be obtained using refrigerant thermal property calculation routines such as CoolProp (Bell and Jäger, 2014[58]).

The main unknowns in Equation 4.13 are the refrigerant- and air-side HTCs. The

gray box component models are to estimate the HTCs based on local operating conditions and the thermal properties; modeling details are elaborated in the following sections.

4.2.1 Evaporator

The correlation developed by Wang et al. (1997)[59] for wavy fin-and-tube heat exchangers is leveraged to derive a simplified correlation form to estimate the air side HTC. The Wang correlation is able to capture the effect of staggered arrangement of wavy fins and has the following form:

$$\alpha_{a,e} = \frac{N_u k_a}{D_c} \tag{4.14}$$

$$N_u = C_o Re_{D_c} Pr^{1/3} \tag{4.15}$$

where the subscript e stands for evaporator, Nu is the Nusselt number, k_a is the thermal conductivity of air, D_c is fin collar outside diameter, Re is Reynolds number and Pr is Prandtl number. C_o is the Colburn factor, which is a function of the air-side Reynolds number and geometric parameters of the evaporator coil, including the tube pitch in the traverse direction, fin thickness and density of fins. The detailed functional dependence of the Colburn factor on the coil geometries is omitted but can be found in Wang et al. (1997)[59]. Obtaining the coil geometric parameters needed for calculating the Colburn factor is a time consuming process and the obtained parameters are subject to high uncertainties. Considering that Re_{D_c} and Pr are strongly dependent on the air mass flow rate m_a and not very sensitive to temperature/humidity variations within the ranges of interest, a simplified exponential form is proposed to correlate the air side HTC and the mass flow rate

$$\alpha_{a,e} A_{o,e} = a_1 m_a^{a_2} \tag{4.16}$$

where a_1, a_2 are estimation parameters. For the air side heat exchange, I only consider the dry coil scenario in this dissertation since all experimental tests were conducted with low return air humidity. However, wet coil heat transfer characteristics can also be easily captured by establishing an empirical correlation of the Lewis number (Pirompugd et al., 2006[60]) from wet-coil experimental data in estimation of the mass transfer coefficient.

Tremendous efforts have been made in characterizing evaporation heat transfer processes for air-conditioning and refrigeration applications and the most widely studied HTC correlations include those proposed by Gungor and Winterton (1986)[61] , Shah (1982)[62] , Jung et al. (1989)[63] and Chen (1966)[64]. I have implemented and compared the aforementioned correlations for R410A and Figure 4.4 depicts the estimated evaporation HTCs with variable quality for fixed mass flux G_m and evaporation temperature T_e. In this dissertation, the Chen correlation is utilized considering that it considers both the effects of nucleate pool boiling and forced convection and doesn't require the calculation of the boiling number, which would involve iterative processes.

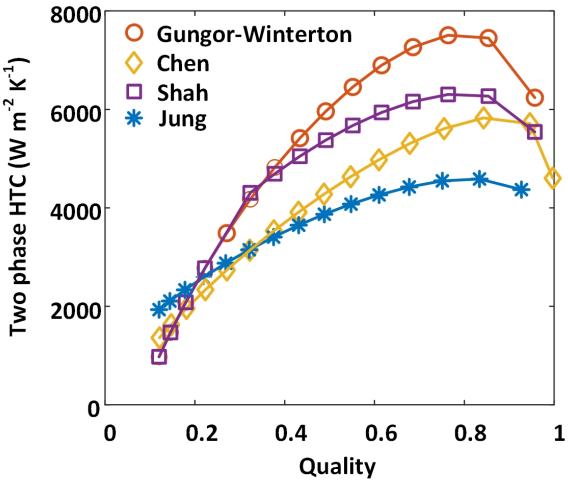

Figure 4.4: Comparisons of different correlations of evaporation HTC for $G_m = 1125\text{kg m}^{-2}\text{s}^{-1}$ and $T_e = 278\text{K}$.

The Chen correlation estimates the evaporation HTC based on the following equation

$$\alpha_{tp,e} = \alpha_{nb} + \alpha_{fc} = S\alpha_{fz} + F\alpha_{l,e} \tag{4.17}$$

where α_{nb} and α_{fc} are the HTCs associated with the nucleate boiling and forced convection, respectively. α_{fz} is the pool boiling HTC which can be calculated with the Forster-Zuber correlation.

$$\alpha_{fz} = 0.00122\left(\frac{k_l^{0.79}C_{p,l}^{0.45}\rho_l^{0.49}}{\sigma^{0.5}\mu_l^{0.29}h_{fg}^{0.24}\rho_g^{0.24}}\right)\Delta T_{sat}^{0.24}\Delta P_{sat}^{0.75} \tag{4.18}$$

where k_l is the liquid phase thermal conductivity, ρ_g and ρ_l are the gas and liquid phase refrigerant density, σ is the refrigerant surface tension, μ_l is the liquid-phase dynamic viscosity, h_{fg} is the latent heat of vaporization and $C_{p,l}$ is the liquid phase specific heat. ΔT_{sat} is the temperature difference of the inner tube wall (T_{wall}) and the refrigerant temperature (T_e). ΔP_{sat} is the difference of the saturated pressures evaluated at the inner tube wall and the refrigerant temperatures. For given saturated evaporating temperature and enthalpy, all the properties in Equation 4.18 can be obtained using CoolProp. S is the nucleate boiling suppression factor which is a function of Re_{tp}, the two phase Reynolds number:

$$S = \frac{1}{1 + 2.53\mathrm{e}^{-6}Re_{tp}^{1.17}} \tag{4.19}$$

The HTC contribution from forced convection (α_{fc}) is estimated based on the liquid phase convective HTC $\alpha_{l,e}$, using the turbulent flow correlation of Dittus-Boelter (Bergman et al., 2011[65]):

$$\alpha_{l,e} = 0.023Re_l^{0.8}Pr_l^{0.4}\frac{k_l}{D_i} \tag{4.20}$$

where D_i is the inner tube diameter. A correction factor F is needed to account for the heat

transfer enhancement due to vapor formation during the evaporation process

$$F = \left(\frac{1}{\chi_{tt}} + 0.213\right)^{0.736} \tag{4.21}$$

where χ_{tt} is the Martinelli parameter which is a function of the refrigerant quality q:

$$\chi_{tt} = \left(\frac{1-q}{q}\right)^{0.9} \left(\frac{\rho_g}{\rho_l}\right)^{0.5} \left(\frac{\mu_l}{\mu_g}\right)^{0.1} \tag{4.22}$$

where μ_g is the gas-phase dynamic viscosity.

Based on the above correlations, a simplified form, that is suitable for model identification and closely resembles those given in Equation 4.17 to Equation 4.22, is identified as shown in Equation 4.23, where θ_1 to θ_7 are parameters to be estimated in the training procedure:

$$\alpha_{tp,e} = \theta_1 T_e^{\theta_2} \Delta T_{sat}^{\theta_3} \left(\frac{1}{1 + \theta_4 Re_{tp}^{\theta_5}}\right) + \theta_6 \chi_{tt}^{\theta_7} \alpha_{l,e} \tag{4.23}$$

It may be noted that the nucleate boiling coefficient (α_{nb}) is mainly dependent on the saturated evaporating temperature (T_e), refrigerant-to-tube temperature difference (ΔT_{sat}) and two phase Reynolds number (Re_{tp}). The effect of the saturated pressure difference (ΔP_{sat}) on the nucleate boiling coefficient can be implicitly accounted for through the nonlinear dependence on ΔT_{sat}. Therefore, if the relationship between ΔP_{sat} and ΔT_{sat} is close to linear, the estimated value for parameter θ_3 should be close to 0.99, which is the sum of the exponents of ΔP_{sat} and ΔT_{sat} in Equation 4.18. The estimation of the forced convective coefficient is made from intermediate variables χ_{tt} and $\alpha_{l,e}$, which can be calculated from input variables such as the saturated temperature, refrigerant mass flow rate and quality. These functional relationships remain in the gray-box formulation to improve the identifiability of the model; further training processes could be used to capture these relationships from experimental data but would introduce more parameters to estimate and increase the requirement

of training data.

The two phase heat transfer dominates the total cooling effect of the evaporator and only a small fraction of heat exchange occurs in the superheated region. To ensure model identifiability, the gray-box model adopts the following Gnielinski correlation (Admiraal and Bullard, 1993 [66]) for the superheated phase directly, without any training:

$$\alpha_{sp,e} = \frac{k}{D_i} \frac{(f/8)(Re_{sp} - 1000)Pr_{sp}}{1 + 12.7(f/8)^{0.5}(Pr_{sp}^{2/3} - 1)} \tag{4.24}$$

where the thermal conductivity k, the Reynolds number Re_{sp} and Prandtl number Pr_{sp} are all defined in the superheated phase. This is a reasonable assumption considering the fact that the two-phase heat transfer rate contributes 88% to 94% of the total cooling capacity in all the collected experimental data. The friction factor f is calculated as

$$f = (0.79 \mathrm{In} Re_{sp} - 1.64)^{-2} \tag{4.25}$$

Refrigerant inventory strongly affects the operating pressures of a VCS. To estimate the amount of refrigerant residing in each control volume, the correlation by Tandon et al. (1985)[67] is adopted that estimates the void fraction α for a given quality q, the relationship of which is denoted by $\alpha = f_\alpha(q)$. The refrigerant mass in a two-phase control volume is calculated for a known tube volume V as:

$$m_t = V(\rho_g W_g + \rho_l(1 - W_g)) \tag{4.26}$$

$$W_g = \frac{\int_{q_i}^{q_o} f_\alpha(q)\mathrm{d}q}{q_o - q_i} \tag{4.27}$$

where W_g is refrigerant gas density weighting factor and q_o and q_i represent the inlet and outlet quality of each control volume.

4.2.2 *Condenser*

The condenser is also of a fin-and-tube type with wavy fins. Therefore, the air-side heat transfer correlation presented for the evaporator coil can be directly applied. However, unlike the evaporator coil that is subject to variable airflow, the condenser fan has a fixed speed. Therefore, the air-side HTC $\alpha_{a,c}$ can be identified as an individual estimation parameter.

Since the Shah correlation (Shah, 1979[68]) has shown satisfactory agreement with experimental results for a wide range of operating conditions, it is adopted in this dissertation to characterize the condensation HTC

$$\alpha_{tp,c} = \alpha_{l,c}\left[(1-q)^{0.8} + \frac{3.8q^{0.76}(1-q)^{0.04}}{P_R^{0.38}}\right] \tag{4.28}$$

where P_R is the reduced pressure, defined as the condensing pressure divided by the critical pressure, and $\alpha_{l,c}$ is the liquid phase convective HTC, which can be calculated using Equation 4.20.

It is worth noting that when the quality approaches zero in Equation 4.28, the condensation HTC converges to the liquid-phase HTC ($\alpha_{l,c}$); therefore, the Shah correlation guarantees a smooth transition of the HTC at the interface between the two-phase and subcooled regions. It is evident that the condensation HTC ($\alpha_{tp,c}$) is mainly dependent on the saturated condensing temperature (T_c), refrigerant quality (q) and liquid-phase HTC ($\alpha_{l,c}$) (note that the reduced pressure P_R can be uniquely determined for a given T_c). Therefore, the following simplified correlation is proposed to be used in the gray-box model to estimate the condensation HTC

$$\alpha_{tp,c} = \alpha_{l,c}\left[c_1(1-q)^{c_2} + c_3 q^{c_4} T_c^{c_5}\right] \tag{4.29}$$

where c_1 to c_5 are the estimation parameters. It may be noted that for the subcooled region, the estimation parameter c_1 serves as a correction factor for the liquid-phase HTC obtained via Equation 4.20. Therefore, the condenser model in Equation 4.29 captures the heat transfer characteristics for both the two-phase condensation and subcooled regions, which together play a dominant role in the total condenser heat; only a small fraction of heat exchange occurs in the desuperheated region, less than 15% for all the experimental data collected in this study. Therefore, similar to the evaporator case, the gray-box model applies the Gnielinski HTC correlation for the desuperheated region without any training.

4.2.3 Compressor

A compressor model is developed to estimate the refrigerant mass flow rate, discharge enthalpy and compressor power for given compressor speed and suction/discharge conditions. For a scroll compressor, it is a common practice to assume a volumetric efficiency of 100% (Stoecker, 1988[69]). Therefore, the refrigerant mass flow rate pumped by the compressor can be calculated by (Winandy et al., 2002[70])

$$m_r = \frac{V_s \cdot RPM}{60 v_{suc}} \tag{4.30}$$

where m_r is refrigerant mass flow rate, v_{suc} is the specific volume of refrigerant at the suction port, and V_s represents the swept volume of the compressor, which is the only parameter that needs to be estimated for the mass flow sub-model, and RPM (revolutions per minute) represents the compressor speed.

The electrical power input to the compressor has been modeled based on estimating the work necessary for a polytropic compression process as well as an efficiency term that includes the electric motor efficiency and other inefficiencies that occur inside a compressor, such as frictional effects. Equation 4.31 shows the power model (Reindl and Klein, 2000[71])

including this combined efficiency

$$Power \cdot (1 - f_{hl})\eta_{comb} = m_r(h_{dis} - h_{suc})\eta_{comb} = m_r \underbrace{\left\{ \frac{\lambda}{\lambda - 1} P_e v_{suc} \left[\left(\frac{P_c}{P_e} \right)^{\frac{\lambda-1}{\lambda}} - 1 \right] \right\}}_{\text{ideal isentropic gain}} \tag{4.31}$$

where h_{dis} and h_{suc} are discharge and suction enthalpy, respectively, λ is the specific heat ratio and f_{hl} is the heat loss ratio. The right-hand side of this equation provides the ideal isentropic/polytropic work and the term inside the curly brackets gives the refrigerant enthalpy gain for ideal compression. The study by Chen et al. (2000)[72] has shown that the combined efficiency η_{comb} has strong dependence on the pressure ratio $\frac{P_c}{P_e}$ (the ratio of the discharge pressure of a compressor to its suction pressure) and compressor speed RPM. Based on the experimental data collected in the present study, the following polynomial correlation is proposed

$$\eta_{comb} = d_1 + d_2 \text{In}\left(\frac{P_c}{P_e} \right) + d_3 RPM + d_4 \text{In}\left(\frac{P_c}{P_e} \right) \cdot RPM \tag{4.32}$$

where d_1 to d_4 are estimation parameters. The study by Willich and White (2017)[73] has found a close-to linear relationship between the heat loss ratio and compressor speed RPM. In addition, the ambient temperature T_a was found to be another influential variable. The following linear form is proposed to estimate the heat loss ratio

$$f_{hl} = e_1 + e_2 RPM + e_3 T_a \tag{4.33}$$

where e_1 to e_3 are coefficients to be estimated in the training process. The combined isentropic efficiency η_{comb} allows the calculation of the discharge enthalpy and the heat loss ratio can then be used to estimate the compressor power input.

4.2.4 Heat Gain in the Gas Line

For split systems having a long distance between the indoor and outdoor units, the low temperature refrigerant can absorb heat from the surrounding environment, which would offset a portion of the cooling effect. The test unit involved in this dissertation has the indoor and outdoor units about 3.4 meters apart. Although both the gas and liquid lines are insulated with 1.5" thick Armaflex, the heat gain from the evaporator output to the compressor suction port was found to be up to 3% of the total cooling capacity from the experimental data. Considering that the heat gain is mainly driven by the temperature difference between the refrigerant and the ambient, a bilinear form is adopted to capture this heat exchange

$$Q_{gain} = m_r(h_{suc} - h_{ero}) = f_1 + f_2 m_r + f_3(T_{cai} - T_{ero}) + f_4 m_r(T_{cai} - T_{ero}) \tag{4.34}$$

where T_{cai} and T_{ero} represent the temperatures of the condenser air inlet (ambient) and the evaporator refrigerant outlet, respectively, and f_1 to f_4 are the coefficients to be estimated.

4.2.5 Integrated Model

The component models described in the preceding sections are trained separately from experimental test data and are then coupled to establish an integrated gray-box model through continuity constraints, i.e., the outlet conditions of one component need to match the inlet conditions of the downstream component. The overall model integration diagram is shown in Figure 4.5, where h_{cro}, h_{ero} and h_{suc} are the refrigerant enthalpies at the condenser outlet, evaporator outlet and suction port of compressor. M_c and M_e represent the amounts of refrigerant residing in the condenser and evaporator, respectively. The system integration involves solving a system of two equations with two unknowns, i.e., the evaporating and condensing pressures (P_e and P_c). The two equations that need to be satisfied are 1) the total

refrigerant charge remains constant at a predetermined level and 2) the suction superheat is equal to the set point. The two intermediate variables, P_e and P_c, are solved iteratively using a multivariate Newton's method for each steady state operation point. In the integrated system model, there is only one estimation parameter, i.e., the total refrigerant charge.

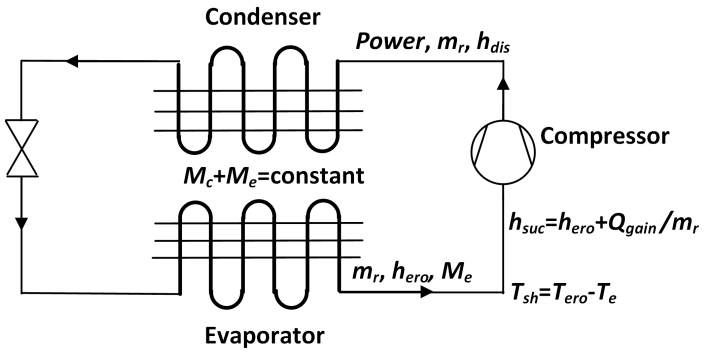

Figure 4.5: Coupling of boundary variables across components with pre-determined charge level and superheat.

The overall modeling methodology entails a two-level training procedure: the lower level identifies the component models separately while the upper level only involves the identification of the total refrigerant charge. Since none of the component models has any dependence on refrigerant inventory, the two training hierarchies are decoupled and can be executed sequentially.

4.3 Case Study Results

4.3.1 Results of Evaporator

A total of 56 steady state tests were conducted for the test unit, covering a range of operating conditions as shown in Table 4.1. The compressor speed and supply fan speed can be directly controlled through the proprietary communication protocol acquired from the manufacturer. The EXV opening is varied through a step motor control sequence implemented in

Arduino UNO3. All the experimental data were collected with a National Instruments CompactRIO controller with relevant input/output modules. The graphical user interface was designed and implemented in LabVIEW running on a PC, which integrates all the control communications with the unit onboard controllers and Arduino. For each steady-state test point, measurements were averaged over a 10-minute time window after the system reached steady state to obtain the steady-state performance.

Table 4.1: Ranges of operating conditions involved in the steady-state tests

Boundary conditions	**Range**
Indoor air flow rate (CFM)	750-1800
Compressor speed (RPM)	1300-3400
Evaporator air inlet temperature (K)	295-300
Evaporator air inlet relative humidity (%)	25-40
Outdoor air temperature (K)	288-306

To evaluate the validity of the proposed correlation, offline simulations were carried out using the high-fidelity correlations given in Equation 4.17 to Equation 4.22 for a range of operating conditions as shown in Table 4.2. The simulations generated a set of 14490 data points which were used in validating the simplified gray-box correlation given in Equation 4.23. Since the data covers almost all possible operating conditions for the evaporator, the training performance represents the best accuracy that can be obtained and therefore, the results reveal the structural identifiability of the proposed model form. Table 4.3 presents the estimation confidence intervals for all parameters, which shows very good parameter accuracy and individual parameter identifiability.

Table 4.2: Range of operating conditions in validation of the simplified model form for the evaporator

Operating conditions	**Range**
Evaporating temperature (K)	268—290
Mass flow rate (g s^{-1})	15—50
Temperature difference (K)	0.1—10

Table 4.3: Offline identification results for the evaporation model

Parameter	**95% confidence interval**	**Estimated value**
θ_1	[1.2162e^{-10}, 1.417e^{-10}]	1.3166e^{-10}
θ_2	[5.2945, 5.3215]	5.308
θ_3	[1.0207, 1.0231]	1.0219
θ_4	[2.6518e^{-6}, 2.9756e^{-6}]	2.813e^{-6}
θ_5	[1.1615, 1.1709]	1.1662
θ_6	[1.0881, 1.0905]	1.0893
θ_7	[-0.7085, -0.7077]	-0.7081

Figure 4.6 depicts the fitting results and compares the two-phase HTC predicted by the high-fidelity Chen's correlation and the proposed correlation model. The results show that the proposed correlation can well capture the variation of the evaporation HTC for all possible operating conditions. It may be noted that this offline identification mainly serves to evaluate the validity of the proposed gray-box model form. In modeling of actual systems, it would be cost prohibitive to acquire such informative training data, and model identifiability is highly dependent on the quality of training data available, which is called data-dependent identifiability (in contrast to structural identifiability). For real-world applications with limited training data sets, the sensitivity analysis and de-correlating methods illustrated in Section 4.1 are critical steps to avoid over-parametrization issues and to guarantee reasonable parameter identifiability.

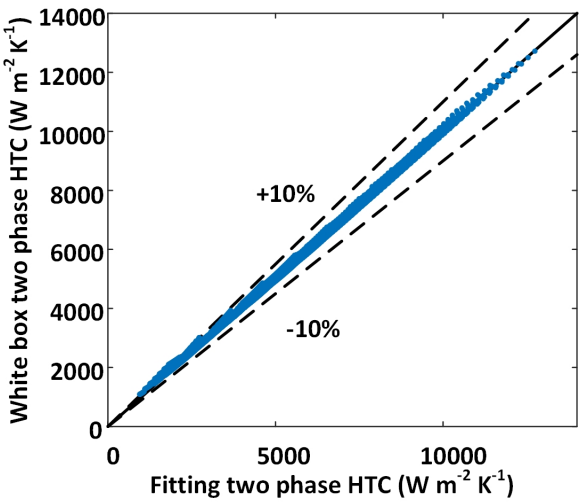

Figure 4.6: Comparison of evaporation HTC predicted by Chen correlation and the gray-box model (RMSRE=1.78%).

In this dissertation, the root mean square relative error (RMSRE) is used to evaluate the prediction accuracy of the gray-box model against the benchmark data:

$$\text{RMSRE} = \sqrt{\frac{1}{N}\sum_{i=1}^{N}\left(\frac{y_{mea}^{i} - y_{est}^{i}}{y_{mea}^{i}}\right)^{2}} \times 100\% \tag{4.35}$$

where N is the number of data points, y_{mea}^{i} and y_{est}^{i} are the ground-truth and predicted values of the variable of concern for the i^{th} data point.

In addition to the parameters involved in Equation 4.16 and Equation 4.23, other parameters that need to be estimated include the tube length l and number of circuits C. For air-conditioning, heat pump and refrigeration systems, 3/8"-diameter tubes are predominantly used. Therefore, the standard tube diameter and wall thickness are used in the gray-box model without any training involved. All candidate parameters to be estimated are summarized in Table 4.4. It may be noted that all the estimation parameters take continuous values except for the number of circuits C. Since most nonlinear regression algorithms are only applicable to problems with continuous parameters, a "mixed-integer" training scheme

is adopted where the discrete parameter is enumerated for a set of possible values and for each integer value of C, identification is performed for the remaining continuous parameters. The parameter value combination that achieves the minimum error is selected. Four discrete values (4, 6, 8 and 10) are considered for the number of circuits during training. Besides, the continuous parameters of refrigerant side HTC that are shown in Table 4.4 have been ranked with their significance based on the PCA-based method with the 56 training data points.

Estimation of the model parameters is a classic nonlinear regression problem and a Levenberg–Marquardt-based algorithm (Yu and Bogdan, 2018[74]) was used. Offline simulations were carried out with the high-fidelity Chen correlation for a wide range of operating conditions, resulting in a total of 14490 performance points. These results were used in a nonlinear regression to obtain the initial guesses of the parameters associated with the evaporation HTC correlation (θ's in Table 4.4). The parameter a_2 assumes an initial value of 0.8, which is equal to the exponent of Reynolds number in classic turbulent flow HTC correlations. The tube length l and parameter a_1 should be proportional to the system capacity and assume initial values of 10 m/ton and 400/ton, respectively.

Table 4.4: Estimation parameters of the evaporator model

Continuous parameter				**Discrete parameters**
Evaporation HTC correlation	Air HTC correlation		Geometry	C
$\{\theta_3, \theta_7, \theta_1, \theta_2, \theta_4, \theta_5, \theta_6\}$	a_1	a_2	l	

The 56 experimental data points were divided into two groups, a training data set and a validation data set. It is generally true that the accuracy of an identified model is positively correlated with the size of training data. To understand the sensitivity of model accuracy with the training data size, a parametric analysis has been conducted for different combinations of training data size and number of estimation parameters. The comparisons of the validation RMSRE (VRMSRE) for the various cases are shown in Figure 4.7. The three

plots correspond to training data sizes of 26, 36 and 46, respectively. For each size, training data points were chosen randomly from the candidate data set of 56 points. To reduce the bias and uncertainty, the random selection of the training data points was repeated 10 times and the box plots in Figure 4.7 present the statistics of the prediction accuracy under different sizes of training data and parameter set. When limited training data is available, such as for plots (a) and (b) with sizes of 26 and 36, the model accuracy deteriorates when more estimation parameters are involved. This is expected since it is more challenging for smaller data sets to cover a wide range of operating conditions and using more parameters would lead to higher risks of over-parameterization and inter-parameter correlations. On the other hand, larger training data sets can have a better coverage of operating scenarios and estimating more parameters simultaneously would be less problematic, which is evident from plot (c). Another observation from the comparison of plots (a) and (b) is that larger training data sets lead to better model accuracy for a given set of estimation parameters.

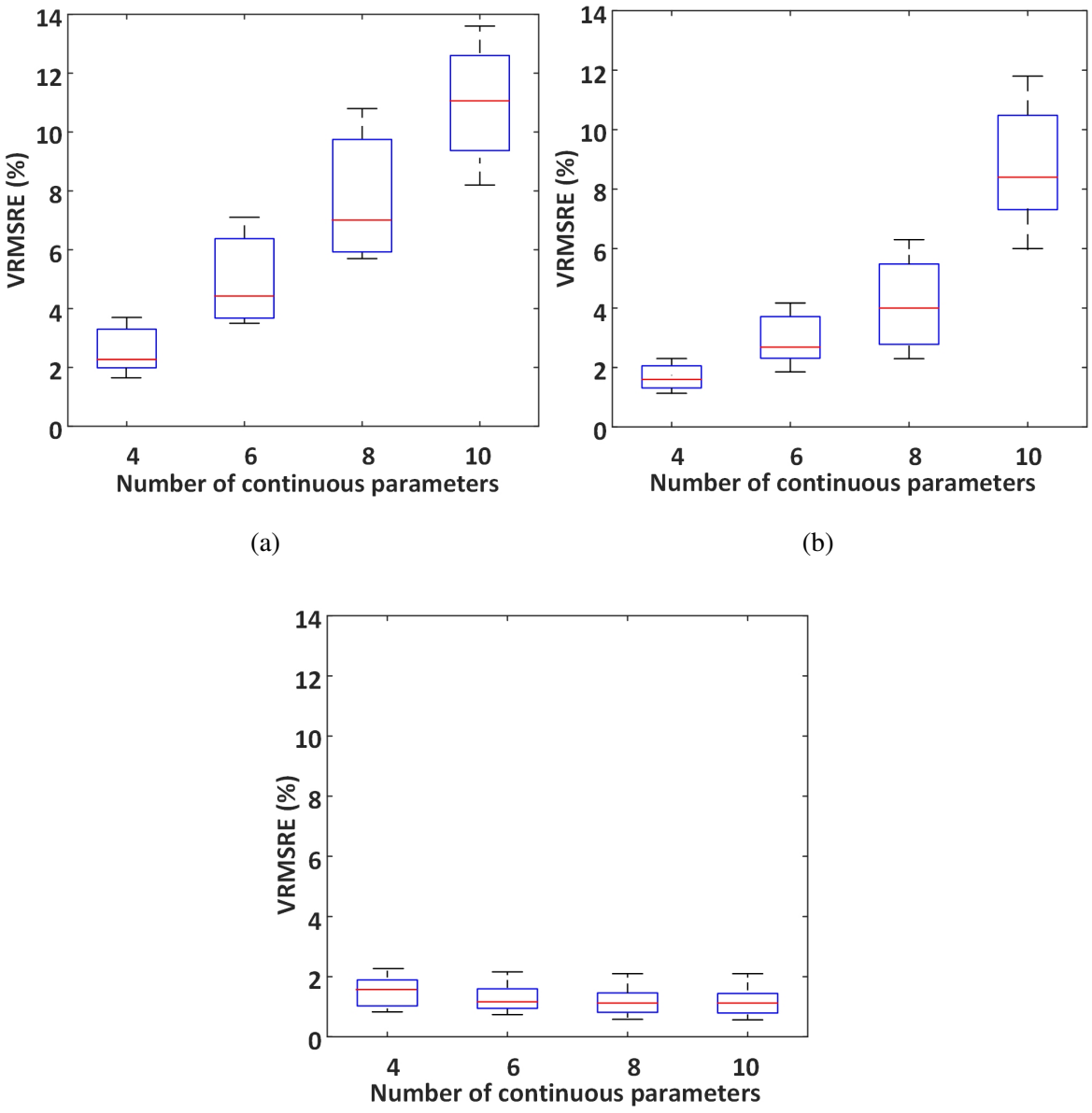

(a) (b)

(c)

Figure 4.7: Comparisons of VRMSRE for training data sizes of (a) 26, (b) 36 and (c) 46.

Figure 4.8 compares the sizes of the averaged confidence intervals for different training data sizes. For each parameter, a normalized size of confidence interval can be calculated relative to the estimated parameter value. An averaged confidence interval size across all estimation parameters serves as an indicator of the parameter accuracy. Results in Figure 4.7

and Figure 4.8 together show that when a small training data set is available, both the parameter accuracy and prediction accuracy, indicated by VRMSRE, deteriorate with the increasing number of estimation parameters. However, for cases with relatively larger training data sets, e.g., of size 46, the prediction accuracy improves with the number of parameters while the parameter accuracy has the opposite trend. To seek an optimal trade-off between the reliability of the parameter estimate (dictated by the size of confidence interval or estimation variance) and training accuracy, six estimation parameters are used in the final gray-box model.

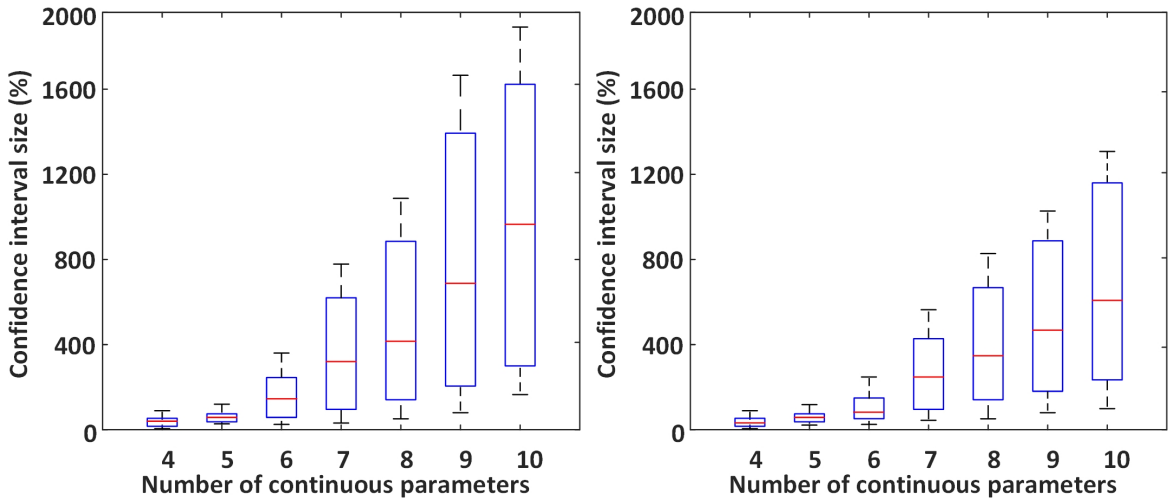

(a) (b)

Figure 4.8: Confidence interval sizes for (a) 26 training data points and (b) 46 training data points.

The estimated values for the six parameters with a randomly chosen 46-point training data set for different circuit numbers are shown in Table 4.5, where the results highlighted in bold indicate the final identification results with the minimum training RMSRE (TRMSRE). It can be seen that the air-side HTC parameters have the highest accuracy with the smallest confidence intervals (approximately 25%) while high uncertainties exit for the refrigerant-side HTC parameters with large confidence intervals (40% to 110%). This is expected since air-side heat transfer resistance dominates the overall thermal resistance for air-to-refrigerant

evaporators and therefore, the model output is more sensitive to air-side parameters. In this dissertation, the evaporator coil was taken out of the indoor unit and carefully inspected. The total tube length for the evaporator is approximately 42.32 m with 8 parallel circuits. It is evident that the identification technique is able to reasonably capture the geometric properties of the system.

Table 4.5: Parameter estimation results for randomly chosen 46 training data points

Circuit number	θ_1	θ_3	θ_7	a_1	a_2	$l\,(m)$	**TRMSRE**
4	$2.3074e^{-10}$	-0.7415	-0.8281	1238.8	1.278	34.148	2.11%
6	$2.1298e^{-10}$	-0.6916	-0.7653	1346.1	1.1615	35.9766	1.85%
8	$\mathbf{1.9517e^{-10}}$	$\mathbf{-0.64}$	$\mathbf{-0.7122}$	**1297**	**1.2671**	**36.72**	**1.35%**
[95% confidence	$[1.3095e^{-10}$,	$[-1.3897$,	$[-1.0438$,	[916.3,	[1.0396,	[12.124,	
interval]	$2.5938e^{-10}]$	$0.1096]$	$-0.3806]$	1677.7]	1.4946]	61.32]	
10	$1.7263e^{-10}$	-0.5622	-0.7824	1112.6	1.1579	41.388	2.39%

Figure 4.9 compares the predicted cooling capacity by the six-parameter evaporator models identified with 26 and 46 training data points, which shows a consistent trend to that shown in Figure 4.7, i.e., larger training data set results in a better prediction accuracy.

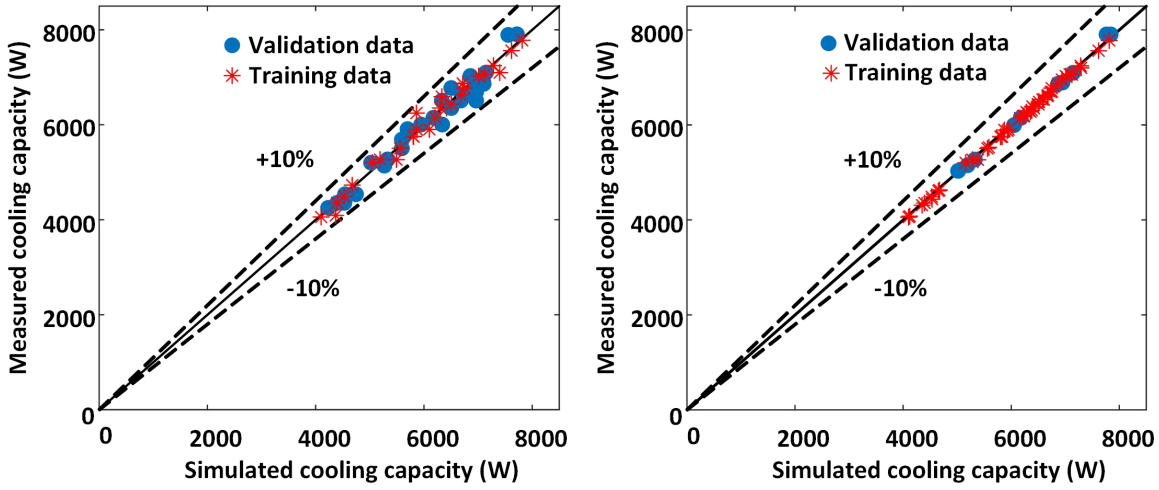

(a) (b)

Figure 4.9: Comparisons of cooling capacity between simulation and experiment for (a) 26 training data points, VRMSRE=5.08% and (b) 46 training data points, VRMSRE=1.54%.

4.3.2 *Results of Condenser*

The establishment of the condenser model followed a similar procedure. The PCA-based method was utilized to identify the influential parameters and to rank the parameter significance. The candidate estimation parameters of the condenser model are the refrigerant-side HTC parameters c_1 to c_5 shown in Equation 4.29, air side HTC b_1, tube length l and number of circuits C. The comparisons of confidence intervals and RMSRE for the various cases are shown in Figure 4.10 and Figure 4.11, respectively. The results show similar trends to those of the evaporator: with limited training data, higher parameter and prediction accuracies can be achieved with fewer estimation parameters; when adequate performance data is available, more estimation parameters can result in higher prediction accuracy but lower parameter accuracy.

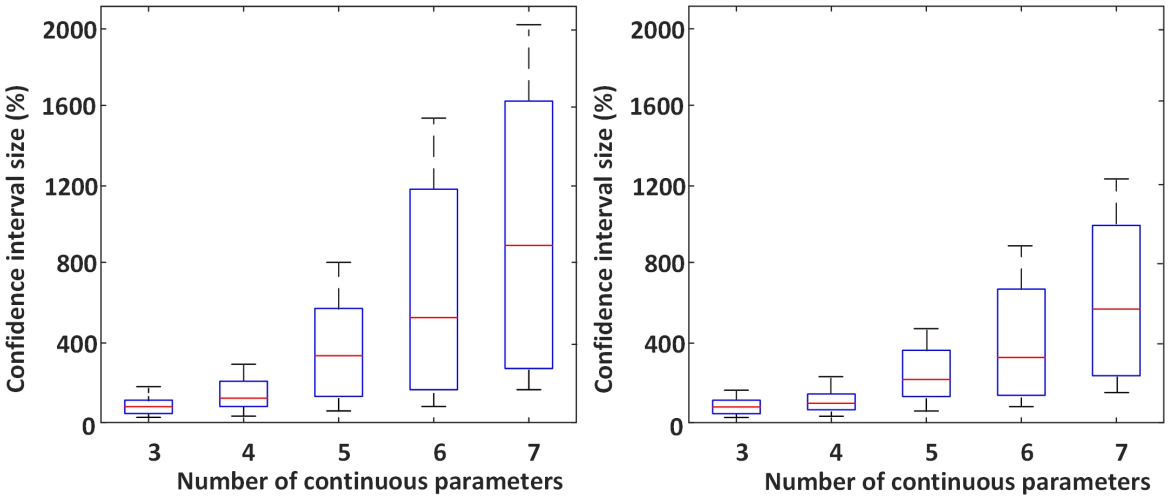

(a) (b)

Figure 4.10: Confidence interval sizes for (a) 26 training data points, (b) 46 training data points.

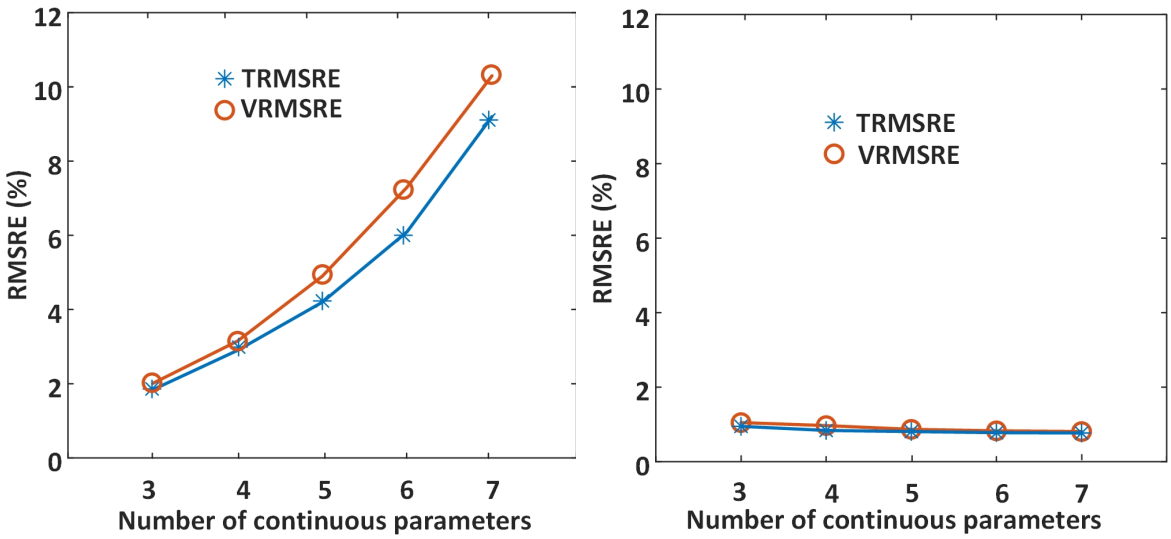

(a) (b)

Figure 4.11: TRMSRE and VRMSRE for (a) 26 training data points, (b) 46 training data points.

Similar to the evaporator case, the number of circuits is an estimation parameter of integer type and needs to be estimated separately. Based on the results presented in Figure 4.10 and Figure 4.11, five continuous parameters were used for training in the gray-box model. The estimated parameter values for the different number of circuits with a 46-piont training data set are shown in Table 4.6, where the results highlighted in bold indicate the final identification results achieving the minimum TRMSRE. It was challenging to disassemble the outdoor unit for a thorough inspection of the condenser coil. However, the CAD drawing of the condenser coil was acquired from the manufacturer from which the total tube length of the condenser was estimated (approximately 224.88 m with 8 parallel circuits). The model identification results are in good agreement with the actual condenser geometries.

Table 4.6: Identified parameter values for the condenser

Circuit number	b_1	c_1	c_2	c_3	$l\,(m)$	**TRMSRE**
4	25.2789	0.0438	4.4579	$1.1315e^8$	264.27	1.21%
6	25.0871	0.0547	3.4825	$0.9553e^8$	260.93	1.07%
8 [95% confidence interval]	**24.514** [22.878, 26.15]	**0.0506** [0.0336, 0.0675]	**2.5371** [−1.1686, 6.2428]	**$1.0776e^8$** [$8.172e^7$, $1.338e^8$]	**274.38** [159.26, 389.5]	**0.86%**
10	24.7987	0.062	2.013	$0.847e^8$	281.48	0.95%

The comparisons of the measured and predicted condenser heat for 26 and 46 training data points are shown in Figure 4.12. The results show satisfactory prediction accuracy for both training data sizes, although a much higher accuracy is achieved for the larger training data set.

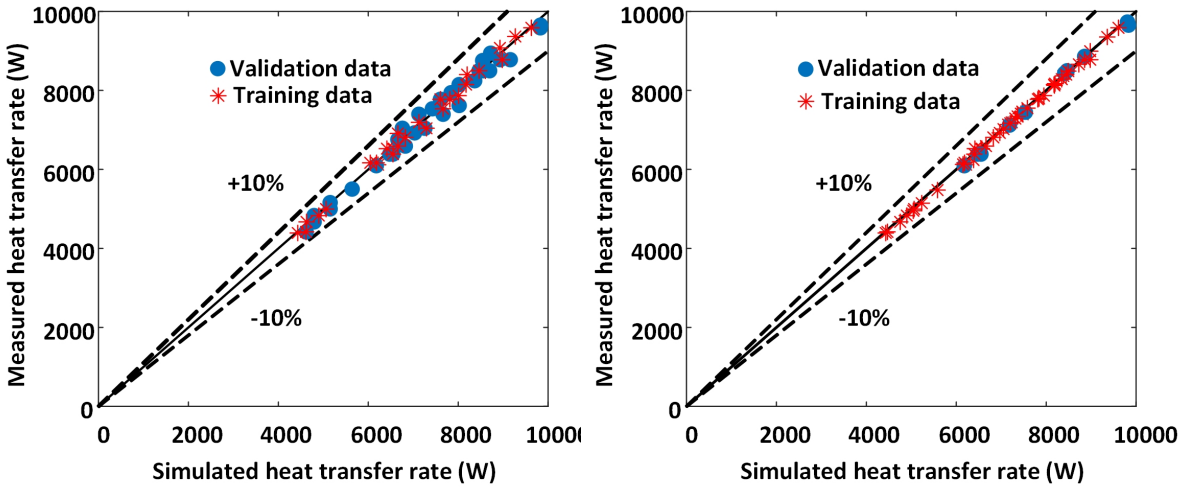

(a) (b)

Figure 4.12: Comparisons of condenser heat transfer rate between simulation and experiment for (a) 26 training data points, VRMSRE=4.09% and (b) 46 training data points, VRMSRE=0.93%.

4.3.3 Results of Compressor Model

Since the compressor model involves very few parameters and identification of the sub-models (i.e., for predictions of mass flow rate, discharge enthalpy and power) can be carried out in a decoupled manner, down-selection of estimation parameters is not necessary. For the subcomponent model for mass flow prediction, there is only one estimation parameter, i.e., the compressor swept volume. Direct measurement of the discharge enthalpy is available and thus, the combined isentropic efficiency can be calculated from the experimental data. This allows easy identification of the coefficients of the isentropic efficiency correlation given in Equation 4.32 through least-square linear regression. This isentropic efficiency sub-model can be used to calculate the discharge enthalpy. Similarly, the correlation for the heat loss ratio in Equation 4.33 can be trained directly from measurements, which allows the prediction of the compressor power input together with the mass flow and isentropic efficiency sub-models. Identification of each sub-component model was performed for training data sets of 26 points and 46 points. The model training and validation errors are depicted in Figure 4.13 to Figure 4.15 for predictions of mass flow rate, discharge enthalpy and power input, respectively. Note that enthalpy is a differential variable and to obtain a meaningful accuracy assessment for discharge enthalpy prediction, the errors were evaluated with a reference enthalpy of $2.6e^5 \text{J kg}^{-1}$, which is close to the enthalpy of condenser outlet. It can be observed that the compressor power prediction errors are greater than those of the heat exchangers; this is because the power prediction relies on the sub-models for mass flow, combined isentropic efficiency and heat loss and the corresponding sub-model inaccuracies added up to higher total errors in compressor power prediction. Training and validation results for the combined efficiency and heat loss ratio are shown in Figure 4.16 and Figure 4.17, respectively.

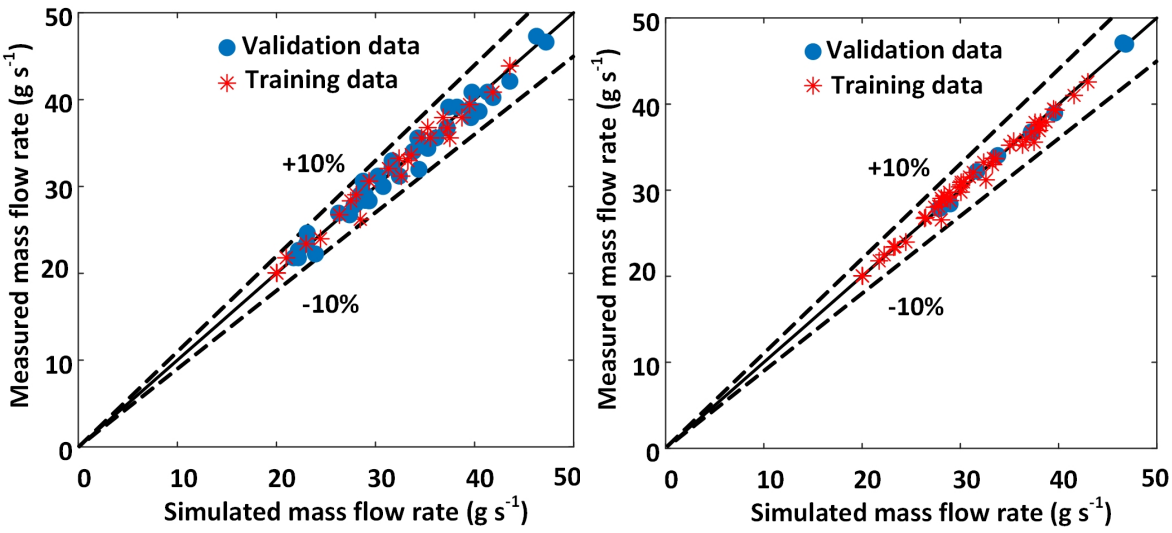

(a) (b)

Figure 4.13: Comparisons of mass flow rate between simulation and experiment for (a) 26 training data points, VRMSRE=5.88% and (b) 46 training data points, VRMSRE=1.21%.

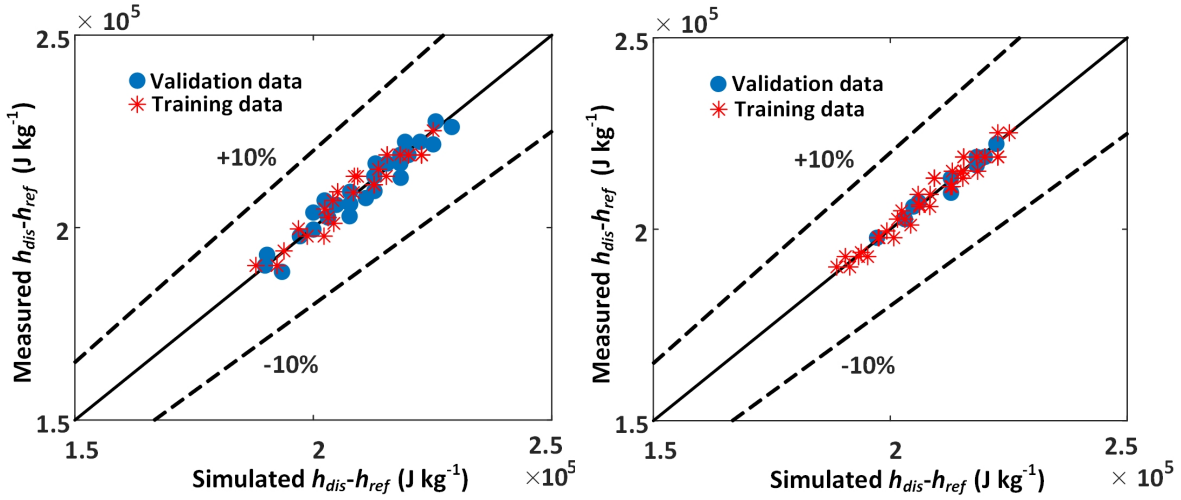

(a) (b)

Figure 4.14: Comparisons of discharge enthalpy between simulation and experiment for (a) 26 training data points, VRMSRE=0.47% and (b) 46 training data points, VRMSRE=0.24%.

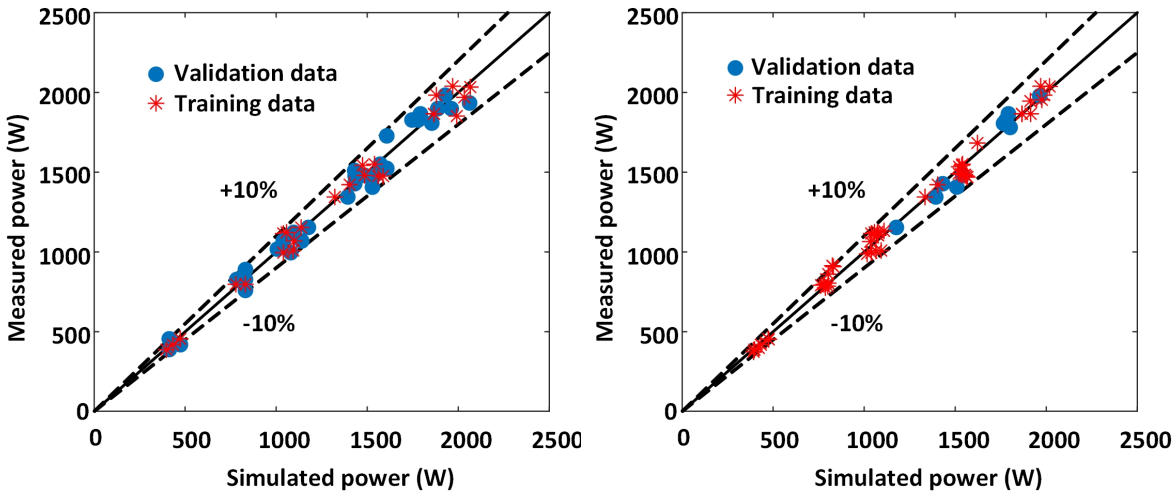

(a) (b)

Figure 4.15: Comparisons of power between simulation and experiment for (a) 26 training data points, VRMSRE=6.87%, abd (b) 46 training data points, VRMSRE=3.49%.

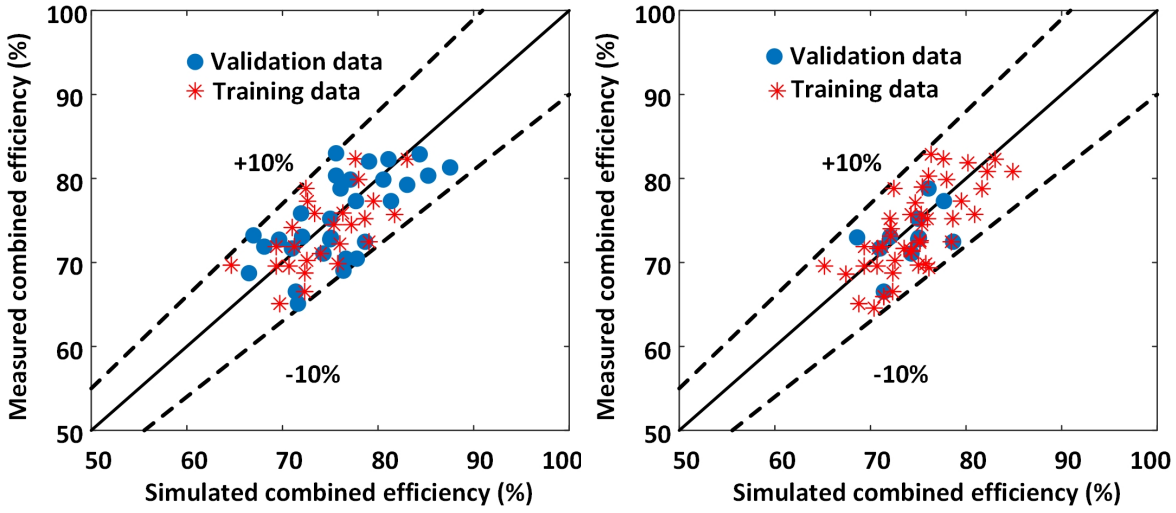

(a) (b)

Figure 4.16: Comparisons of combined efficiency between simulation and experiment for (a) 26 training data points, VRMSRE=6.94%, and (b) 46 training data points, VRMSRE=4.67%.

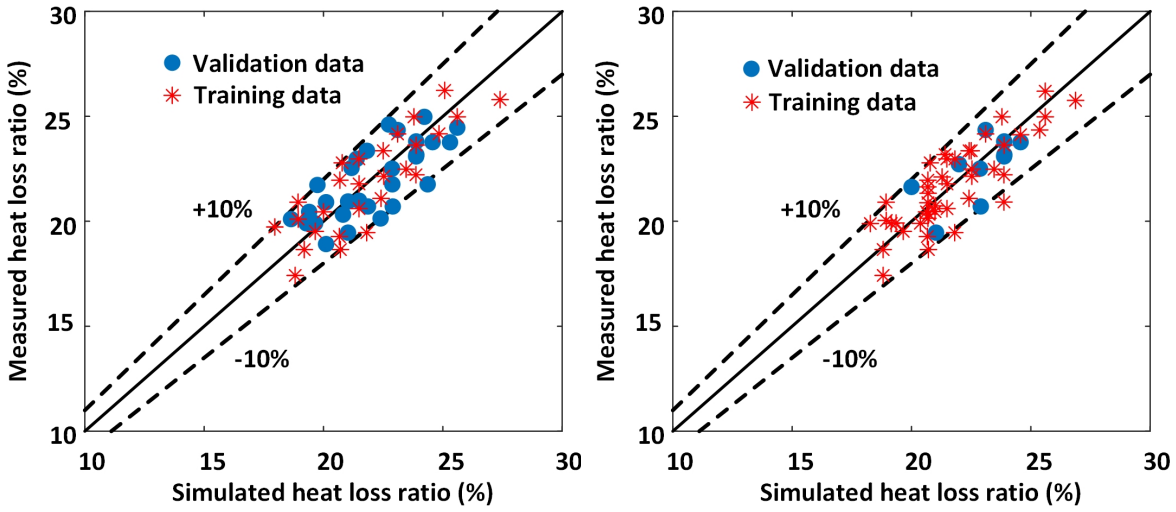

Figure 4.17: Comparisons of heat loss ratio between simulation and experiment for (a) 26 training data points, VRMSRE=7.12%, and (b) 46 training data points, VRMSRE=5.65%.

4.3.4 Results of Integrated Model

In the integrated model, the only estimation parameter is the system refrigerant charge. In training of the system model, the established component models were integrated and a simple line search was performed to find the charge achieving the minimum RMSRE in the cooling capacity prediction. The estimated charge was 3.014 kg with a 95% confidence interval of 2.8145 kg to 3.2145 kg, using a 46-point training data set. The TRMSREs for cooling capacity prediction under various refrigerant charge levels are shown in Table 4.7. The comparisons of the predicted (by the integrated model) and measured cooling capacity, compressor power and saturated condensing/evaporating temperatures are shown in Figure 4.18 to Figure 4.20. The identified system model with 46 training points is able to predict the cooling capacity and compressor power with errors of approximately 3.5%. When the size of training data is limited to 26, the prediction errors almost double but are still satisfactory.

Table 4.7: System model training accuracy under different charge levels

Charge (kg)	2.8	2.9	3	3.1	3.2
TRMSRE	3.46%	3.39%	3.28%	3.32%	3.38%

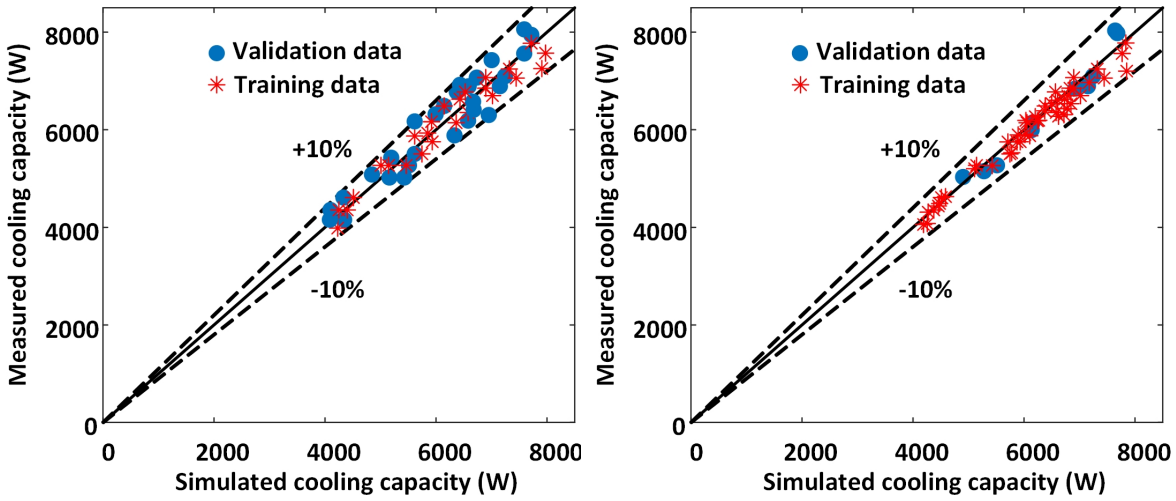

(a) (b)

Figure 4.18: Comparisons of cooling capacity between simulation and experiment for (a) 26 training data points, VRMSRE=6.55%, and b) 46 training data points, VRMSRE=3.29%.

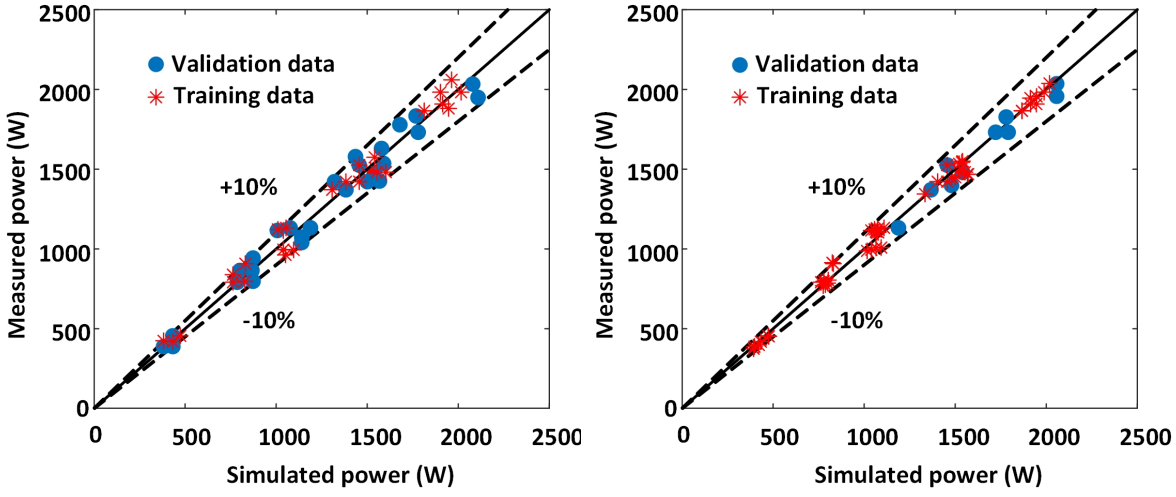

(a) (b)

Figure 4.19: Comparisons of compressor power between simulation and experiment for (a) 26 training data points, VRMSRE=7.2%, and (b) 46 training data points, VRMSRE=3.86%.

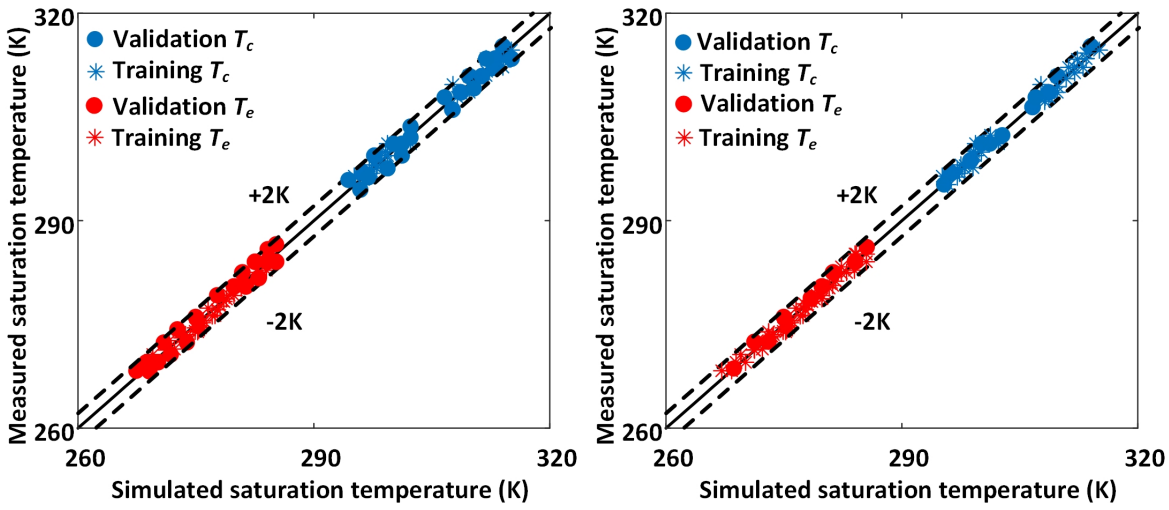

(a) (b)

Figure 4.20: Comparisons of saturation temperatures between simulation and experiment for (a) 26 training data points, VRMSE=1.39 K, and (b) 46 training data points, VRMSE=0.62 K.

4.4 Chapter Summary

This chapter presented a gray-box steady-state modeling methodology for variable-speed DX systems that preserves model reliability under limited training data. A hierarchical training scheme is adopted where the component models are trained separately and are then integrated through continuity equations to establish a system model that is fine-tuned by adjusting the system refrigerant charge. This sequential training approach reduces computational burden and improves model reliability during training. To mitigate potential over-parameterization issues, the methodology incorporates a parameter down-selection procedure to eliminate non-influential and correlated parameters. The methodology was applied to a 3-ton variable-speed heat pump to characterize its steady-state performance. Prediction and parameter accuracies were demonstrated for different training data sizes. It was shown that parameter accuracy deteriorates as more parameters are to be estimated. However, the trend of prediction accuracy bifurcates as the size of training data varies: when adequate

training data is available, the model prediction accuracy improves as more estimation parameters are used; but for cases with limited training data, the prediction accuracy becomes worse when more parameters are estimated. By virtue of its simplicity, the developed steady-state model can also be applied for general online applications such as control optimization and FDD.

Chapter 5: Dynamic Modeling of VCS

This chapter describes a gray-box dynamic modeling methodology for VCSs, built on top of the steady-state modeling approach presented in the preceding chapter. The goal is to establish a dynamic simulation testbed, calibrated with experimental data of the test heat pump that is described in Chapter 3.

The overall modeling methodology consists of a hierarchical training procedure as shown in Figure 5.1. The bottom layer involves identification of steady-state component models associated with the heat exchangers (evaporator and condenser), compressor and EXV. In the middle layer, the established component models are integrated through continuity equations to obtain a system model. The bottom and middle layer model identification follows the approach presented in Chapter 4. The top layer transforms the steady-state system model into a dynamic one described by state-space governing equations, in which the optimal thermal capacitances of the heat exchanger walls are identified to best reproduce system transient responses. This hierarchical training methodology minimizes the number (only two) of estimation parameters and the associated numerical iterations of the computationally demanding dynamic model, while the parameters pertinent to steady-state performances (more than ten) are estimated using the fast steady-state models. This hierarchical training approach ensures numerical feasibility for training of the dynamic VCS model. Further, decoupled estimation of parameter groups associated with the different components reduces the risks of over-parameterization and inter-parameter correlations, which is critical for reliable model identification.

The major assumption in the dynamic modeling method, in addition to those made for the steady-state counterpart presented in Chapter 4 is that the dynamics for the compressor,

EXV and air-side energy balances of heat exchangers are neglected.

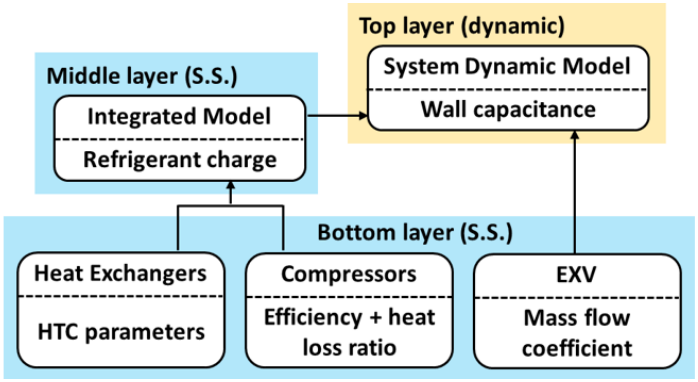

Figure 5.1: Overall schematic diagram of the gray-box dynamic modeling methodology.

5.1 Steady State Model Identification

Identification of the steady-state component and system models, involved in the bottom and middle layers of the hierarchical training procedure, is based on the robust training methodology that is presented in Chapter 4. This methodology assumes simplified correlations for the different component models and incorporates two pre-training conditioning steps to improve the model identifiability: (1) a parameter reduction step that identifies and eliminates the non-influential estimation parameters and (2) a parameter de-correlation step where potential correlations among the remaining parameters are identified and reduced, resulting in further estimation parameter reduction. The modeling details can be found in Chapter 4. The component models capture the component physics through heat and mass balances together with empirical correlations whose parameters are estimated based on performance data. The identified component models are then integrated into a steady-state system model with the refrigerant charge level being the sole estimation parameter.

5.2 Dynamic Model Identification

5.2.1 EXV Model

EXVs are increasingly used in modern VCS because of their fast and accurate response to control actuation and adaptability to time-varying operating conditions. An EXV model is not required in the steady-state model as the measured superheat is used as an input variable. However, a dynamic VCS model ought to characterize the dynamics of superheat (an output variable) and should incorporate an EXV model. This dissertation assumes the following orifice equation to calculate the refrigerant flow through the EXV (Li, 2013[75])

$$m_r = C_d A Y \sqrt{2\rho_f \left(P_c - P_e\right)} \tag{5.1}$$

where A is the throat area of the EXV when it's fully open and ρ_f is the saturated liquid refrigerant density at the condensing pressure. Y is the expansion factor capturing volume expansion of the refrigerant when two-phase refrigerant enters the EXV; the expansion factor is dependent on the refrigerant pressure ratio and thermal properties, e.g., specific heat (Davies and TC, 1973[76]). When sub-cooled refrigerant enters the EXV (i.e., subcooling is nonzero), the expansion factor is unity. The mass flow coefficient C_d is a dimensionless variable that changes with the valve opening δ and subcooling T_{sb}. The following polynomial is found appropriate to capture the EXV behavior from the experimental data:

$$C_d = f_1 + f_2\delta + f_3\delta^2 + f_4\delta\left(\frac{T_{sb}}{T_c}\right) \tag{5.2}$$

where T_c is the critical temperature of the refrigerant, and f_1 to f_4 are estimation parameters.

5.2.2 *Dynamic Heat Exchanger Model*

The evaporator dynamic model extends the steady-state one by incorporating explicit conservation differential equations for the refrigerant energy, mass and tube wall energy of each control volume, given in Equation 5.3 to Equation 5.5.

$$\dot{U}_j = m_{j-1}h_{j-1} - m_j h_j + \alpha_{r,j}A_{i,j}\left(T_{w,j} - T_{r,j}\right) \tag{5.3}$$

$$\dot{m}_{e,j} = m_{j-1} - m_j \tag{5.4}$$

$$\dot{E}_j = \left(C_{th,w}\right)_j \dot{T}_{w,j} = \alpha_{a,j}A_{o,j}\left(T_{a,j} - T_{w,j}\right) - \alpha_{r,j}A_{i,j}\left(T_{w,j} - T_{r,j}\right) \tag{5.5}$$

where U_j is the refrigerant internal energy; m_{j-1} and m_j represent the inlet and outlet mass flow rates of refrigerant, respectively; $\dot{m}_{e,j}$ is the time derivative of the refrigerant mass held in the j^{th} control volume; E_j is the tube wall energy and $C_{th,w}$ denotes the thermal capacitance of the heat exchanger tube wall, which is estimated in the training process. The HTCs and areas assume the values identified in the bottom and middle layers so the evaporator dynamic model only involves a single estimation parameter.

Based on the relationship between the refrigerant specific internal energy u and enthalpy ($u = h - \frac{P}{\rho}$), the time derivative of the refrigerant internal energy in Equation 5.3 can be decomposed into terms of time derivatives with respect to the pressure and enthalpy using the chain rule:

$$\dot{U}_j = V_j\left[\left(\left.\frac{\partial \rho_j}{\partial P_e}\right|_{h_j}\right)\dot{P}_e + \left(\left.\frac{\partial \rho_j}{\partial h_j}\right|_{P_e}\right)\dot{h}_j\right]h_j - V_j\dot{P}_e + V_j\rho_j\dot{h}_j \tag{5.6}$$

where V_j represents the tube internal volume for the j^{th} control volume and the evaporating pressure P_e is assumed to be identical across all control volumes (no pressure drops).

Similarly, the mass balance Equation 5.4 can be re-written as

$$\dot{m}_{e,j} = V_j \dot{\rho}_j = V_j \left[\left(\left. \frac{\partial \rho_j}{\partial P_e} \right|_{h_j} \right) \dot{P}_e + \left(\left. \frac{\partial \rho_j}{\partial h_j} \right|_{P_e} \right) \dot{h}_j \right] \tag{5.7}$$

Equation 5.6 and Equation 5.7 allow the following reformulation of the governing equations using the evaporation pressure and enthalpy as state variables:

$$\mathbf{Z} \begin{bmatrix} \dot{P}_e \\ \dot{h}_1 \\ \vdots \\ \dot{h}_N \\ \dot{T}_{w,1} \\ \vdots \\ \dot{T}_{w,N} \end{bmatrix} = \begin{bmatrix} m_{in} \left(h_{in} - h_1 \right) + \alpha_{r,1} A_{i,1} \left(T_{w,1} - T_{r,1} \right) \\ \vdots \\ m_{in} \left(h_{N-1} - h_{out} \right) + \alpha_{r,N} A_{i,N} \left(T_{w,N} - T_{r,N} \right) \\ m_{in} - m_{out} \\ \alpha_{a,1} A_{o,1} \left(T_{a,1} - T_{w,1} \right) - \alpha_{r,1} A_{i,1} \left(T_{w,1} - T_{r,1} \right) \\ \vdots \\ \alpha_{a,N} A_{o,N} \left(T_{a,N} - T_{w,N} \right) - \alpha_{r,N} A_{i,N} \left(T_{w,N} - T_{r,N} \right) \end{bmatrix} \tag{5.8}$$

where $\mathbf{Z}$ is the transformation matrix that is dependent on the evaporation pressure and refrigerant enthalpy of each control volume. The detailed structure of the matrix can be found in Gupta (2007)[77]. N denotes the total number of control volumes. m_{in} and m_{out} are the inlet and outlet refrigerant mass flow rates for the evaporator, respectively. Solving the non-linear differential Equation 5.8 requires inversion of the transformation matrix, the size of which depends on the number of dynamic state variables $(2N + 1)$. In the case study, to seek a trade-off between the model accuracy and computational efficiency, the evaporator was divided into 20 control volumes, i.e., $N = 20$. The differential equations were solved numerically using the fourth-order Runge-Kutta solver with a fixed time step of 0.05 s (Greenberg, 1988[78]).

The governing equations for the condenser dynamics assume exactly the same form, although a different tube wall thermal capacitance is identified through training.

5.2.3 *Dynamic System Model*

In addition to the integration of the EXV model, the VCS dynamic system model is an natural extension of the steady-state system model established in the middle layer, by incorporating the governing differential equations for the evaporator and condenser dynamics introduced in Section 5.2.2. Since the dynamics of the compressor and EXV are fast and negligible compared to those of the heat exchangers, their steady-state models carry over directly to the dynamic system model. The dynamic system model is established by connecting the component models in a ping-pong scheme: the output of an upstream component for the previous time step is used as the input to calculate the current state of the downstream component. An initialization step is needed to estimate the initial values of the state variables through trial and error so that the total system refrigerant charge of the dynamic model matches the charge level estimated for the steady-state counterpart in the middle layer.

As part of identification of the dynamic system model, thermal capacitances of the heat exchanger tube walls are estimated so that the predicted superheat matches the experimental data with the minimum RMSRE. To illustrate the impact of heat exchanger thermal capacitances on the overall system dynamics, the comparisons between the predicted superheat with different evaporator thermal capacitance values and the measured superheat for the test unit are shown in Figure 5.2, where $C_{th,r}$ denotes the reference evaporator tube wall thermal capacitance calculated from detailed coil geometries provided by the manufacturer. The estimated thermal capacitance is 30% higher than the reference value, possibly because the model also tends to capture the thermal inertia of the temperature sensor (thermocouple installed in the suction line with a metal sheath). The estimated thermal capacitance leads to transient behaviors in best agreement with the measured dynamics. It can be seen from Figure 5.2 that a small thermal capacitance ($0.5C_{th,r}$) leads to fast responses while a large capacitance ($2C_{th,r}$) results in slow system dynamics.

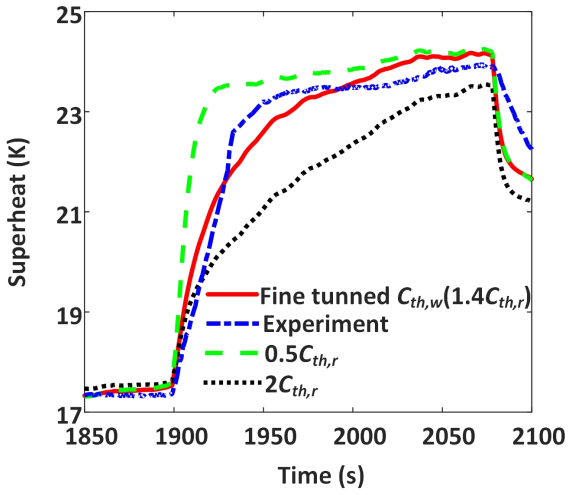

Figure 5.2: Comparisons of superheat dynamics associated with different evaporator thermal capacitance values.

5.3 Case Study Results

5.3.1 Results of EXV

Figure 5.3 shows the EXV model performance, with the same training and validation data sets. The model is able to predict the refrigerant mass flow rate with a VRMSRE of less than 7%. The prediction error is higher than those of the other component models, due to higher uncertainties in the original equipment manufacturer (OEM) EXV characteristics: small offsets in the refrigerant mass flow were observed across multiple repeated tests with exactly the same control and operation settings. Despite the uncertainty, the overall EXV mass flow prediction is still satisfactory.

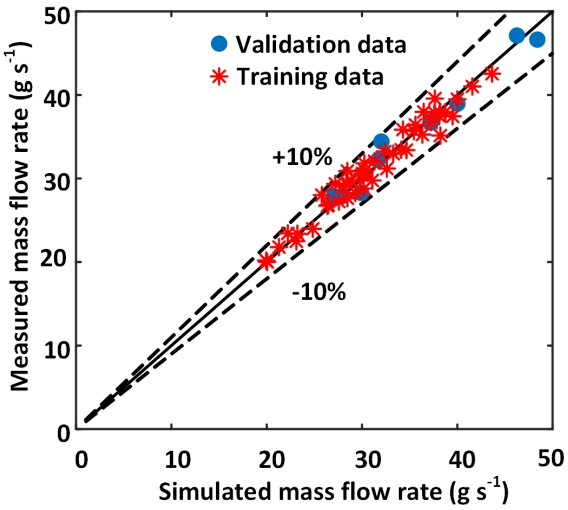

Figure 5.3: Comparison of predicted and measured refrigerant mass flow rate through the EXV (VRMSRE=6.95%).

5.3.2 Results of Dynamic System Model

The final dynamic system model was validated with experimental data collected in a continuous test that consisted of a sequence of different operation settings. The comparisons of the measured and predicted cooling capacity, compressor power consumption, evaporator/condenser saturation temperatures and superheat are depicted in Figure 5.4. The results demonstrate that the identified dynamic model could accurately capture the system dynamics. For this specific validation data set, the model prediction RMSREs are 1.1% for cooling capacity, 3.7% for compressor power consumption, less than 0.8K for the saturated evaporation/condensation temperatures and 0.9K for the superheat.

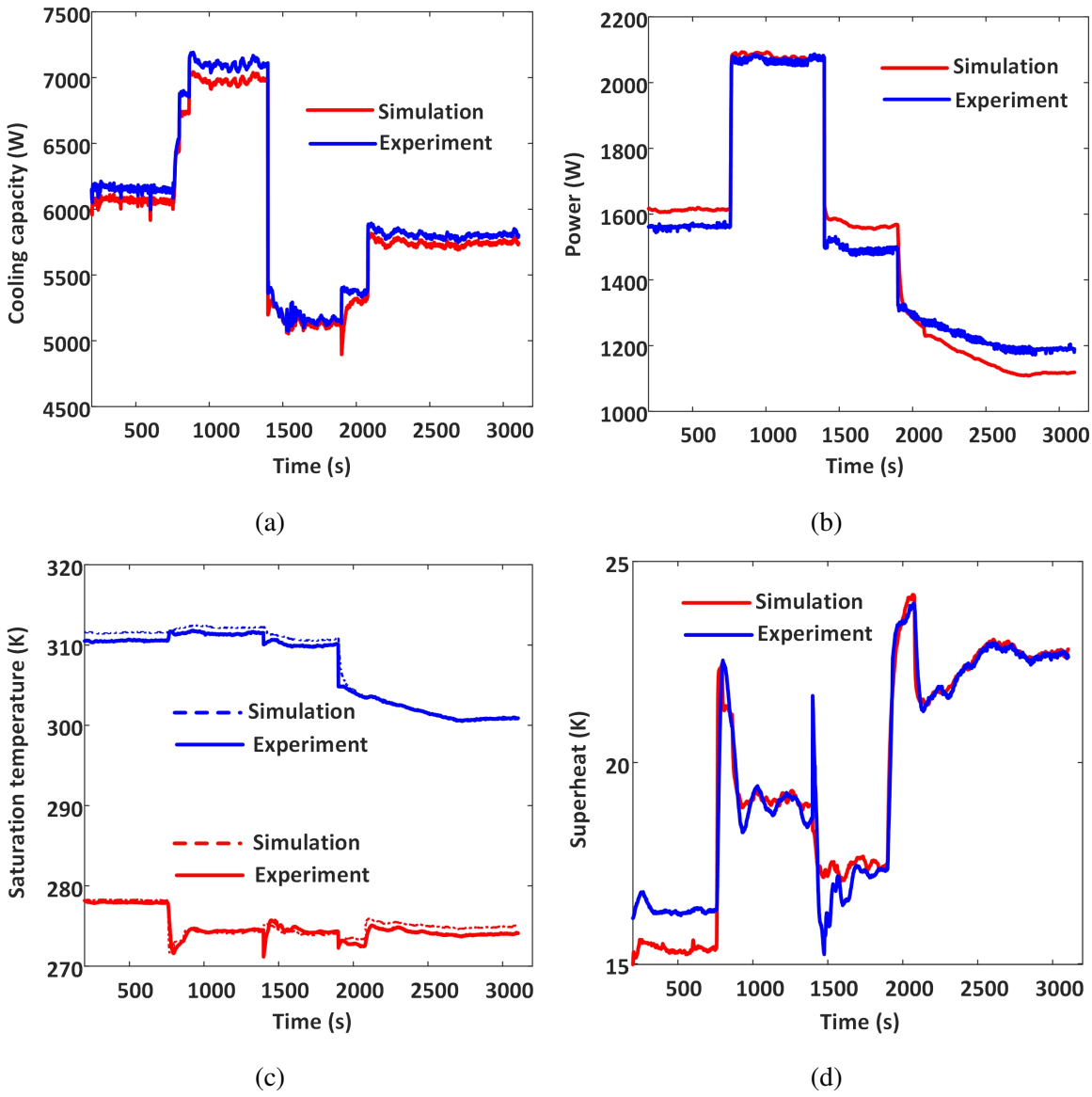

Figure 5.4: Comparisons of system dynamic performance between simulation and experiment for (a) cooling capacity (RMSRE=1.67%), (b) power consumption (RMSRE=3.69%), (c) saturation temperatures (RMSE=0.73K for T_e and RMSE=0.64K for T_c) and (d) superheat (RMSE=0.87K).

5.4 Chapter Summary

For control analysis of existing systems, gray-box VCS models are preferred, which combine physical laws and performance measurements to better capture system character-

istics. Although a good number of studies can be found on steady-state gray-box modeling of VCS (e.g., Cai, 2015[7]; Cheung and Braun, 2013[13]; Lee and Yoo, 2000[10]), attempts on development of dynamic gray-box VCS models have not been reported yet, likely due to the numerical challenge associated with training of the computationally demanding dynamic VCS model. This chapter presented a multi-layer gray-box dynamic modeling methodology for vapor compression systems, which achieves superb model estimation efficiency and reliability by decomposing the model estimation task into multiple sub-problems that can be addressed separately. The main contributions brought by the proposed modeling methodology include (1) improved model identifiability and parameter estimation efficiency through a hierarchical modeling procedure, (2) enhanced prediction accuracy for both the steady-state and dynamic performance. The performance of the methodology was demonstrated using performance data collected from the variable-speed heat pump test unit. The test results verified that the established model can provide accurate predictions of both steady-state and dynamic behaviors under a range of operating conditions, with prediction root mean square relative errors of less than 4%.

Although the proposed modeling methodology has only been tested on heat pump systems, the overall methodology can be directly applied to other types of vapor compression systems, such as multi-compressor and multi-circuit systems, refrigeration units and variable refrigerant flow (VRF) systems. Minor adaptations may be needed for specific applications. For example, modeling of refrigeration systems may require the addition of a receiver component model where the reservoir volume can be treated as an estimation parameter. For dynamic performance characterization of VRF systems, the pressure drops across the connecting lines between the distant indoor and outdoor units need to be captured, possibly through capillary tube models whose flow coefficients can be estimated in the training process. Refrigeration system performance can also be characterized using the proposed methodology while modifications of the evaporator model may be necessary to properly capture the frost formation and defrost dynamics and their impact on the system-

level performance.

Chapter 6: VCS Control Stability Analysis

This chapter presents an application of the developed VCS dynamic model for the digital control stability analysis, with a specific focus on the determination of proper EXV control execution time steps. This particular analysis was motivated by superheat control chattering observed from tests of the heat pump unit with the OEM controller. Improper EXV control execution time step setting was found to be the root cause. Therefore, analysis of such control settings is critical to ensure system operational efficiency and reliability. The chapter starts with an introduction of the hardware and software components of a testing platform for EXV control. A control stability analysis for superheat regulation is followed, which relies on application of linear system theory to linearized dynamics at operating conditions under study.

6.1 EXV Control Testing Platform

TXV and EXV are the most commonly used refrigerant flow regulation devices to maintain desired superheat. In a variable-speed VCS, superheat is typically controlled with fast responding EXV, the opening of which is modulated through a stepper motor. The test unit heat pump comes with a third-party EXV and superheat controller, which only accepts the superheat setpoint from the main unit controller and does not allow direct EXV opening control. To facilitate EXV control testing, a dedicated superheat control testbed was developed and added to the test unit. The original EXV controller was bypassed and the EXV opening was directly controlled with the added control testbed through an external stepper motor driver. Figure 6.1 shows a schematic diagram of a superheat control testbed.

A pressure sensor and a temperature sensor are installed at the outlet of the evaporator for measurements of the evaporating pressure and outlet refrigerant temperature. The temperature/pressure readings are acquired by a high-performance programmable logic controller, which runs the baseline and the proposed control algorithms in generating a control command (0-10 VDC) to the EXV. A stepper motor driver board is used to convert the control command to a pulse sequence for the stepper motor that drives the EXV to open or close.

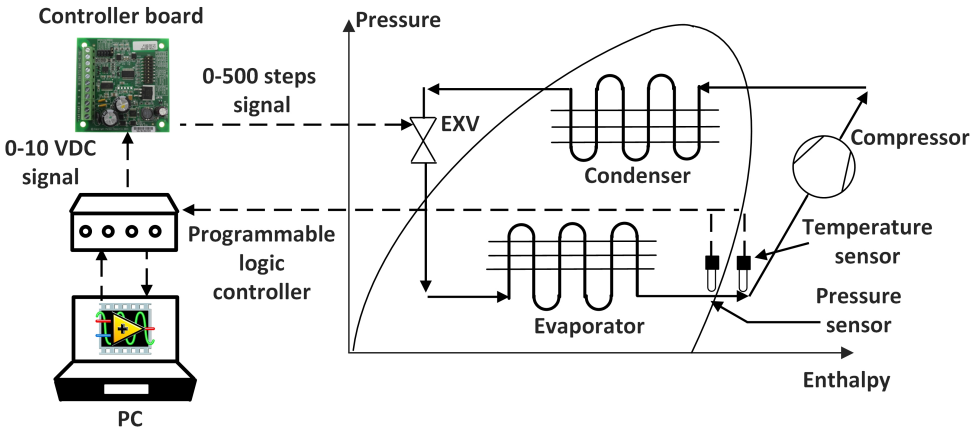

Figure 6.1: Schematic diagram the superheat control testbed.

To facilitate control analysis and synthesis, the gray-box dynamic model developed in Chapter 5 is utilized. All the simulation results presented in subsequent sections were obtained using this model.

6.1.1 Sporlan IB-G Driver Board

The Sporlan IB-G is a small electronic circuit board that extends the functionality of an external system controller to drive step motor valves. The external controller must provide an analog 0-10VDC or 4-20mA signal to the IB-G board. The signal is then converted to a step motor signal to position the valve. The IB-G board has enhanced features including LED indicators for power and valve position and disturbance rejection, which make it an ideal option for our testing platform. The board and its wiring diagram are shown in Fig-

ure 6.2. The experimental tests proved that the Sporlan board is reliable and robust with no error accumulation. Also it does not require additional coding for the conversion of the analog input to pulse sequences (done internally by the board), which simplifies the workflow. The OEM EXV used in the test unit is a CAM electronic linear control valve (shown in Figure 6.3), which consists of two mainly parts: step motor and valve. The motor receive the step signal generated by the controller, to open or close the valve and modulate the refrigerant mass flow rate into evaporator with precise amount.

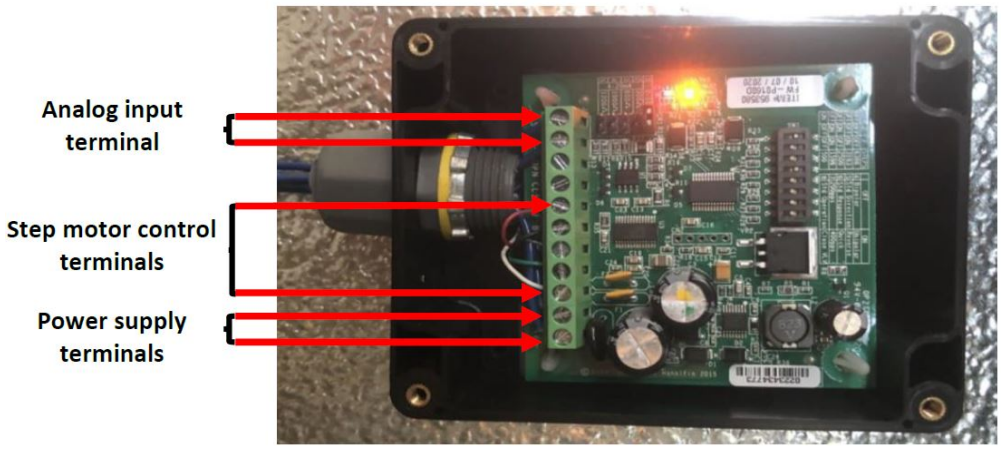

Figure 6.2: Wiring diagram of Sporlan IB-G board and its wiring diagram.

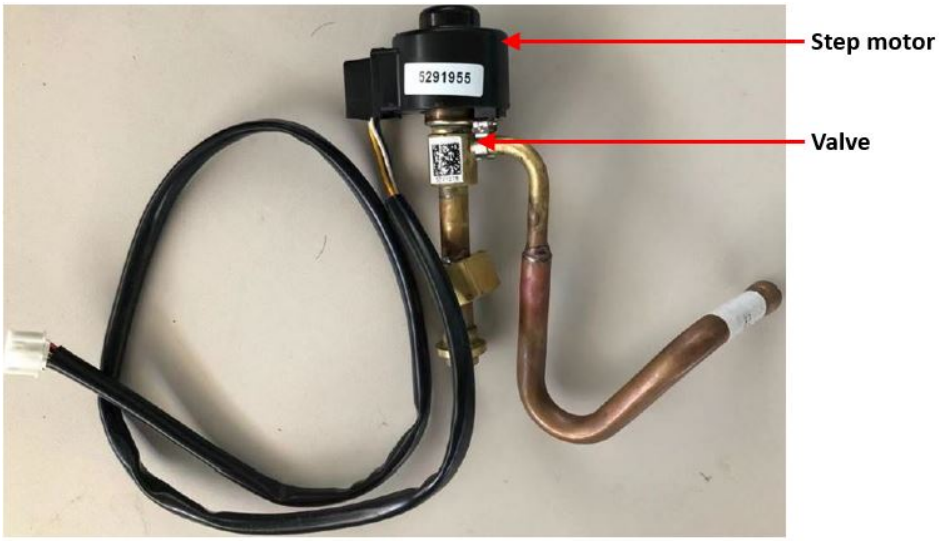

Figure 6.3: CAM EXV (OEM valve used in the test heat pump).

6.1.2 Control and Software Platform

A graphic user interface (GUI) was designed and implemented in LabVIEW running on a PC, which integrates all the control communications with the unit onboard controller and the EXV testing platform (Sporlan IB-G). The LabVIEW GUI front panel shown in Figure 6.4. All control logics were written in LabVIEW. The LabVIEW codes realize two main functions: superheat measurement and control decision making. The refrigerant outlet pressure and temperature measurements are used to calculate the evaporator outlet superheat. Note that the test unit has an additional suite of pressure and temperature sensors at the compressor inlet (suction superheat in Figure 6.4). Both superheat measurements are displayed and trended in the LabVIEW GUI. For the EXV control decision making, a discrete-time PID algorithm was implemented with tunable P/I gains.

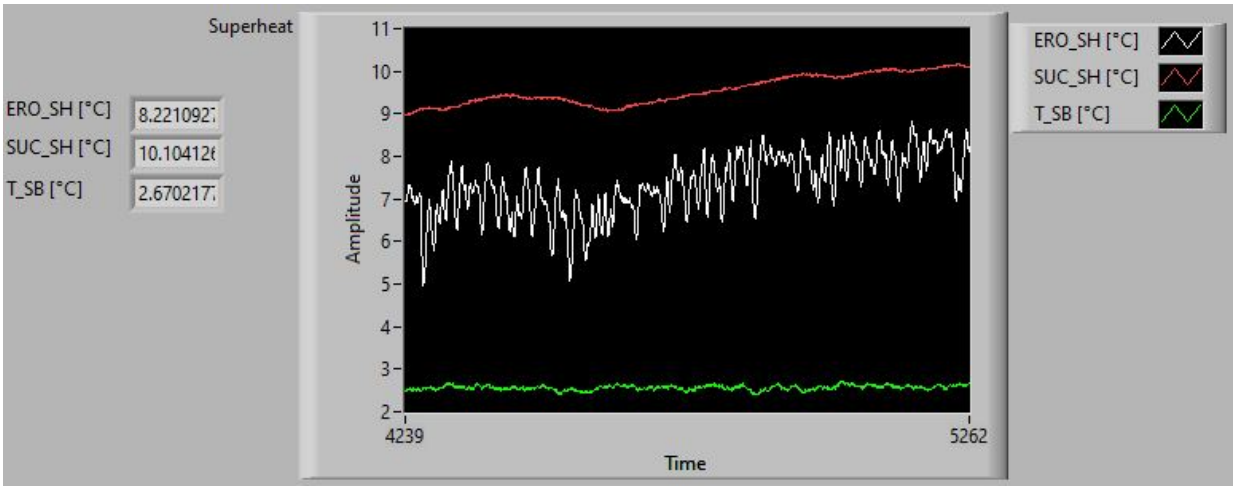

Figure 6.4: LabVIEW front panel for measurement of superheat.

6.2 Transfer Function Analysis of PI Controlled VCS

This section considers a digital PI controller for superheat regulation, which is predominantly used for industrial process control. For a given feedback controller (e.g., PID controller), a short execution time step could provide fast and accurate superheat regulation

but frequent actuation may reduce the lifetime of the valve and stepper motor; on the other hand, an excessively large execution time step setting can lead to control instability such as superheat hunting which may trigger control oscillations of both the EXV and compressor. Therefore, a proper setting of the control execution time step is critical to ensure reliable and efficient VCS operations.

Although PI controllers are focused, the analysis method presented here is applicable to general linear feedback controllers. Figure 6.5 shows the block diagram of the digital superheat control loop, where the PI controller accepts the superheat control error $\hat{T}_{sh,e}$ between the superheat setpoint $\hat{T}_{sh,s}$ and the measured superheat $\hat{T}_{sh,m}$, and generates the control command $\hat{\delta}$ for the EXV opening. Note that the symbol "^" denotes the discrete-time signal. The PI controller has the following discrete-time transfer function:

$$C(z) = \frac{\mathcal{Z}\{\hat{\delta}\}}{\mathcal{Z}\{\hat{T}_{sh,e}\}} = K_p + K_i \frac{\Delta T z}{z-1} \tag{6.1}$$

where K_p and K_i are the proportional and integral gains, respectively, ΔT is the execution time step of the controller, and $\mathcal{Z}$ is the Z-transform operator. Note that throughout this paper, a continuous-time signal is denoted by a regular variable while a discrete-time (sampled) signal is represented by a hatted variable.

The continuous-time transfer function of the VCS plant model is denoted by $H(s)$. Zero-order hold (ZOH) is applied to the discrete-time control command $\hat{\delta}$ generated by the PI controller to reconstruct a continuous-time and piece-wise constant signal δ fed to the VCS plant. The ZOH operator has the following transfer function (Landau and Zito, 2007[79])

$$K(s) = \frac{\mathcal{L}\{\hat{\delta}\}}{\mathcal{L}\{\delta\}} = \frac{1 - \mathrm{e}^{-s\Delta T}}{s} \tag{6.2}$$

where $\mathcal{L}$ is the Laplace-transform operator. A sampler is present after the VCS plant to obtain a discrete-time superheat signal ($\hat{T}_{sh,m}$). The discrete-time equivalent VCS plant model

with the ZOH process is represented by $KH(z)$.

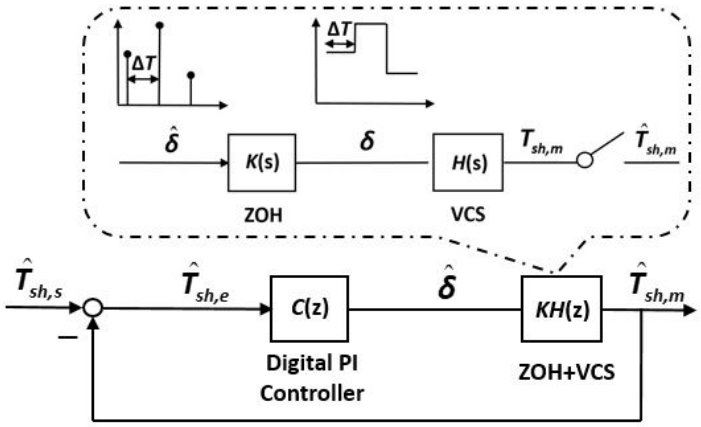

Figure 6.5: Block diagram of the digital superheat controller.

The original gray-box VCS plant model described in the Chapter 5 is highly nonlinear and includes differential algebraic equations and, thereby not suitable for control analysis. To this end, a linear surrogate model is derived in the following manner: for given operating conditions, step response tests are conducted with the developed gray-box VCS model and the offline simulation data is used to fit a first-order linear time-invariant surrogate model (Rasmussen, 2012[18])

$$H(s) = \frac{\mathscr{L}\{T_{sh,m}\}}{\mathscr{L}\{\delta\}} = \frac{K_e}{1+\tau s} \tag{6.3}$$

where τ is the time constant and K_e is the DC gain of the surrogate model, which is equal to the variation of the steady-state superheat subject to a unit step change in the EXV opening. Note that both the time constant and the DC gain change with operating conditions and the analysis results are only valid for the conditions under which the surrogate model is developed. When the operation conditions change, the surrogate model ought to be updated. The discrete-time equivalent model of the VCS plant with the ZOH process is:

$$KH(z) = \frac{\mathscr{Z}\{\hat{T}_{sh,m}\}}{\mathscr{Z}\{\hat{\delta}\}} = \frac{K_e\left(1-\mathrm{e}^{-\frac{\Delta T}{\tau}}\right)}{z-\mathrm{e}^{-\frac{\Delta T}{\tau}}} \tag{6.4}$$

Then, the closed-loop discrete-time transfer function for the superheat control system is:

$$G(z) = \frac{\mathcal{Z}\{\hat{T}_{sh,m}\}}{\mathcal{Z}\{\hat{T}_{sh,s}\}} = \frac{C(z)\,KH(z)}{1 + C(z)\,KH(z)} = \frac{Bz + D}{z^2 + Ez + F} \tag{6.5}$$

where

$$\begin{aligned}
B &= K_e\left(K_p + K_i\Delta T\right)\left(1 - \mathrm{e}^{-\frac{\Delta T}{\tau}}\right), \\
D &= -K_eK_p\left(1 - \mathrm{e}^{-\frac{\Delta T}{\tau}}\right), \\
E &= K_e\left(K_p + K_i\Delta T\right)\left(1 - \mathrm{e}^{-\frac{\Delta T}{\tau}}\right) - \left(1 + \mathrm{e}^{-\frac{\Delta T}{\tau}}\right), \\
F &= \mathrm{e}^{-\frac{\Delta T}{\tau}} - K_eK_p\left(1 - \mathrm{e}^{-\frac{\Delta T}{\tau}}\right).
\end{aligned}$$

Discrete-time closed-loop stability can be guaranteed if all the closed-loop poles, which are the roots of the characteristic equation $z^2 + Ez + F$, fall within the unit circle in the z-plane (Fadali and Visioli, 2013[80]). This stability criterion is used to analyze the effect of control execution time step ΔT on system stability.

6.3 Case Study Results on Control Stability

6.3.1 Surrogate Model-Informed Stability

Figure 6.6 depicts the variation of the distance between the dominant pole of the closed-loop system and the origin of the z-plane with respect to the control execution time step, under different P/I gain settings. The analysis corresponds to the following boundary conditions: evaporator inlet air dry-bulb temperature of 305K and relative humidity of 35%, outdoor air dry-bulb temperature of 300K, compressor speed at 3000 RPM and supply air flow rate of 1200 CFM. The Ziegler–Nichols rule (Katsuhiko, 2010 [81]) was used to fine tune the P/I gains with the full VCS model under the same operating conditions. The

P/I gains were determined to be 2 (step/K) and 0.09 (step/K/sec), respectively. Open-loop simulation tests were conducted under the same conditions and the results were utilized for estimation of the surrogate model, the time constant τ and DC gain K_e of which were identified to be 41.5 s and 7.112 (K/step), respectively. The results presented in Figure 6.6 were obtained using the estimated surrogate model for the specific boundary conditions. It can be observed that for all considered P/I gain settings, the dominant pole's distance from the origin increases monotonically with the increase of the control execution time step and when the control time step reaches certain threshold, the closed-loop pole crosses the unit circle and the system becomes unstable. This threshold is termed critical execution time step ΔT_c, which is a critical parameter to consider in the design of a digital controller: the control time step needs to be smaller than this threshold to maintain stability of the closed-loop system. Another key observation is that the critical time step varies dramatically with the P/I gain settings: the increase of the P or I gain, which corresponds to more aggressive control reactions to superheat errors, leads to a decrease of ΔT_c. This is expected as more frequent control actuation is needed to accommodate the dramatic changes in the control command by an aggressive PI controller.

To investigate the effect of operating conditions on the critical time step, analyses were performed for a different set of boundary conditions: the evaporator inlet/outdoor air conditions remained the same as those in Figure 6.6 but the compressor speed and supply air flow rate were changed to 3500 RPM and 1800 CFM, respectively. The results are depicted in Figure 6.7. The VCS response is quite different under the new boundary conditions and the surrogate VCS model was re-identified accordingly. The updated surrogate model has a slightly larger time constant and a significantly smaller DC gain. Although the curves exhibit similar trends, the critical time step ΔT_c has changed quite significantly as a consequence of the variation in system dynamics. For the nominal P/I gain settings of 2 (step/K) and 0.09 (step/K/sec), the critical time step has increased from 6.09 s to 9.45 s after the changes in the boundary conditions. These results indicate the promise of an improved strategy to

adapt the control execution time step with the operating conditions, which can offer benefits of reducing control actuation and prolonging equipment lifetime with guaranteed stability. However, this is out of the scope of this dissertation.

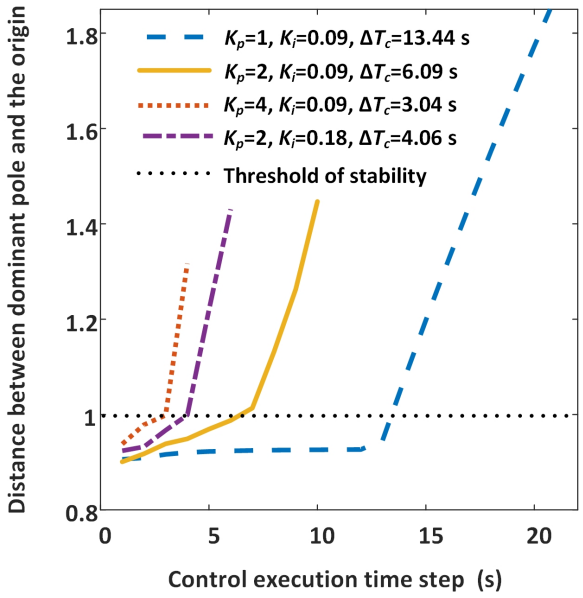

Figure 6.6: Variation of distance between dominant pole and the origin with respect to the control execution time step for $\tau = 41.5\text{s}, K_e = 7.112\text{K/step}$.

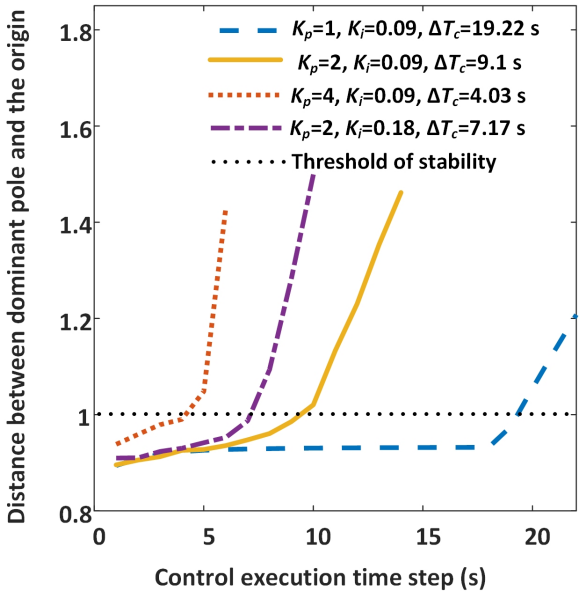

Figure 6.7: Variation of distance between dominant pole and the origin with respect to the control execution time step for $\tau = 36.5\text{s}, K_e = 3.875\text{K/step}$.

6.3.2 Experimental Validation of the Stability Results

Experimental tests were carried out using the test unit to validate the stability results presented in Section 6.3.1. The test assumed the same operating conditions as those in Figure 6.6 and the nominal P/I gains of 2 (step/K) and 0.09 (step/K/sec). In the experiments, all boundary conditions and P/I gains remained constant while the PI controller execution time step was gradually increased from 2 s to 14 s with a 2 s increment. Each execution time step setting lasted 30 minutes to ensure the system reached steady- or oscillatory-steady-state before the next setting was applied.

Figure 6.8 presents the experimental results. It can be observed that the system was stable for controller execution time steps shorter than 6 s, while unstable superheat oscillations occurred when ΔT was increased to 8 s and the control response became more oscillatory as ΔT was further increased. These results are consistent with the critical execution time step of 6.09 s, identified in the stability analysis of Section 6.3.1. The dominant pole's distance from the origin is indicated for each execution time step setting in the first subplot of Figure 6.8, which also proves that ΔT of 6 s is very close to the stability threshold with the dominant pole almost falling on the unit circle. It may be noted that a larger control execution time step is anticipated to reduce mechanical wear and tear of the valve and stepper motor. However, an excessively large control time step may cause system instability and control chattering which can even accelerate the aging of the expansion device, as evidenced by the results in Figure 6.8.

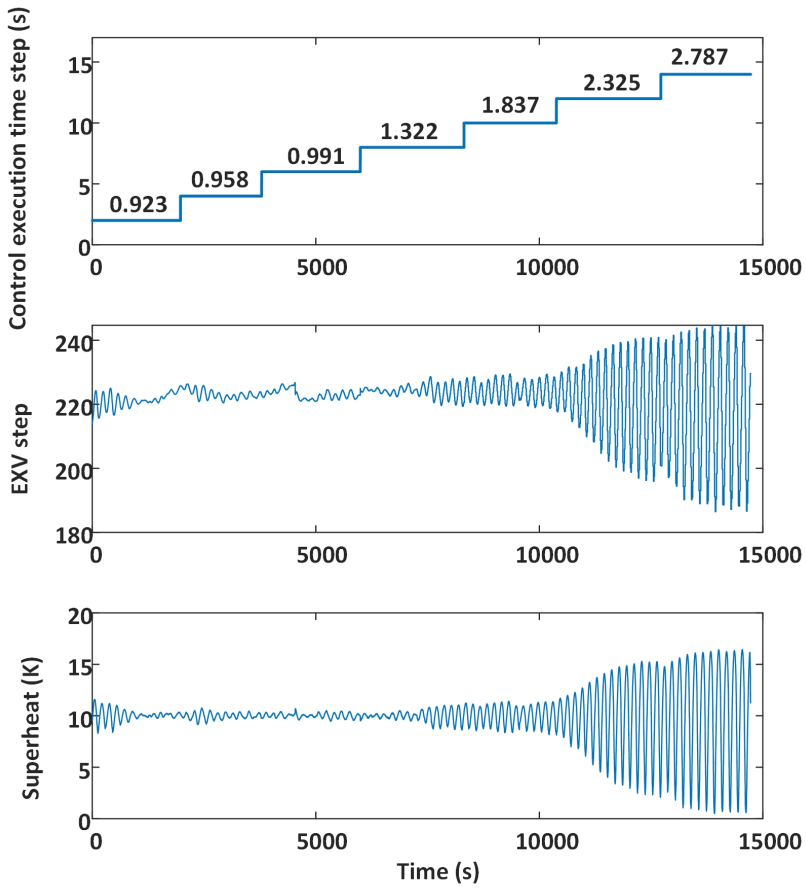

Figure 6.8: Experimental results under different control execution time step.

6.4 Chapter Summary

This chapter presented the first application of the developed dynamic model for control analysis. Specifically, the developed dynamic model has been utilized for stability analysis of a digital PI controller, with a particular goal of identifying the maximum EXV control execution time step to attain stable operation with minimum EXV lifetime impact. To the author's knowledge, this is the first attempt in analyzing digital control stability of VCS with respect to control decision time interval. In the analysis, the nonlinear VCS model was linearized at given operating conditions and digital control theory was applied to evaluate the feedback control stability. The case study results showed that the stability threshold for the

PI control execution time step could change significantly, from 3 sec to 19 sec, as the operating conditions and P/I control settings vary, and a proper selection of the execution time step is critical to ensure stable and reliable operations.

Chapter 7: Improved Superheat Control under Provision of Fast Balancing Services

This chapter starts with an introduction of opportunities of using VCS for fast balancing services to the electric grid. Then it reports superheat control problems observed in the previous experiments that involved dramatic compressor speed changes during provision of fast balancing services, e.g., frequency regulation and PV smoothing. To improve the superheat regulation performance, a new control strategy is presented, wherein a traditional PI feedback controller is combined with a gain-scheduled feed-forward block to mitigate the disturbance effect associated with sudden compressor speed changes. Subsequent discussions include simulation and experimental tests utilized to demonstrate the efficacy of the proposed controller in improving the superheat stability and system energy efficiency.

7.1 Superheat Control Issue

This section firstly introduces the background of fast ancillary services that motivated development of an improved superheat control strategy and then discusses the superheat control problem observed in prior fast balancing experiments. This problem is illustrated through both experimental and simulation tests using the test heat pump.

7.1.1 Background of Fast Ancillary Services

Increasing penetration of renewable energy resources, e.g., solar and wind, causes challenges to sustain reliable and efficient operations of the electric grid. Driven by the increased generation uncertainties, the power market has seen record demand for procurement

of fast ancillary services, e.g., frequency regulation. Vapor compression-based loads are recognized as low-cost resources for grid reliability support. The use of VCS for ancillary services in various forms has been studied in recent years, including frequency regulation (Cai amd Braun, 2019[82]), smoothing control of solar PV (Jiang et al., 2020[83]), distribution voltage regulation (Elhefny et al., 2022[84]), etc.

In provision of ancillary services, the compressor speed of a VCS is modulated to follow a reference power signal sent by system operators, and depending on how accurately the signal is followed, the resource can receive a payment for the services offered. In fast ancillary services, the reference power signal can change drastically every few seconds which would require aggressive modulation of the compressor speed and could cause challenges in superheat regulation. It is widely known that evaporator superheat affects both system efficiency and reliability. A low superheat can lead to control instability and occasional wet compression that may cause catastrophic failure of the compressor. On the other hand, excessively high superheat may result in low COP. Therefore, appropriate superheat control is critical in achieving maximum system efficiency and reliable operation.

7.1.2 Overview of Superheat Control

As discussed in Chapter 6, EXV regulates the refrigerant mass flow to achieve desired superheat. There is a trade-off between efficiency and operational safety in the superheat setting: a high superheat results in larger safety margins for the compressor but comes at the cost of lower energy efficiency. Appropriate superheat setpoints range from 5K to 15K. VCSs are operated under a wide range of boundary and load conditions and are subject to different types of transient disturbances. Based on the induced transient behavior, superheat control disturbances are classified as either internal or external:

- **Internal disturbances:** Disturbances that directly and immediately alter the flow rate

or thermodynamic states of the primary fluid (refrigerant) are classified as internal disturbances. Internal disturbances, such as compressor speed changes and opening/closing of refrigerant bypass valves, can have immediate impact on the evaporator superheat by drastically altering the saturation pressure.

- **External disturbances:** External disturbances to the evaporator include variations in the flow rate and thermodynamic status of secondary fluid, e.g., return airflow and temperature changes. Since these disturbances only affect the refrigerant pressures indirectly through heat transfer across the fin-and-tubes, the impact to evaporator superheat is slower and milder compared to that of internal disturbances.

During provision of fast balancing services, the compressor speed modulation represents internal disturbances that have immediate impacts on superheat. Mitigation of such internal disturbance effect is challenging but is what this chapter aims to address.

7.1.3 Baseline Superheat Control Results and Issues

Experimental tests were carried out using a traditional PI feedback controller to illustrate the superheat control issue, demonstrate the necessity of the proposed control strategy and validate the accuracy of the established gray-box model. In the experiments, the setpoints for indoor/outdoor air temperatures assumed 295K and 305K, respectively, while the evaporator air flow rate was fixed at 1400 CFM. The P/I gain settings of the OEM superheat controller were recovered through offline tests of the EXV: the superheat setpoint was perturbed in the tests and the EXV control action by the OEM superheat controller was recorded along with the superheat error; the obtained results were used in estimation of the P/I gains of the OEM controller, which were determined to be approximately 2 (step/K) and 0.01 (step/K/sec), respectively. The estimated P/I gains were assumed for all the experimental and simulation tests reported in this study. To minimize mechanical wear and tear of the

EXV, the OEM superheat controller executes EXV control actuation every 10 s and the same setting was used in the experiments.

Simulations were also carried out using the calibrated dynamic model, with a simulation time step of 0.05 s. The measured boundary conditions were fed into the simulation tests and the same control settings (e.g., PI gains, control execution time steps) were used in order to evaluate the accuracy of the model compared to actual system responses. Figure 7.1 shows the comparisons of superheat and EXV opening between the experiment and simulation. In this experiment, all boundary conditions and control settings were maintained constant until time 1400 s when the compressor speed was suddenly reduced from 3500 RPM to 1500 RPM. The experimental and simulation results show a good agreement. It can also be observed that the superheat (for both experiment and simulation) drifted from the setpoint (10K) and dropped to 0K following the compressor ramp-down, indicating the presence of wet compression, which can cause damage and pre-mature failures of the compressor. The results show that drastic change of compressor speed, which can occur frequently during provision of fast load balancing services, affect the superheat regulation, highlighting the necessity of an improved control approach with better dynamic disturbance mitigation ability.

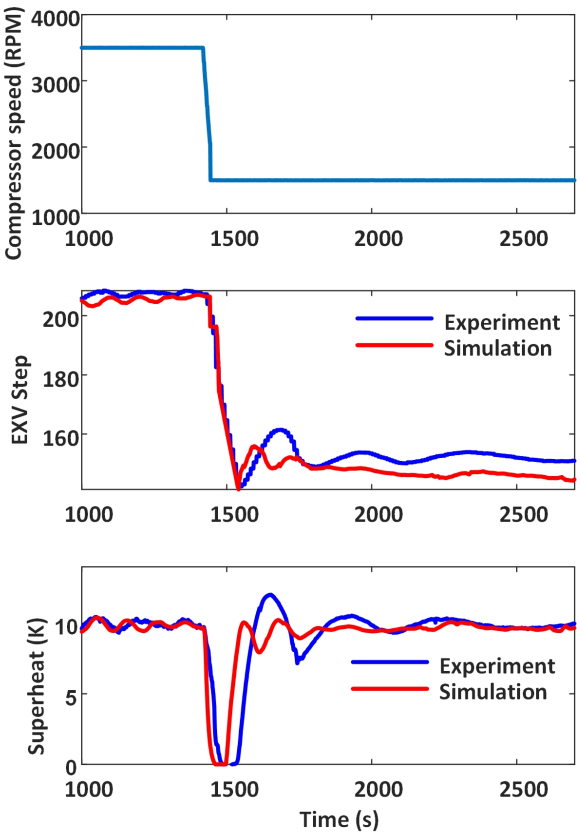

Figure 7.1: Baseline superheat control results between experiment and simulation under PI control.

7.1.4 Causes of Superheat Control Issues

As can be observed in the first subplot of Figure 7.1, the descent of the compressor speed followed a constant ramp rate of approximately 50 RPM/s, although an immediate speed change command was sent to the unit. From the spec sheet of the compressor variable frequency drive, the default ramp rate for both upward and downward ramping is 50 RPM/s but can be adjusted to up to 360 RPM/s through proprietary software.

To investigate whether the ramp rate of compressor speed has any effect on the superheat regulation performance, a parametric simulation analysis was carried out, in which the boundary conditions and controller settings were kept the same as the baseline test while

different compressor ramp rates were implemented. Figure 7.2 depicts the comparisons of superheat responses with ramp rates of 50 RPM/s, 10 RPM/s and 5 RPM/s. The simulation results verified that the superheat regulation problem is severer with higher compressor ramp rates; when a ramp rate of less than 10 RPM/s is used, wet compression can be completely avoided with the traditional PI controller, because a small ramp rate would allow adequate time for the feedback controller to respond and take remedial actions. However, high ramp rates are always preferred for fast load balancing services. For example, the dynamic frequency regulation service (RegD) is paid at a much higher price compared to the slow regulation service (RegA); PV smoothing control also requires high ramp rates from mitigation resources as solar irradiance can vary dramatically within a few seconds due to passing clouds. It is worth noting that the ramp rate of 50 RPM/s was applied for all the remaining tests presented in this chapter.

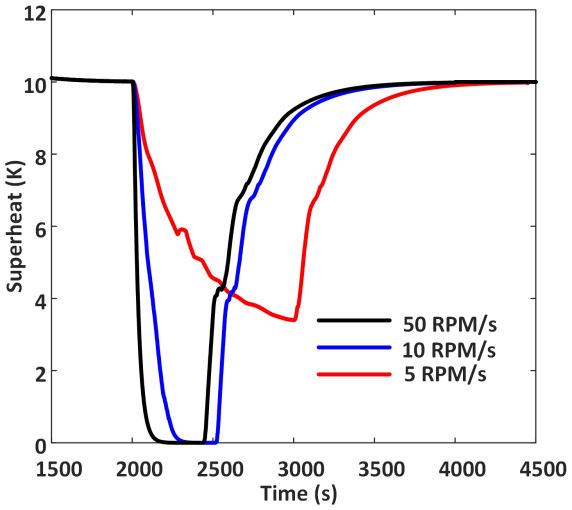

Figure 7.2: Simulated superheat responses to different compressor ramp rates.

Another possible factor that needs to be considered is the execution time step of the feedback PI controller. As explained in Section 7.1.3, a 10-s time step is adopted by the OEM controller for the sake of EXV lifetime. A simulation test was conducted with a 1-s control time step and the results are compared to those of the baseline with 10-s time step,

as shown in Figure 7.3. The two response curves are almost overlapping, which rules out the effect of control time setting.

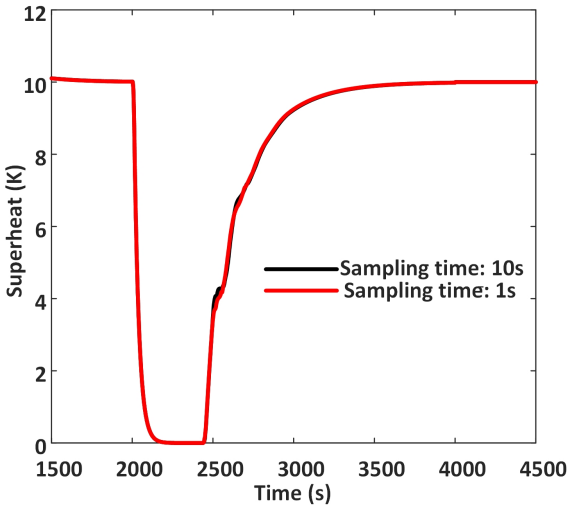

Figure 7.3: Simulated superheat responses under different control time step settings.

It is widely known that PI controllers are effective in rejecting disturbances with slow variations. However, internal disturbances such as changes of compressor speed can have an immediate effect on the superheat and therefore cannot be mitigated by feedback controllers. In addition, PI controllers can take corrective actions only after the process output (superheat) has drifted from the setpoint; the delay in the reading of temperature sensors can exacerbate the superheat regulation problem (Xia and Deng, 2016[85]). This finding motivated the proposed feedforward + PI controller to be discussed in the next section.

7.2 Gain-Scheduled Feedforward + PI Control

7.2.1 Control Architecture

As highlighted in the Section 7.1.3, sudden changes of compressor speed can disturb the superheat, and traditional feedback controller may not be able to maintain a positive su-

perheat and thereby may jeopardize safe operation of a VCS. The control stability issue is also partially due to the separate control loops used for the EXV opening and compressor speed, which work well traditionally for a VCS subject to slowly varying boundary conditions. However, for provision of fast ancillary services, the traditional approach fails and a PI control strategy is proposed combined with a feedforward action, that uses the real-time compressor speed available in a VCS central controller to proactively compensate for its disturbance effect. In addition, the DC gain of the feedforward block is varied with the evaporator air flow rate and temperature to further improve the superheat performance by accounting for the disturbance effect of the slowly varying boundary conditions. All these disturbances measured by the VCS central controller are used to adjust the EXV position to make corrective actions before the superheat drifts too far away from its setpoint. The proposed gain-scheduled feedforward + PI controller has the following formulation

$$\delta\left(n\right) = K_p T_{sh,e}\left(n\right) + K_i \sum_{i=1}^{n} T_{sh,e}\left(i\right) + \delta_F\left(n\right) \tag{7.1}$$

where δ is the EXV opening in step (0 to 500 with a fully closed valve at 0 step and fully open valve at 500 steps), n indicates the n^{th} sampling time, K_p and K_i are the (discrete-time) P and I gains of the PI controller, respectively, and $T_{sh,e}$ is the error between the measured superheat $T_{sh,m}$ and its setpoint $T_{sh,s}$. The first two terms in Equation 7.1 represent the proportional and integral actions of a traditional PI controller (Franklin et al., 2015[86]) while the third term, δ_F, represents the proposed gain-scheduled feedforward control action to compensate for the effect of drastic compressor speed changes, which is calculated with

$$\delta_F\left(n\right) = \sigma(n)\left(\sum_{i=1}^{n_u} \lambda_{u,i}\omega\left(n-i\right) + \sum_{i=1}^{n_y} \lambda_{y,i}\delta_F\left(n-i\right)\right) \tag{7.2}$$

where σ is the gain for the feedforward action, which is adjusted based on the operating conditions; n_u, n_y are the degrees of the numerator and denominator polynomials in z^{-1} of the feedforward transfer function; λ are the coefficients of the transfer function polynomials;

ω is the compressor speed. The determination of the feedforward gain and transfer function is discussed in the following sections.

Figure 7.4 shows a block diagram of the proposed controller. The fast balancing controller converts a reference power signal of a given ancillary service into a compressor speed command. The variable compressor speed represents an external disturbance to the evaporator superheat; the disturbance transfer function is denoted by $G(s)$. The response of superheat to the EXV opening is characterized by the plant transfer function $H(s)$. The actual compressor speed, along with other influencing disturbances such as evaporator air flow rate v_f and return air temperature T_{eai}, is fed to the feedforward controller, represented by the transfer function $K(s)$.

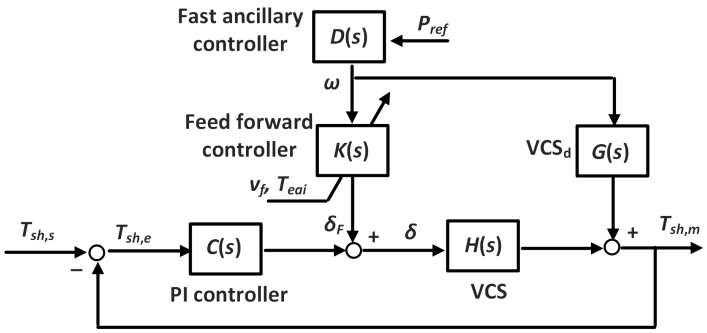

Figure 7.4: Block diagram of the proposed feedforward + PI controller.

7.2.2 Scheduling of Feedforward Gain

To accommodate the nonlinearity of a VCS, the feedforward control gain σ is adapted with variations of measurable boundary conditions. To investigate an appropriate functional relationship between controller gain σ and operation conditions, parametric dynamic simulations were conducted under the traditional PI control (without feedforward block). The simulations covered a pre-defined set of different combinations of boundary conditions, shown in Table 8.1, where the range of evaporator air inlet temperature was selected based on the measured mixed air temperature in an air-handling unit serving a campus building of Uni-

versity of Oklahoma over the month of July 2020, and the outdoor air temperature range was based on ambient temperature measurements of the same month for Oklahoma City. The temperature upper and lower limits were determined as the 95 percentile of the respective measurements, rounded to the nearest multiple of 5K. The ranges of compressor speed and evaporator air flow rate followed suggestions by the manufacturer of the test unit for a design outdoor temperature of 308K. For each operating condition, a continuous dynamic simulation was carried out sweeping through a sequence of step changes in the compressor speed, from 3500 RPM to 1500 RPM with a 100 RPM increment. Each compressor speed was held constant within a 20-min time window for the system to reach steady state, in which the PI controller identified the new EXV opening to maintain the desired 10K superheat. The obtained EXV step was recorded together with all boundary conditions and compressor speeds, to be used for estimation of the feedforward gains.

Table 7.1: Range of operating variables

Operating variables	**Range**
Evaporator air flow rate (CFM)	1000-1800
Compressor speed (RPM)	1500-3500
Evaporator air inlet temperature (K)	290-300
Outdoor air temperature (K)	295-310

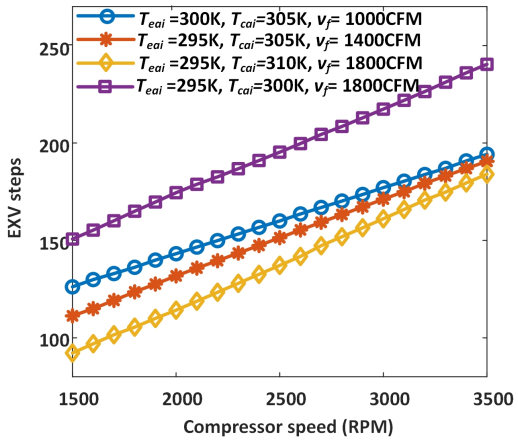

Figure 7.5: Variation of EXV step to achieve 10°K superheat with different compressor speed.

Example simulation results are depicted in Figure 7.5. It can be observed that for each operating condition, the relationship between EXV opening and compressor speed in achieving the same superheat is nearly linear, i.e., there is an approximately constant change of EXV opening corresponding to each 100 RPM change of the compressor speed. The feedforward control gain σ should be set equal to the slope of the EXV-compressor speed line, which clearly varies with the boundary conditions. The results show that the slope is not sensitive to the outdoor temperature but is highly dependent on the evaporator inlet air temperature and evaporator air flow rate. Therefore, the following functional relationship was developed to correlate the feedforward control gain with these two boundary conditions:

$$\sigma = \gamma_1 v_f + \gamma_2 T_{eai} + \gamma_3 v_f \cdot T_{eai} + \gamma_4 v_f^2 + \gamma_5 \tag{7.3}$$

where γ_1 to γ_5 are the correlation coefficients. Figure 7.6 and Figure 7.7 show the curve fit results. The scattered points correspond to the results from the parametric dynamic simulations while the curves represent the predicted feedforward control gain using the estimated model of Equation 7.3. The model exhibits a good agreement with the simulation test results.

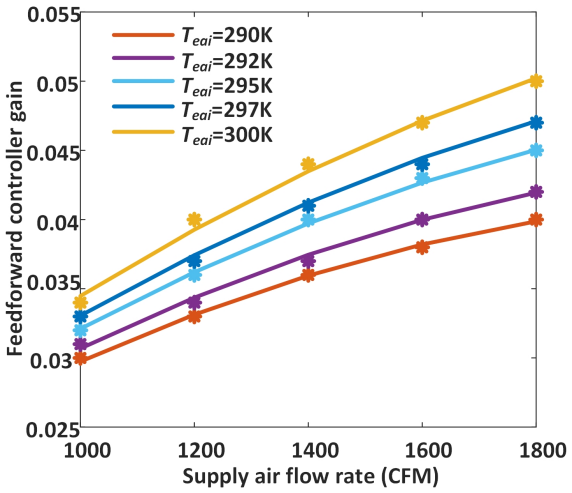

Figure 7.6: Comparisons of feedforward gain with respect to evaporator air flow rate between the correlation and simulation test results.

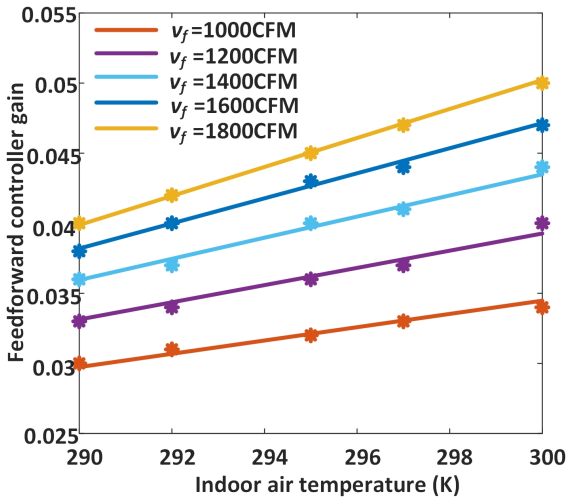

Figure 7.7: Comparisons of feedforward gain with respect to evaporator air inlet temperature between the correlation and simulation test results.

7.2.3 Transfer Function of the Feedforward Controller

As depicted in Figure 7.4, $C(s)$, $H(s)$ and $G(s)$ represent the transfer functions of the PI controller, the dynamics of superheat in response to EXV opening and the disturbance effect from compressor speed, respectively. The feedforward controller $K(s)$ should

be designed to effectively eliminate the disturbance effect of the compressor speed on the evaporator superheat, i.e., the following disturbance closed-loop transfer function should be maintained small and close to 0

$$\frac{K(s) \cdot H(s) + G(s)}{1 + C(s) \cdot H(s)} \tag{7.4}$$

which can be satisfied with $K(s) = -\frac{G(s)}{H(s)}$. It is clear that the plant and disturbance transfer functions ($H(s)$ and $G(s)$) need to be estimated for the synthesis of the feedforward controller.

Open-loop step response simulation tests were conducted to facilitate identification of the disturbance transfer function $G(s)$, with identical boundary conditions shown in Table 8.1. Each test started with a 10-min warmup period for the system to reach steady state; at the end of the warmup period, a step change was imposed on the compressor speed while all other operating conditions, including the EXV opening, were held constant. Simulation results of example cases are depicted in Figure 7.8, with the superheat response normalized to enable comparison across different operating conditions. It is evident that the normalized superheat response curves for the different cases are almost overlapping, indicating the (normalized) disturbance transfer function $G'(s)$ is invariant with operating conditions. The results were used with the aid of the Matlab System Identification Toolbox (Ljung, 1999[55]) in identifying the following third-order transfer function for $G'(s)$

$$G'(s) = \frac{-5.634\text{e}^{-4}s + 2.371\text{e}^{-4}}{s^3 + 0.1635s^2 + 0.01203s + 2.371\text{e}^{-4}} \tag{7.5}$$

The simulated response with the identified model is also plotted in Figure 7.8, which shows very good agreement with the simulation results of the high-fidelity VCS model.

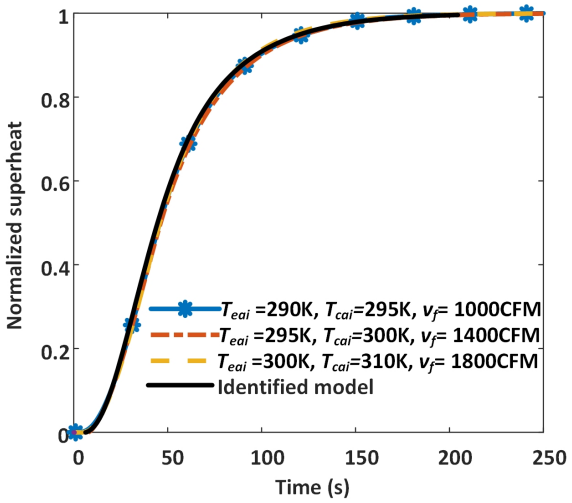

Figure 7.8: Comparison of normalized superheat responses to compressor speed step changes under different boundary conditions.

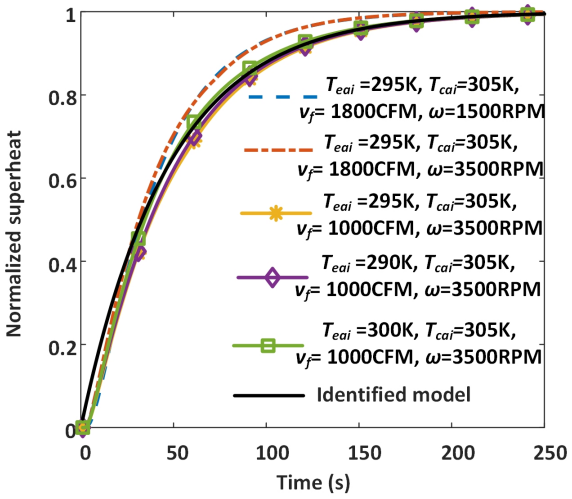

Figure 7.9: Comparison of normalized superheat responses to EXV opening step changes under different boundary conditions.

Similar open-loop step response simulation tests were performed for identification of the normalized plant transfer function $H'(s)$. In these simulations, step changes were artificially injected to the EXV opening while other operating conditions were maintained constant. Example simulation results are shown in Figure 7.9. It can be observed that the evaporator air flow rate has the most significant impact on the superheat response to EXV

opening: the two response curves corresponding to the evaporator airflow rate of 1800 CFM are almost overlapping, while the three alike curves associated with the airflow rate of 1000 CFM show much slower responses compared to the higher airflow cases. This is expected as the rate of heat propagation through the heat exchanger wall is highly dependent on the evaporator airflow rate and this behavior is consistent with prior studies (e.g, Xia et al., 2019[32], Yan et al., 2019[87]). However, for a given boundary condition, the response curve is close to that of a first order system (also consistent with previous work such as Rasmussen, 2012[18]). An average response curve was obtained from all simulated responses, which was used in identification of the first order transfer function for $H'(s)$. The response of the first-order surrogate model is shown in Figure 7.9 and the estimated transfer function is:

$$H'(s) = \frac{-1}{47.3908s + 1} \tag{7.6}$$

From Equation 7.4, the feedforward controller has a transfer function of $K(s) = \sigma K'(s)$ where the unity-gain feedforward transfer function $K'(s)$ is

$$K'(s) = -\frac{G'(s)}{H'(s)} = \frac{-0.0267s^2 + 0.0106s + 2.371\mathrm{e}^{-4}}{s^3 + 0.1635s^2 + 0.01203s + 2.371\mathrm{e}^{-4}} \tag{7.7}$$

This continuous-time transfer function (s domain) was converted into the following discrete-time transfer function (z domain, Fadali and Visioli, 2013[80])

$$K'(z) = \frac{0.2196z^{-1} + 0.1568z^{-2} - 0.2705z^{-3}}{1 - 1.59z^{-1} + 0.8909z^{-2} - 0.195z^{-3}} \tag{7.8}$$

where z^{-1} is a time shifting operator so the above discrete-time transfer function recovers the time series formulation given in Equation 7.2.

7.3 Control Performance Validation

The proposed control approach was validated with both simulation and experimental tests. The simulation-based validation, based on the dynamic model developed in Chapter 5, firstly evaluates the control performance under step changes of compressor speed, which represents the worse-case scenario with the most aggressive disturbance. The subsequent sections present the simulation-based assessments of the control performance under two representative fast ancillary services, namely fast frequency regulation and PV smoothing. Section 7.3.2 presents the experimental validation results against step changes in compressor speed.

7.3.1 Simulation-Based Validation

Mitigation of Disturbance Effect from Step Changes in Compressor Speed

The compressor speed undergoing a step change, either upward or downward, between the speed upper and lower limits, presents a worst-case disturbance that a VCS system can experience in terms of superheat regulation. Such drastic compressor speed changes are not common in daily VCS operations (except during start-up and shut-down) but could be frequently encountered in provision of fast ancillary services. The proposed control strategy was firstly evaluated under this worst-case scenario to validate the feasibility and potential limitations.

Two simulation tests, one for ramp-up and the other for ramp-down in compressor speed, were carried out under representative boundary conditions, i.e., T_{eai} = 290K, v_f = 1000 CFM and T_{cai} = 305K. The PI gain settings and the control time step were identical to those in the baseline test presented in Section 7.1.3 to enable fair comparison. A ramp rate of 50 RPM/s was applied during these tests (same as baseline). For the ramp-down test, the

compressor speed was firstly operated at 3500 RPM until the system reached a steady state; then a sudden ramp-down to 1500 RPM was injected and the simulation continued until the superheat returned to its setpoint. The ramp-up test followed the same operation sequence except that the compressor speed was changed in the opposite direction.

Figure 7.10 shows the ramp-down test results. The first subplot compares the variations of EXV opening under the baseline and the proposed controller, along with the compressor speed profile, while the second subplot depicts the resultant superheat responses of the two controllers. It can be seen that after the sudden compressor speed drop (3500→1500 RPM), the baseline PI controller had not much response until the superheat control error built up, and it took a long time, almost 1000 s, for the integral action to catch up and completely offset the disturbance effect. Because of the slow response, the superheat under the traditional PI controller dropped to and remained at 0K for several minutes before it eventually re-settled at the setpoint. This caused wet compression lasting for a few minutes. In contrast, the feedforward action of the proposed controller sensed the compressor speed drop and took counteracting control actuation (close the valve) immediately so the superheat could be maintained positive preventing harmful wet compression. A comparison of Figure 7.8 and Figure 7.9 reveals that the superheat response to EXV opening is slightly slower than the response to compressor speed changes. This difference is explicitly captured by the feedforward controller $K(s)$, which led to a slight over-compensation in the control action (see first subplot of Figure 7.10) for maximum disturbance mitigation.

Figure 7.11 shows the compressor ramp-up test results. The compressor speed ramp-up would cause the superheat to drift upwards, so wet compression is not a concern in this case. After a sudden increase of the compressor speed (1500→3500 RPM), the superheat of the PI controller went through a significant overshoot and it took a long time for it to come back to its setpoint. This superheat overshoot has reduced the system energy efficiency (coefficient of performance, or COP) as shown in the third subplot. Nevertheless, the proposed

controller could take compensating actions against the sudden compressor speed increase and provided improved superheat regulation performance with less fluctuation and higher overall COP.

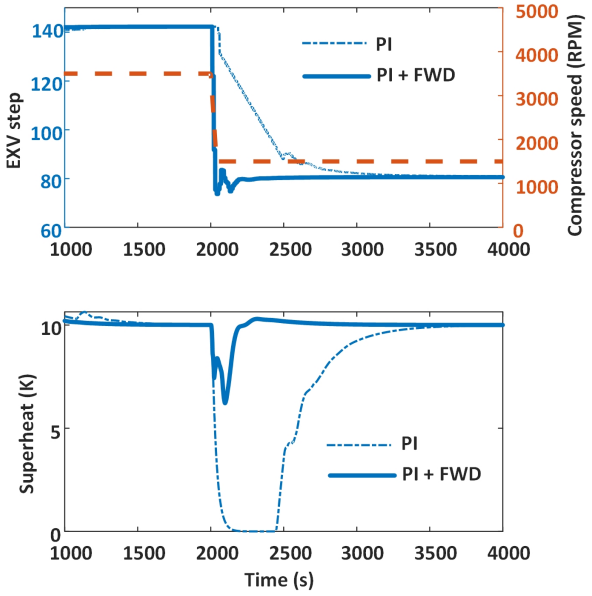

Figure 7.10: Simulation results for the compressor speed ramp-down test.

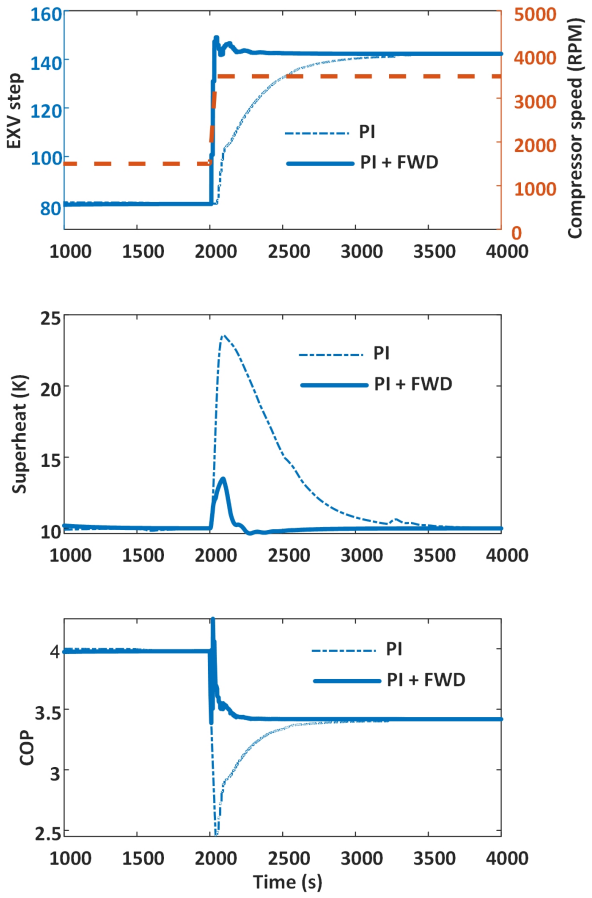

Figure 7.11: Simulation results for the compressor speed ramp-up test.

Disturbance Rejection for Frequency Regulation

The power grid has seen record increase in renewable energy integration. Most of the renewable energy resources, such as solar power and wind, are intermittent and highly uncertain, which cause stresses on the power grid in matching real-time power supply and demand and maintaining a stable power frequency. As one of ancillary services procured by system operators, frequency regulation aims to balance the transmission system as it moves electricity from generating sources to consumers. In a frequency regulation market, a regulation power signal, generated by the system operator based on the area control error, is broadcast to the participating resources every few seconds, as a means to steer the instan-

taneous power supply/demand up or down to offset any power imbalances. If a resource is able to accurately follow the regulation signal, a monetary credit can be earned. Frequency regulation can involve very aggressive power modulation and thereby is regarded as one of the highest-value services (Zhou et al., 2016[88]).

The Pennsylvania–New Jersey–Maryland Interconnection (PJM) market is most favorable for demand-side regulation resources and thereby PJM test signals are used for performance assessment in this chapter. The PJM dynamic regulation service (called RegD) requires the most aggressive variation of the resource power, which is directly related to the compressor speed for a VCS-type resource. Assuming the compressor speed and power are linearly related, the RegD signal downloaded from PJM (2021)[89] website can be linearly projected to the operating range of compressor speed (1500 to 3500 RPM); this treatment eliminates the requirement of a frequency regulation controller (practical VCS frequency regulation controllers can be found in Cai and Braun, 2019[82]).

Figure 7.12 shows the compressor speed input in the top subplot, the EXV steps in the middle subplot, and the comparison of the simulated superheat in the bottom subplot, under the traditional PI controller and the proposed controller for a PJM RegD test. It can be observed that the superheat under the traditional PI controller underwent significant fluctuations due to the aggressive compressor speed adjustment required by provision of RegD service. After a major RegD signal ramp-down at time around 800 s, the superheat dropped to zero and the wet compression lasted for approximately 4 minutes. The proposed controller was effective in mitigating this oscillation and led to much improved regulation of the superheat around its setpoint of 10K. More importantly, the proposed controller was successful in avoiding wet compression throughout the entire simulation period.

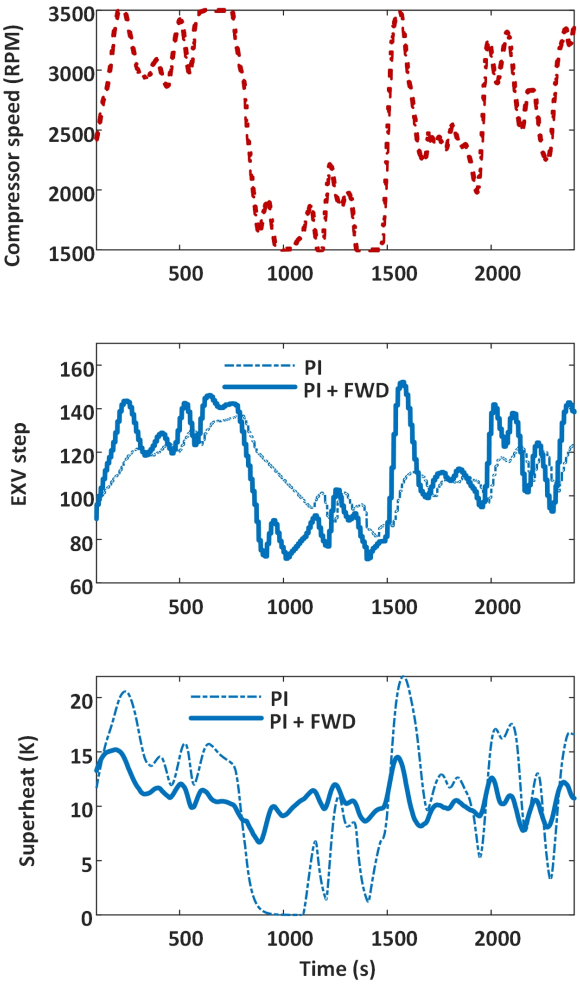

Figure 7.12: Simulation results under RegD frequency regulation.

Disturbance Mitigation under PV Smoothing

The increasing deployment of PV generation, especially those tied to the distribution grids, has caused reliability and stability concerns, due to 1) the misalignment of the peak demand and renewable generation and 2) the uncertainty of power availability from solar resources. Frequency regulation can counteract the solar volatility on a transmission level; but it cannot help solve and in some cases may even exacerbate the distribution grid reliability issues caused by distributed PV generation. Numerous mitigation methods were thereby introduced to directly attenuate the aggressive fluctuations of PV output, including the use

of smart power inverters (Tonkoski et al., 2010[90]) and energy storage (Wang et al., 2014[91]). Very recently, Dr. Cai's team has demonstrated the technical feasibility of using variable-speed VCS to smooth on-site solar PV generation (Jiang et al., 2020[83]). Various benefits of PV smoothing control to the distribution grid have been shown, including reduced variation of distribution voltage and reduced operations of step voltage regulators.

Solar irradiance data of Kalaeloa, Hawaii for a summer day was downloaded from the National Renewable Energy Laboratory Measurement and Instrumentation Data Center website (NREL, 2021[92]). The irradiance data was then converted to active power output using the solar PV cell model (Jiang et al., 2020[83]), which was used in this chapter to validate the disturbance mitigation ability of the proposed controller under PV smoothing. Similar to the frequency regulation case, the obtained PV power was normalized according to the upper (sunny) and lower (cloudy) limits and then linearly projected to the operating range of compressor speed (1500 to 3500 RPM), for simplicity; practical PV smoothing control algorithms can be found in Jiang et al. (2020)[83].

Figure 7.13 depicts the resultant compressor speed and the comparison of the simulated superheat under the baseline and proposed controllers for the PV smoothing test. Compared to the frequency regulation service, PV smoothing requires more aggressive modulation of the compressor speed between the upper and lower limits, to smooth out the net generation against passing clouds. It can be seen that the superheat under the traditional PI controller underwent very significant fluctuations and 4 wet compressions were experienced within this 40-min test period. The longest wet compression occurred at around 1500 s after a sudden drop of PV power availability and lasted for over 5 minutes. In contrast, the proposed controller could attenuate the oscillation of superheat and successfully prevented wet compression throughout the whole simulation period.

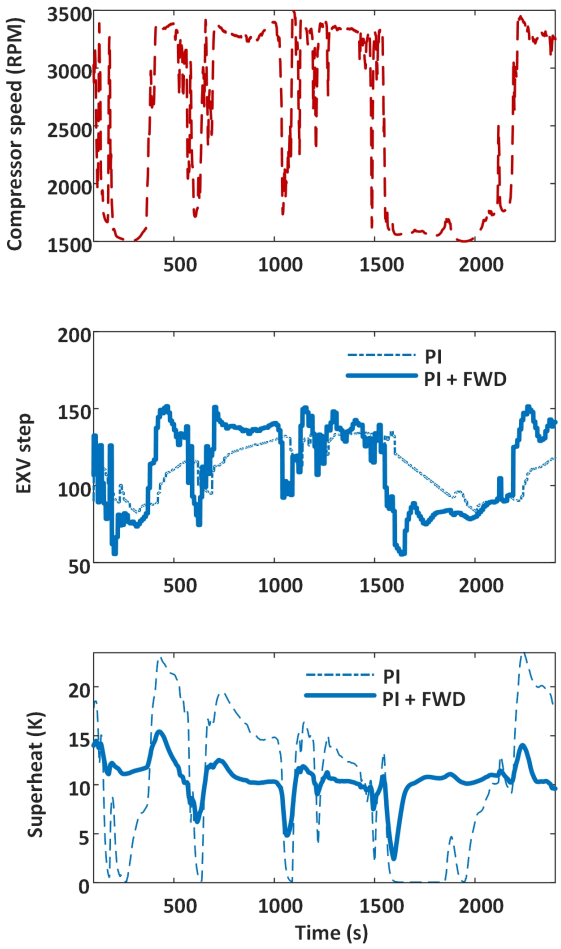

Figure 7.13: Simulation results under PV smoothing test.

7.3.2 Experimental Validation

The proposed control strategy was experimentally validated for the worst-case scenario, i.e., the case with step changes in the compressor speed. To enable cross comparison with simulation results, the boundary conditions and control settings were kept the same as the simulation counterpart, described in Section 7.3.1, during the experiments.

Figure 7.14 depicts the experimental results under a compressor speed ramp-down. Similar behaviors were observed: the superheat under the conventional PI controller dropped to and remained at 0K for several minutes after the sudden compressor speed drop, while the

superheat of the proposed controller was maintained positive, with complete avoidance of wet compression, and came back to its setpoint much faster. For the compressor ramp-up case shown in Figure 7.15, the superheat associated with the PI control underwent a significant overshoot and then slowly approached the setpoint. This caused system efficiency degradation as shown in the third subplot. On the other hand, the proposed controller could take immediate counteracting actions resulting in much improved superheat regulation performance with less oscillations and higher COP.

Although the general trends of the experimental results match those of the simulation test results presented in Section 7.3.1, small discrepancies can be noticed. Model inaccuracy can be a major contributor as model calibration had been conducted more than eight months prior to the experiments of this study, and system performance degradation and sensor drifts may have occurred during this period. Communication and control delays could also cause mismatch in the system dynamics. Despite of the discrepancy, the obtained control performance is consistent.

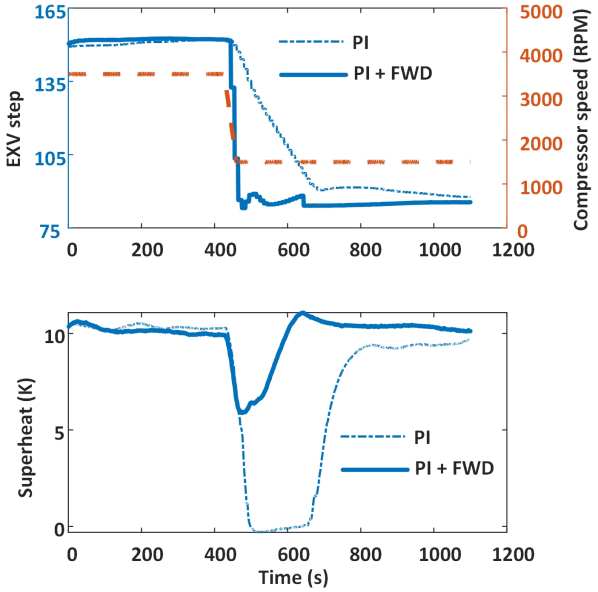

Figure 7.14: Experimental results for compressor speed ramp-down test.

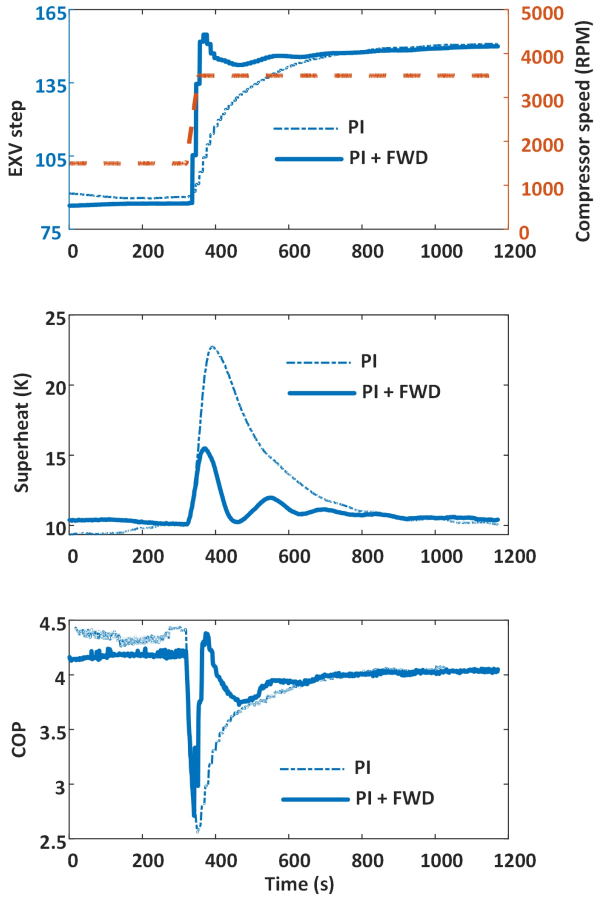

Figure 7.15: Experimental results for compressor speed ramp-up test.

7.4 Chapter Summary

Stable superheat regulation is crucial for safe and efficient operations of a VCS. However, provision of fast load balancing services, the demand of which has seen fast growth in recent years driven by the increased renewable energy deployment, creates operational challenges for a VCS. This is the first study of its kind in reporting experimental evidence and developing a control strategy for mitigation of the disturbance effect associated with provision of fast power ancillary services. This chapter presented a new gain-scheduled feedforward + PI control strategy, which incorporates a feedforward mechanism to provide immediate compensating actions to offset the disturbance effect. The proposed superheat

control strategy was validated with both simulations and experiments. The simulation validation included performance assessments under three load balancing scenarios, namely, step ramp-up/-down of compressor speed, fast frequency regulation and PV smoothing. Wet compression was present under the traditional PI control in all three numerical test cases, while much improved superheat regulation performance was demonstrated with the proposed control approach, including complete avoidance of wet compression, fast return to the setpoint and higher system efficiency. The experimental tests consolidated the findings from the numerical studies and further proved the efficacy of the proposed controller.

The dynamic VCS model developed in Chapter 5 was leveraged in this chapter to facilitate design and validation of the improved superheat control strategy. However, for practical control implementation, such a model is not required and the proposed controller can be synthesized with the aid of system identification techniques along with historical operation data. To reduce the training data requirement, the control structure could be simplified assuming a constant feedforward gain. This simplified control structure was also evaluated as part of this study and was found to be capable of eliminating wet compression for all the test cases, although its disturbance rejection performance was not as satisfactory as the full controller. The overall approach proposed in this chapter is applicable to general VCS including air-conditioning, heat pump and refrigeration systems.

Chapter 8: Zero-Superheat and Active Charge Control Enabled by Accumulator Liquid-Level Estimation

This chapter presents another application of developed gray box dynamic model in controller design. Specifically, the dynamic model has been leveraged in development of an accumulator liquid level estimator, based on which zero-superheat control and active charge control can be achieved. This chapter presents a "virtual" accumulator liquid level detection technique, based on nonlinear state observers. Then the zero-superheat and active charge control strategies, enabled by the liquid level detector, are introduced and their effectiveness in enhancing system efficiency is demonstrated through simulation and experimental tests.

8.1 Control-Oriented Dynamic VCS Model

This section introduces two dynamic models: a low-order dynamic model for the evaporator and accumulator set that is used in the liquid level estimator (referred to as control model), and a high-fidelity VCS model in support of simulation-based assessments of the proposed estimation and control strategies. The latter is a simple extension of the dynamic VCS model presented in Chapter 5, with addition of an accumulator model, and will be referred to as plant model in this chapter. The low-order model is simplified from the original dynamic model and only includes the sub-models for the evaporator and accumulator. The high-fidelity plant model purely serves as a simulation testbed for the proposed liquid level detection technique and superheat and active charge control strategies, and is not needed in control implementation. In the simulation tests, the key operational variables simulated by the plant model are fed to the liquid level detector and controller for real-time control

decision making, while in actual control implementation (e.g., experimental tests discussed in Section 8.4.2), physical sensor readings should be used.

8.1.1 Low-Order Model for State Estimation

The low-order control model used for state estimation captures the dynamics of the evaporator and accumulator. The dynamic model of the evaporator has been presented in Section 5.2.2, while the model for accumulator is elaborated in the following section. Note that condenser dynamics contribute no additional information for detection of refrigerant liquid level in the accumulator, and therefore no condenser sub-model is involved in the control model.

Accumulator Model

A few assumptions are made for modeling of the accumulator:

- There is no heat gain along the refrigerant line connecting the evaporator and accumulator, i.e., the enthalpy of the accumulator inlet equals that of the evaporator outlet h_N, as this tube section is typically well insulated;
- Outlet enthalpy of the accumulator h_{out} equals the compressor suction enthalpy.
- The heat transfer between the accumulator and its surrounding environment is neglected.

The conservation differential equations for mass and energy of the refrigerant inside

the accumulator are

$$\left(\frac{\mathrm{d}\rho_g}{\mathrm{d}P_e}V_g + \frac{\mathrm{d}\rho_f}{\mathrm{d}P_e}V_f\right)\frac{\mathrm{d}P_e}{\mathrm{d}t} + \left(\rho_f - \rho_g\right)\frac{\mathrm{d}V_f}{\mathrm{d}t} = m_{acc} - m_{comp} \tag{8.1}$$

$$\left(\frac{\mathrm{d}\left(\rho_g u_g\right)}{\mathrm{d}P_e}V_g + \frac{\mathrm{d}\left(\rho_f u_f\right)}{\mathrm{d}P_e}V_f\right)\frac{\mathrm{d}P_e}{\mathrm{d}t} + \left(\rho_f u_f - \rho_g u_g\right)\frac{\mathrm{d}V_f}{\mathrm{d}t} = m_{acc}h_N - m_{comp}h_{out} \tag{8.2}$$

where ρ_g (u_g or V_g) and ρ_f (u_f or V_f) are the gas-phase and liquid-phase refrigerant density (specific internal energy or volume in the accumulator), respectively. m_{acc} and m_{comp} are the refrigerant mass flow rates entering the accumulator and the compressor, respectively. The accumulator outlet enthalpy h_{out} is determined by the rules shown in Table 8.1 (Cheung and Braun, 2014[93]).

Table 8.1: Outlet refrigerant state for the accumulator

Accumulator inlet state	**Liquid level of accumulator**	**Outlet state**
Two phase	Not full	Saturation vapor
	Full	Saturated liquid (“wet compression”)
Superheated phase	Empty	Superheated vapor
	Non empty	Saturation vapor

Assuming the total volume of the accumulator is V_{acc}, then $V_{acc} = V_g + V_f$. Using the relationship between the refrigerant specific internal energy and enthalpy ($u = h - \frac{P}{\rho}$), the conservation equations can be reformulated as

$$\begin{bmatrix} \frac{\mathrm{d}\rho_g}{\mathrm{d}P_e}\left(V_{acc} - V_f\right) + \frac{\mathrm{d}\rho_f}{\mathrm{d}P_e}V_f & \rho_f - \rho_g \\ \left(h_g\frac{\mathrm{d}\rho_g}{\mathrm{d}P_e} + \rho_g\frac{\mathrm{d}h_g}{\mathrm{d}P_e}\right)\left(V_{acc} - V_f\right) + \left(h_f\frac{\mathrm{d}\rho_f}{\mathrm{d}P_e} + \rho_f\frac{\mathrm{d}h_f}{\mathrm{d}P_e}\right)V_f - V_{acc} & \rho_f h_f - \rho_g h_g \end{bmatrix}\begin{bmatrix} \dot{P}_e \\ \dot{V}_f \end{bmatrix} = \begin{bmatrix} m_{acc} - m_{comp} \\ m_{acc}h_N - m_{comp}h_{out} \end{bmatrix} \tag{8.3}$$

where h_g and h_f are the gas-phase and liquid-phase refrigerant enthalpy, respectively.

The adiabatic assumptions above may cause discrepancies between the control model and actual equipment dynamics (e.g., caused by insulation degradation over time). However, the proposed liquid level detection technique is insusceptible to model inaccuracies as the state observer is able to tolerate model imperfection at the expense of slightly biased state estimations. The accumulator used in the test unit has a design capacity of 2.45 L and a maximum allowed pressure of 3.06×10^6 Pa.

Integrated Low-Order (Control) Model

Let m_{exv} be the refrigerant mass flow through the EXV (or evaporator inlet flow), which relates to the accumulator inlet flow m_{acc} via the following equation

$$\begin{aligned} m_{acc} &= m_{exv} - \left(\dot{m}_{e,1} + \cdots + \dot{m}_{e,N}\right) = m_{exv} - \\ &\left[V_1\left(\frac{\partial \rho_1}{\partial P_e}\dot{P}_e + \frac{\partial \rho_1}{\partial h_1}\dot{h}_1\right) + \cdots + V_N\left(\frac{\partial \rho_N}{\partial P_e}\dot{P}_e + \frac{\partial \rho_N}{\partial h_N}\dot{h}_N\right)\right] \end{aligned} \tag{8.4}$$

where N is the number of control volumes in the evaporator.

By combining the governing equations for the evaporator and accumulator, an inte-

grated state-space formulation can be obtained for the evaporator and accumulator set:

$$\tilde{\mathbf{Z}}\underbrace{\begin{bmatrix}\dot{P}_e\\ \dot{h}_1\\ \vdots\\ \dot{h}_N\\ \dot{T}_{w,1}\\ \vdots\\ \dot{T}_{w,N}\\ \dot{V}_f\end{bmatrix}}_{\dot{\mathbf{x}}} = \underbrace{\begin{bmatrix} m_{exv}\left(h_{in}-h_1\right)+\alpha_{r,1}A_{i,1}\left(T_{w,1}-T_{r,1}\right)\\ \vdots\\ m_{exv}\left(h_{N-1}-h_N\right)+\alpha_{r,N}A_{i,N}\left(T_{w,N}-T_{r,N}\right)\\ m_{exv}-m_{comp}\\ \alpha_{a,1}A_{o,1}\left(T_{eai}-T_{w,1}\right)-\alpha_{r,1}A_{i,1}\left(T_{w,1}-T_{r,1}\right)\\ \vdots\\ \alpha_{a,N}A_{o,N}\left(T_{a,N}-T_{w,N}\right)-\alpha_{r,N}A_{i,N}\left(T_{w,N}-T_{r,N}\right)\\ m_{exv}h_N-m_{comp}h_{out}\end{bmatrix}}_{g(\mathbf{x},\mathbf{u})} \Rightarrow \begin{aligned}\dot{\mathbf{x}} &= \hat{g}\left(\mathbf{x},\mathbf{u}\right)\\ &= \tilde{\mathbf{Z}}^{-1}g\left(\mathbf{x},\mathbf{u}\right)\end{aligned} \tag{8.5}$$

where $\mathbf{x}$ is the vector of state variables, $\mathbf{u}$ is the vector of inputs (i.e., $\left[m_{exv}, m_{comp}, h_{in}, T_{eai}, m_a\right]$), T_{eai} is the evaporator air inlet temperature, m_a is the evaporator air mass flow rate, h_{in} is the refrigerant enthalpy at evaporator inlet, and $\tilde{\mathbf{Z}}$ is the transformation matrix that is dependent on the evaporation pressure and refrigerant enthalpy of each control volume. The detailed structure of the matrix can be found in Appendix A. This low-order control model for the evaporator and accumulator set is used in the accumulator liquid level estimation and it differs from the high-fidelity plant model (discussed in the next section) in the small number of control volumes for reduced computational demand.

8.1.2 High-Fidelity Model for the Simulation Testbed

The high-fidelity dynamic VCS model, serving as a simulation testbed in this chapter, is an simple extension of the dynamic model developed in Chapter 5. The major extension is the inclusion of the accumulator model presented in Section 8.1.1 between the evaporator and compressor. The experimental tests involved in the preceding chapters always has a positive superheat with an empty accumulator. That is why the original model described in Chapter 5

does not include any accumulator component model. In this chapter, the accumulator model described in Section 8.1.1 was added to the system-level dynamic model.

Figure 8.1 shows the schematics of the high-fidelity and low-order control models. To seek a trade-off between the model accuracy and computational efficiency, in the case study, the high-fidelity system model assumes 20 control volumes for both the evaporator and condenser with a simulation time step of 0.01 s (the same settings as Chapter 5). In contrast, the low-order evaporator and accumulator model used for state estimation assumes 5 control volumes with a 0.05 s simulation time step, to reduce computation burden and accommodate real-time implementation. Note that the low-order control model assumes the same heat transfer correlations (both air- and refrigerant-side) as those involved in the high-fidelity model. In practice, these correlations can be estimated on the fly with field data following the method described in Chapter 4. In the simulation tests, the high-fidelity model serves as an emulator of actual systems and the simulated operational variables are used as "measurements" to be fed to the state estimator discussed next.

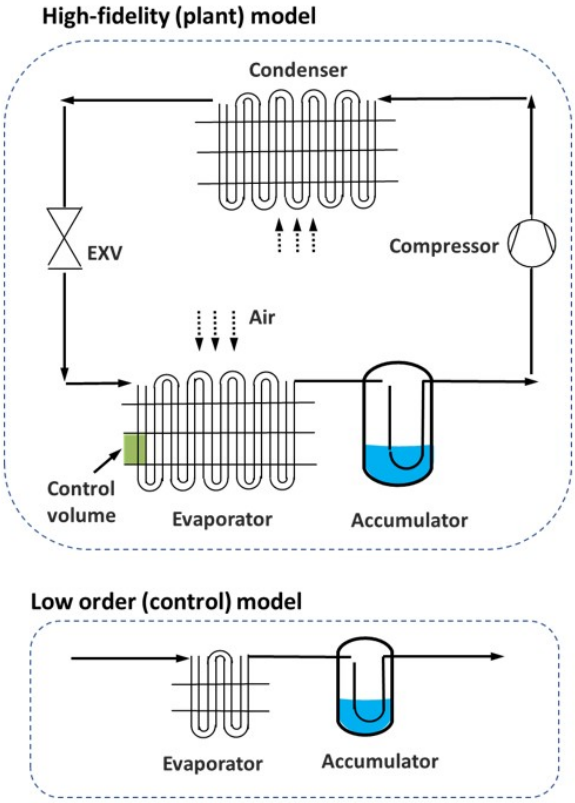

Figure 8.1: Schematics of the high-fidelity model and the low order model.

8.2 Accumulator Liquid Level Estimator

The accumulator refrigerant liquid volume V_f, as a state variable of the evaporator-accumulator control model, can be estimated along with other state variables when input/output measurements are available. The required measurements for the accumulator liquid volume detection includes the evaporating pressure P_e, refrigerant enthalpy at the evaporator inlet h_{in}, evaporator inlet air temperature T_{eai} and mass flow rate m_a, and refrigerant mass flow rates through the EXV (m_{exv}) and compressor (m_{comp}). Since the evaporating pressure P_e is very often monitored in modern air-conditioning and refrigeration systems, its reading obtained at the evaporator outlet is used as the measurable output variable. When measurements of other operational variables are available, multiple outputs can be used to improve the state estimation accuracy. The input variables, namely $m_{exv}, m_{comp}, h_{in}, T_{eai}$ and

m_a, are directly measurable or can be estimated through virtual sensing. Specifically, h_{in} can be measured through pressure and temperature readings at the condenser outlet. The refrigerant mass flow through the EXV and compressor can be estimated with their characteristic curves (e.g., see the methods described in Section 4.2.3 and 5.2.1). The evaporator airflow can be inferred from the fan curve while the thermostat temperature can be a proxy for the evaporator inlet air temperature.

Assuming that the evaporator-accumulator's dynamics are subjected to the following discrete-time state-space equations with additive noises

$$\mathbf{x}_{k+1} = f\left(\mathbf{x}_k, \mathbf{u}_k\right) + \mathbf{w}_k \tag{8.6}$$

$$y_k = \mathbf{h}^\top \mathbf{x}_k + v_k \tag{8.7}$$

where $f(\cdot)$ is the discrete-time counterpart of $\hat{g}(\cdot)$, k indicates the time step, $\mathbf{w}_k$ is the process noise subject to a zero-mean normal distribution with a covariance matrix $\mathbf{Q}$, and v_k is the output noise, also assumed to follow a zero-mean Gaussian with a variance R. Since the measured output y is the evaporation pressure P_e, the vector $\mathbf{h}$, which relates the state variables and output, has its first element being unity and all other elements being zero. State estimation can be achieved with the extended Kalman filter, an extension of the classic Kalman filter for nonlinear systems (Hoshiya and Saito, 1984[94]), which estimates the state variables with two sequential steps: next-time-step prediction and update with current output measurement.

Step-ahead predict: Given the input vector and *a posteriori* estimate of the state variable ($\hat{\mathbf{x}}_k$) at the current time step, the next-step states can be predicted with

$$\hat{\mathbf{x}}_{k+1}^{-} = f\left(\hat{\mathbf{x}}_k, \mathbf{u}_k\right) \tag{8.8}$$

which is the *a priori* state estimate at the $(k+1)^{\text{th}}$ time step given knowledge of the process

prior to step $k+1$. Equation 8.6 can be linearized locally as

$$\mathbf{x}_{k+1} \approx \hat{\mathbf{x}}_{k+1}^{-} + \mathbf{A}_k \left(\mathbf{x}_k - \hat{\mathbf{x}}_k\right) + \mathbf{w}_k \tag{8.9}$$

where $\mathbf{A}_k$ is the Jacobian matrix of $f(\cdot)$ with respect to $\mathbf{x}$, i.e.,

$$\mathbf{A}_{k,[i,j]} = \left.\frac{\partial f_{[i]}}{\partial \mathbf{x}_{[j]}}\right|_{\hat{\mathbf{x}}_k, \mathbf{u}_k} \tag{8.10}$$

where i and j are the row and column indices. The prediction step also projects the (*a priori*) error covariance for the next time step with

$$\mathbf{P}_{k+1}^{-} = \mathbf{A}_k \mathbf{P}_k \mathbf{A}_k^{\mathrm{T}} + \mathbf{Q} \tag{8.11}$$

where $\mathbf{P}_k$ is *a posteriori* estimate of the error covariance at time step k. The covariance initialization can follow the example described in Zarchan (2005)[95].

Update with measurement: When an output measurement becomes available (y_{k+1}), it can be used to correct the *a priori* estimate and obtain the *a posteriori* estimate of the state variables with

$$\hat{\mathbf{x}}_{k+1} = \hat{\mathbf{x}}_{k+1}^{-} + \mathbf{K}_{k+1}\left(y_{k+1} - \mathbf{h}\hat{\mathbf{x}}_{k+1}^{-}\right) \tag{8.12}$$

where $\mathbf{K}_{k+1}$ is the Kalman gain that minimizes the error covariance:

$$\mathbf{K}_{k+1} = \mathbf{P}_{k+1}^{-}\mathbf{h}^{\mathrm{T}}\left(\mathbf{h}\mathbf{P}_{k+1}^{-}\mathbf{h}^{\mathrm{T}} + R\right)^{-1}. \tag{8.13}$$

The state covariance is updated with

$$\mathbf{P}_{k+1} = \left(\mathbf{I} - \mathbf{K}_{k+1}\mathbf{h}\right)\mathbf{P}_{k+1}^{-}. \tag{8.14}$$

Figure 8.2 depicts the implementation diagram of the state estimator. This chapter uses naive estimates of the process noise covariance matrix **Q** and output variance R based on the respective sensor uncertainties. In practical implementations, more realistic estimates can be obtained through analysis of historical operation data, e.g., using the autocovariance least-squares technique (Rajamani and Rawlings, 2009[96]) .

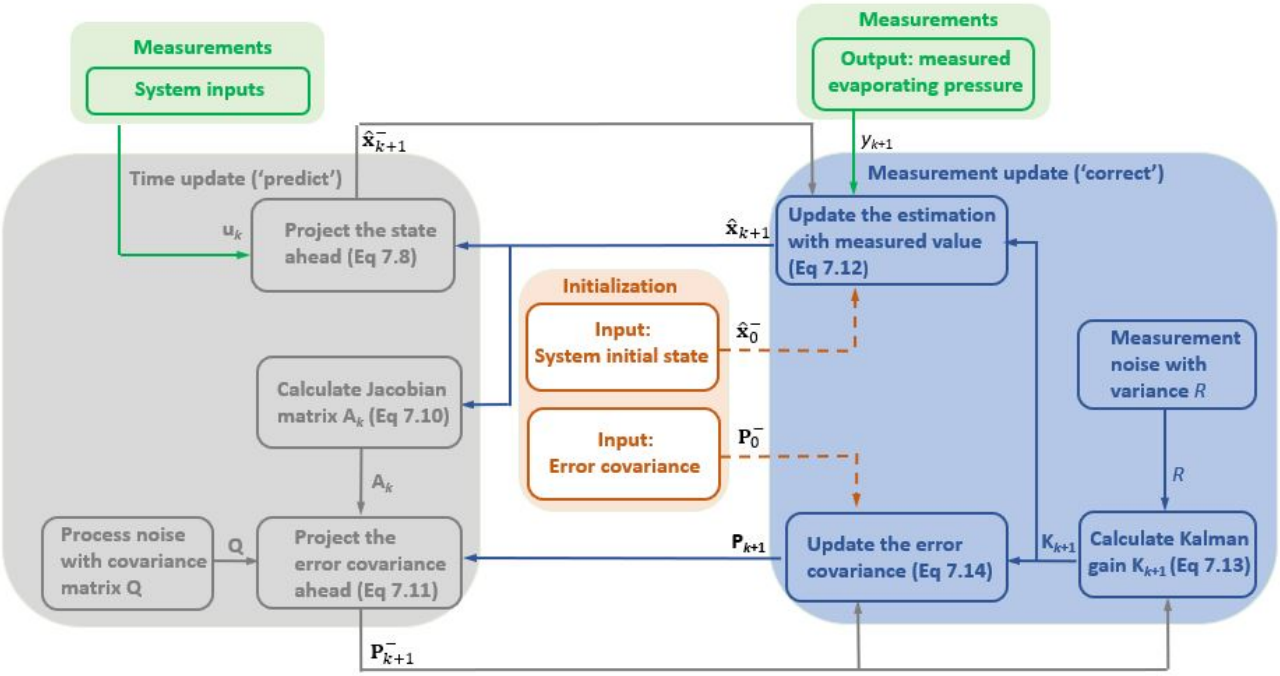

Figure 8.2: Implementation diagram of the state estimator.

8.3 Zero-Superheat and Active Charge Control

This section describes the zero-superheat and dynamic charge control strategies that can be enabled by the accumulator liquid level estimator.

8.3.1 Zero-Superheat Control

It is widely known that lower superheat settings can improve the system COP (Chen et al., 2002[27], Jensen and Skogestad, 2007[48], etc), but excessively low superheat may cause

control instability and even wet compression that can result in compressor damages. When a suction accumulator is present, a zero superheat setting can be implemented to achieve the maximum efficiency with flooded evaporators, but leads to loss of visibility of the refrigerant status at the evaporator outlet and if the accumulator is completely filled, the compressor will be flooded by pure liquid refrigerant which is disastrous. The proposed accumulator liquid level estimator can fill the visibility gap by affording real-time estimate of the refrigerant liquid level and support a zero-superheat controller to ensure operation safety. In practical implementations, a near-zero superheat setpoint can be used (e.g., 1K in the case study) and the estimated accumulator liquid level can be used to ensure the accumulator is never completely filled. When active charge control is enabled, the zero-superheat condition is automatically satisfied.

8.3.2 Active Charge Management

For overcharged systems, the rise of refrigerant mass flow can cause the increase of compressor power consumption and may cause wet compression and jeopardize system reliability. On the other hand, undercharged systems have reduced cooling capacity and degraded system energy efficiency with high superheat. Maintaining an optimum refrigerant charge level is critical to achieve maximum operation efficiency and reliability. Previous studies (Choi and Kim, 2002[43], Kim and Braun, 2012[45], Poggi et al.,, 2008[97]) have revealed concave relationships between the charge level and system COP and the existence of an optimal charge achieving the maximum system COP. However, the charge-COP curve and the optimal charge level vary with operating conditions, especially with the outdoor temperature. The accumulator can serve as a refrigerant reservoir and with proper control, can enable dynamic active charge management, for which real-time estimation of the accumulator liquid level is a prerequisite.

To evaluate the charge-COP relationship of the case study unit, the high-fidelity sim-

ulation testbed described in Section 8.1.2 was run for different ambient temperatures, with the boundary conditions presented in Table 8.2. The test rig has an oversized air duct (21 in $\times$ 21 in with a total length of approximately 30 ft) and that is why the supply airflow at the full fan speed is higher than what would be seen in field installations. For each simulation test, all the boundary conditions were held constant within a 20-min time window to ensure the system reached steady states by the end of each test (for most cases, steady states could be reached within 5 min). For all the simulation tests, a PI controller was used to modulate the EXV opening to maintain a 1K superheat setpoint. Figure 8.3 depicts the variation of the steady-state system COP with the ambient temperature and charge level. It can be observed that for a given ambient temperature (T_{cai}), the COP peaks at an intermediate charge level, and the optimal charge level, highlighted in Figure 8.3, varies and exhibits a positive correlation with the outdoor temperature, which indicates efficiency improvement potentials for dynamic charge management. Specifically, assume the system is charged with 6.4 lbs of refrigerant, which is the optimal charge level for a nominal ambient temperature $T_{cai} = 308$K; when the ambient temperature drops to 298K, the system becomes overcharged (relative to the optimal charge of 5.35 lbs at the ambient temperature of 298K) and to achieve the maximum operation efficiency during the low temperature hours, the accumulator should store 1.05 lbs (the difference of charge level between $T_{cai} = 308$K and $T_{cai} = 298$K) of refrigerant. To achieve dynamic charge control, the EXV can be modulated using a PI controller to maintain the estimated accumulator liquid level on the desired setpoint. Note that the optimal active charge level (equivalently optimal accumulator liquid level) can be determined using a look-up table developed offline or with online optimization techniques such as ESC (Koeln and Alleyne, 2014[49]); finding the optimal active charge is not a focus of this chapter. A simple look-up table approach is adopted: the results presented in Figure 8.3 were utilized to compile a table that identifies the optimal charge against each simulated outdoor temperature; in control implementation, for a given outdoor temperature, the corresponding charge level is applied in determining the optimal accumulator liquid level setpoint.

Table 8.2: Parametric analysis boundary conditions

Operating variables	Indoor temperature (K)	Outdoor temperature (K)	Compressor speed (RPM)	Evaporator air flow rate (CFM)
Setting	298	298, 303, 308, 313	4000	1600

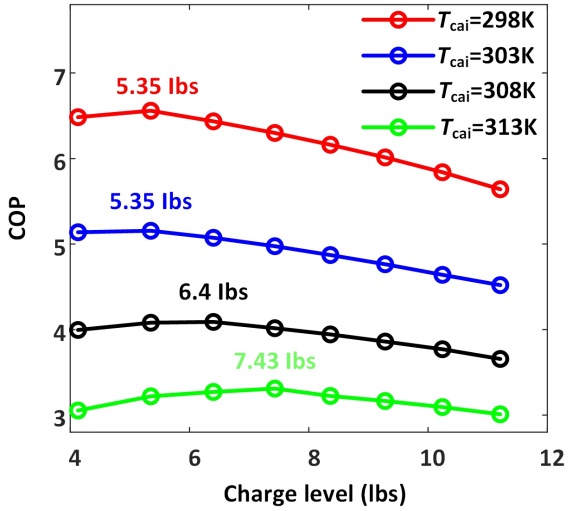

Figure 8.3: Variation of COP with respect to refrigerant charge level.

Figure 8.4 shows a block diagram of the control sequence for the proposed strategies. The controller will receive two control setpoints, the superheat setpoint $T_{sh,s}$ and the accumulator liquid level setpoint $V_{f,s}$ and only one of the two can be non-zero. When the superheat setpoint is non-zero, the accumulator will be empty and a PI controller will modulate the EXV opening to maintain the desired superheat. If the liquid level setpoint is non-zero, another PI controller, with different PI gain settings, is enabled to adjust the EXV opening to regulate the estimated liquid level around its setpoint where superheat is always zero.

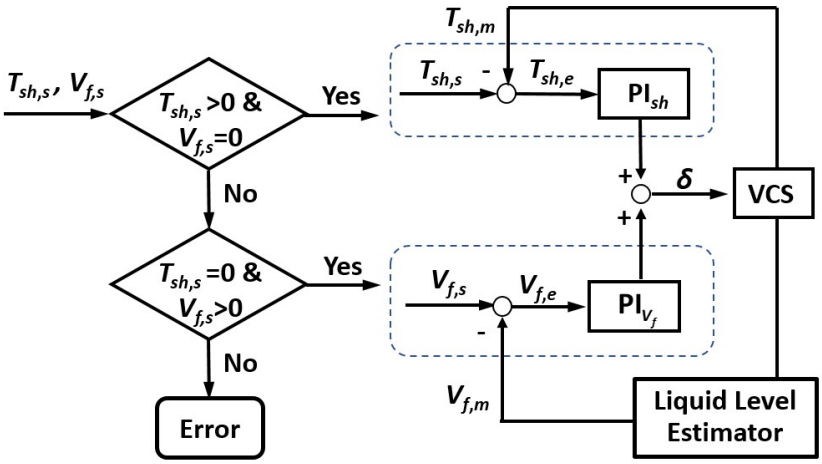

Figure 8.4: Block diagram of the proposed superheat and active charge control strategy.

8.4 Control Performance Validation

8.4.1 Simulation-Based Validation

The accumulator liquid level estimator and the zero-superheat and dynamic charge control strategies were first tested with the high-fidelity simulation testbed described in Section 8.1.2. It is assumed that the system is charged with 6.4 lbs of refrigerant (optimal charge for T_{cai} = 308K). The boundary conditions were maintained constant in the simulation tests following the settings shown in Table 8.2 while T_{cai} was fixed to 298K. Based on the analysis of Section 5.3.2, the accumulator should store 1.05 lbs of refrigerant to ensure maximum efficiency. The simulation test was divided into two stages, with the first stage assessing the COP improvement potential of zero-superheat control and the second stage demonstrating the performance of the active charge management strategy. Figure 8.5 shows the simulation test results. The numbers in the first subplot are the averaged COP over manually selected time periods when steady states were reached. The averaging time windows are also highlighted.

Zero-Superheat Control

The P/I gain settings of the OEM superheat controller were recovered through offline tests of the EXV, which were determined to be approximately 2 (Step K^{-1}) and 0.01 (Step K^{-1} sec^{-1}), respectively, and used in the simulation test. The test was started with a superheat setpoint of 10K, which was maintained until the system reached steady state at time 1000 s (see Figure 8.5). Then the superheat setpoint was reduced to 1K while all boundary conditions and control settings were kept unchanged. A low but non-zero setpoint (1 K) was used to ensure system controllability. The simulated system COP underwent a noticeable increase (approximately 8%) with the superheat descent from 10K to 1K, while the accumulator liquid level was zero throughout the first stage (the first 2000 s when the superheat was positive and no liquid refrigerant entered the accumulator).

Active Charge Control

Based on the analysis of Section 8.3.2, the accumulator should hold 1.05 lbs of refrigerant to ensure that the system operates under maximum efficiency. The accumulator in the test unit has a total internal volume V_{acc} of 2.45 L, and the liquid volume of refrigerant in the accumulator can be estimated with

$$\rho_g \left(V_{acc} - V_f\right) + \rho_f V_f = M_{acc} \Rightarrow V_f = \frac{M_{acc} - \rho_g V_{acc}}{\rho_f - \rho_g} \tag{8.15}$$

where M_{acc} is the desired mass of refrigerant held by the accumulator, i.e., 1.05 lbs. The corresponding accumulator liquid volume is V_f =0.33 L under a nominal evaporation pressure of 1×10^6 Pa.

During the second-stage test, the control strategy switched to the active charge management mode where the regulation variable changed to the estimated refrigerant liquid vol-

ume inside the accumulator. Due to the different dynamics between EXV opening and accumulator liquid volume, different PI control gain settings were identified using offline open-loop simulation tests and adopted in the charge control mode. The second-stage test started at time 2000 s with a positive superheat of 1K and an empty accumulator (see Figure 8.5). When the active charge control mode was enabled, the estimated accumulator liquid volume was zero and below its setpoint of 0.33 L, which drove the EXV to open up allowing more refrigerant flow to the evaporator; this resulted in disappearance of the superheated region and liquid refrigerant entering the accumulator. The EXV opening was modulated until the accumulator liquid level settled around the setpoint of 0.33 L. The results show a satisfactory agreement between the estimated and actual liquid volume which proves the ability of the state observer approach for accurate estimation of the accumulator liquid volume. With the active charge control, the system COP was boosted by another 2.5% compared to the 1 K superheat case in the first stage test.

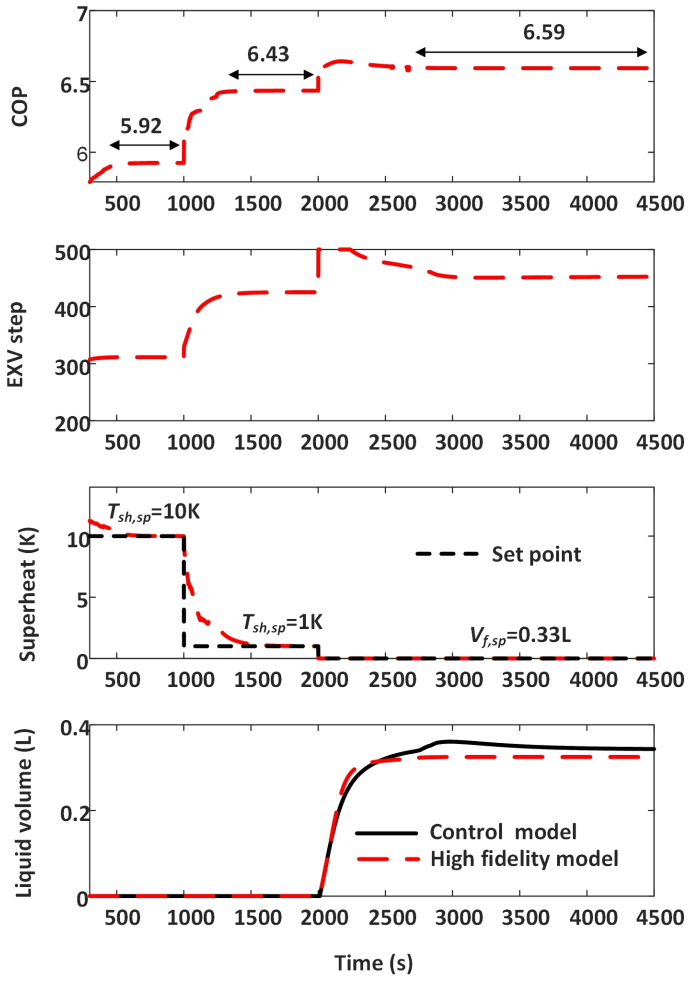

Figure 8.5: Simulation-based validation results of the estimation and control strategy.

8.4.2 Experimental Validation

Experimental tests were carried out to validate the efficiency improvement potential of the zero-superheat control strategy. All boundary conditions and control settings were kept identical to those involved in the simulation test. Simulations were also carried out with the high-fidelity model to demonstrate the accuracy of the model compared to actual system responses, where the measured boundary conditions were used in the simulations. Note that the charge level of the high-fidelity dynamic model was calibrated in advance with the experimental data by matching the simulated and measured subcooling, a key indicator

of refrigerant charge sufficiency.

Figure 8.6 shows the variations of the system COP, EXV opening, superheat and the simulated accumulator liquid volume. Since there is no liquid level detector in the accumulator, the ground-truth liquid level is unknown. That is why the high-fidelity simulation results are included. The experiment mainly serves to validate the efficiency improvement potential of the zero-superheat controller as no ground-truth charge level is available.

In the tests, a sequence of step changes were imposed on the superheat setpoint, from 10K to 1K with a 3K decrement each step. For each step change, the boundary conditions and control settings were held constant until the system reached steady state. It can be observed the PI controller was able to provide fast responses to the superheat setpoint perturbations and the system COP increased as the superheat was gradually reduced. Reduction of the superheat from 10K to 1K achieved a COP improvement by 6.63% in the experiment. The experimental and simulation results show a good agreement with a simulated COP improvement of 7.5%. In the end of the experiment, the EXV opening was manually increased to 385 steps which drove the superheat to zero and liquid refrigerant to enter the accumulator (liquid volume V_f increased). This has resulted in a further COP increase of 2.3%, which could be attributed to the superheat reduction from 1K to 0K and active charge management. The exact cause is unknown as the ground-truth charge and accumulator liquid level are not available. However, the experiment has successfully shown the effectiveness and performance of zero-superheat control. Note that during the active charge period, the system pressures and COP underwent minor oscillations, which could be caused by instability of the flow pattern transition in the evaporator (Nayak et al., 2003[98]) and density/thermal oscillations (Liang et al., 2011[99]).

Although the general trends of the experimental results match the simulation results depicted in Figure 8.5, some discrepancies can be noticed. The initial charge condition can be a major contributor as the simulation test assumed the optimal charge level for $T_{cai} = 308$K

(6.4 lbs), while it is difficult to determine the actual charge level of the test unit. Model inaccuracy could also contribute to the mismatch. Despite the discrepancy, consistent control performance was obtained from experimental and simulation tests.

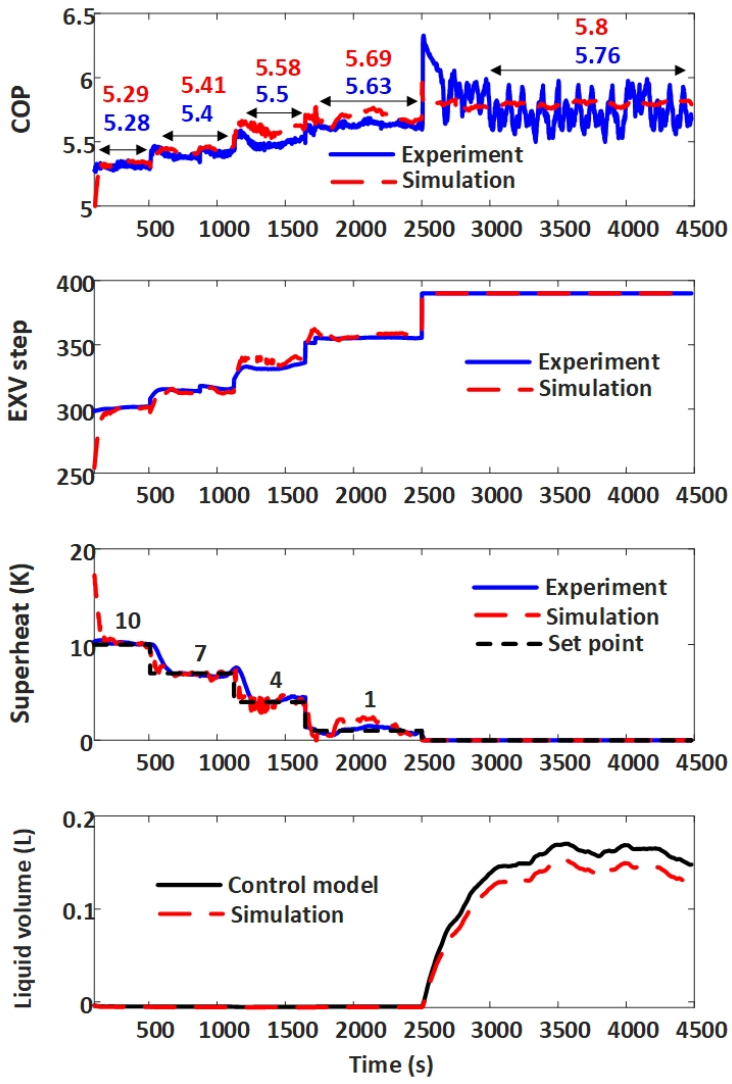

Figure 8.6: Experimental validation results for the zero-superheat controller.

8.5 Chapter Summary

This chapter presented an accumulator liquid level estimation method based on a nonlinear state observer combined with a gray-box dynamic model of the evaporator and

accumulator. This method affords a virtual liquid level detection ability from real-time readings of built-in pressure and temperature sensors in modern VCS equipment. The liquid level estimator has particular value in support of zero-superheat and active charge control strategies for energy efficiency improvement. Numerical tests have demonstrated its ability in estimation of the accumulator liquid level for the test heat pump. The numerical results also showed that 8% COP improvement could be achieved by reducing the superheat from 10K to 0K and the COP could be boosted by another 2.5% through active charge management. The experimental tests consolidated the findings from the numerical analysis and a comparable efficiency gain was observed from the zero-superheat and active charge control.

The proposed liquid level detection technique relies on other virtual sensing solutions, e.g., for the EXV and compressor mass flow rate predictions, in real-world implementation and thereby, the liquid level detection accuracy is dependent on the performance of the virtual flow sensors. It is assumed that equipment manufacturers provide such virtual sensing capability, e.g., with the aid of compressor mass flow maps. The actual virtual sensing accuracy may degrade due to deviations from design performance over time. Continuous self-calibration, e.g., through cross comparison of the compressor and EXV mass flow rates under steady-state operation, can help mitigate virtual sensing degradation. In addition, the proposed liquid level detection technique can tolerate model or virtual sensing inaccuracies through state estimations.

Chapter 9: Summary and Future Work

9.1 Summary

This dissertation starts with presentation of a reliable and robust gray-box steady-state modeling methodology for DX systems equipped with variable speed compressors and fans, that can accommodate applications with limited training data. A dual step training scheme has been proposed for identification of the model, which trains the component models separately and then integrates them through continuity equations to establish a system model. To avoid potential over-parameterization issues, the methodology incorporates sensitivity analysis and de-correlating steps to identify the influential parameters to be estimated in the training process. Built on top of the steady-state model, a multi-layer gray-box dynamic modeling methodology is presented as the major contribution of this dissertation. The dynamic modeling approach transforms the established steady-state system model into a dynamic one described by state-space governing equations, in which the thermal capacitances of the heat exchanger walls are identified to capture the system transient response. The overall methodology decomposes the model estimation task into multiple layers, that can be implemented in parallel or in series, and consequently improves the model estimation efficiency and reliability. Employing a finite control volume approach for characterizing the thermal behaviors of heat exchangers, the proposed methodology has advantages including low training data requirement, high computational efficiency and superb model accuracy. Experimental validation with a 3-ton variable-speed heat pump verified that the established model can provide accurate predictions of both steady-state and dynamic behaviors under a range of operation conditions.

The developed gray-box dynamic model has been applied for various control applications:

- *Control stability analysis of digital PI controller for determination of the proper execution time step of EXV*: simulation case studies showed that the stability threshold for the PI control execution time step could change significantly, as the operating conditions and P/I control settings vary, which indicates necessity of an optimal control strategy to adapt the control execution time step with operating conditions.

- *Design and validation of improved superheat control during provision of fast power ancillary services*: a new gain-scheduled feedforward + PI control strategy, which incorporates a feedforward mechanism to provide immediate compensating actions to offset the disturbance effect associated with fast balancing control, has been designed and tested with the dynamic model. Much improved superheat regulation performance was demonstrated with the proposed control approach, including complete avoidance of wet compression, fast return to the setpoint and higher system efficiency.

- *Zero-superheat and active charge control*: a "virtual" accumulator liquid level detection technique based on a nonlinear state observer combined with the gray-box dynamic model of the evaporator and accumulator is presented. The liquid level estimator can be combined with zero-superheat and active charge control to maximize the system efficiency. Numerical and experimental tests showed up to 10% efficiency improvement.

9.2 Future Work

Work presented in this dissertation can be extended in several directions:

- The presented model identification methodology is passive in the sense that the control settings are not proactively manipulated in the data collection phase. Optimal experimental design (OED) techniques can be leveraged as part of an active identification scheme where the target system is proactively controlled to obtain the most informative training data. The application of OED to VCS model training is worth pursuing in future work.

- The application of the established dynamic model for digital control stability analysis has shown that the stability threshold for the PI control execution time step could change significantly with the operating conditions and P/I control settings vary. This findings indicate promises of an improved strategy that adapt the control execution time step with the operating conditions to reduce control actuation and prolong the equipment lifetime.

- Active refrigerant charge management requires virtual detection of the accumulator liquid level. This study relies on an EKF which is a computationally demanding step and the non-differentiability of the control model, caused by phase transitions in the evaporator, may cause sub-optimal performance with frequent chattering of the linearized dynamics. An alternative method is to identify a nominal linear surrogate model that recovers most of the control dynamics with minimum instability and computational burden for state estimation. Other state observers with simpler implementations, such as Luenberger observer (Ciccarella et al., 1993[100]) and sliding mode observer (Davila et al., 2005[101]), can also be explored in future studies.

- For the liquid level state estimation, the ground-truth accumulator liquid level was unknown, due to difficulties in installing liquid level detection devices on the test unit. Future work can explore better benchmarking solutions such as addition of sight glass on the accumulator.

- The lower superheat setting may cause a higher heat gain along the refrigerant lines

connecting the outdoor and indoor units. The heat gain may not be a concern for packaged systems with evaporator and compressor within a close proximity but could cause severe efficiency degradation for split systems with long connecting lines. In future work, performance of zero superheat control needs to be thoroughly analyzed with more typical line lengths and insulation levels.

- All results presented in Chapter 8 were obtained at full load conditions with compressor and fan speeds at their maximum levels. The demonstrated performance is representative for single-stage VCSs while for variable-speed equipment, the compressor and fan speeds will likely influence the optimal charge level and make the optimal charge control problem even more complicated. Although this dissertation does not address the problem of how to determine the optimal charge under dynamic operating conditions, it is a topic worth pursuing in future studies.

- The Residential Cold Climate Heat Pump Challenge, as part of the U.S. Department of Energy's Better Energy, Emissions and Equity (E3) Initiative (DOE, 2022[102]), is expected to spur increasing deployment of heat pumps nationwide. Many techniques have been proposed to address the heat pump capacity and efficiency issues at low ambient temperatures, such as the vapor injection (Wang and Li, 2019[103], Heo et al., 2010[104], Wei et al., 2020[105]) and cascade configurations (Arpagaus et al., 2016[106]) with flash tanks (Qiao et al., 2015[107]). The flash tank design opens opportunity for improved charge management that can be facilitated by the gray-box modeling technique.

Appendices

Appendix A: Transformation Matrix

The transformation matrix for the control dynamic model is:

$$\tilde{\mathbf{Z}} = \begin{bmatrix} \tilde{\mathbf{Z}}_{11} & \tilde{\mathbf{Z}}_{12} \\ \tilde{\mathbf{Z}}_{21} & \tilde{\mathbf{Z}}_{22} \end{bmatrix},$$

$$\tilde{\mathbf{Z}}_{11}^{(N+1)\times(N+1)} = \begin{bmatrix} -V_1 & V_1\rho_1 & \cdots & 0 \\ \vdots & \vdots & \ddots & \vdots \\ \left[\sum_{i=1}^{N-1} V_i \left(\frac{\partial \rho_i}{\partial P_e}\right)\right](h_{N-1} - h_N) - V_N & V_1\left(\frac{\partial \rho_1}{\partial h_1}\right)(h_{N-1} - h_N) & \cdots & V_N\rho_N \\ \sum_{i=1}^{N} V_i \left(\frac{\partial \rho_i}{\partial P_e}\right) + \frac{\mathrm{d}\rho_g}{\mathrm{d}P_e}\left(V_{acc} - V_f\right) + \frac{\mathrm{d}\rho_f}{\mathrm{d}P_e}V_f & V_1\left(\frac{\partial \rho_1}{\partial h_1}\right) & \cdots & V_N\left(\frac{\partial \rho_N}{\partial h_N}\right) \end{bmatrix},$$

$$\tilde{\mathbf{Z}}_{12}^{(N+1)\times(N+1)} = \begin{bmatrix} 0 & \cdots & 0 & 0 \\ \vdots & \ddots & \vdots & \vdots \\ 0 & \cdots & 0 & 0 \\ 0 & \cdots & 0 & \rho_f - \rho_g \end{bmatrix}, \quad \tilde{\mathbf{Z}}_{22}^{(N+1)\times(N+1)} = \begin{bmatrix} \left(C_{th,w}\right)_1 & \cdots & 0 & 0 \\ \vdots & \ddots & \vdots & \vdots \\ 0 & \cdots & \left(C_{th,w}\right)_N & 0 \\ 0 & \cdots & 0 & \rho_f h_f - \rho_g h_g \end{bmatrix},$$

$$\tilde{\mathbf{Z}}_{21}^{(N+1)\times(N+1)} =$$

$$\begin{bmatrix} 0 & \cdots & 0 \\ \vdots & \ddots & \vdots \\ 0 & \cdots & 0 \\ \left(h_g\frac{\mathrm{d}\rho_g}{\mathrm{d}P_e} + \rho_g\frac{\mathrm{d}h_g}{\mathrm{d}P_e}\right)\left(V_{acc} - V_f\right) + \left(h_f\frac{\mathrm{d}\rho_f}{\mathrm{d}P_e} + \rho_f\frac{\mathrm{d}h_f}{\mathrm{d}P_e}\right)V_f - V_{acc} + h_N\sum_{i=1}^{N} V_i\left(\frac{\partial \rho_i}{\partial P_e}\right) & \cdots & V_N h_N\left(\frac{\partial \rho_N}{\partial h_N}\right) \end{bmatrix}$$

Appendix B: Publications from This Dissertation

B.1 Journal paper

- Liu, Haopeng, and Jie Cai. "Improved superheat control of variable-speed vapor compression systems in provision of fast load balancing services." International Journal of Refrigeration 132 (2021): 187-196.
- Liu, Haopeng, Jie Cai, and Donghun Kim. "A hierarchical gray-box dynamic modeling methodology for direct-expansion cooling systems to support control stability analysis." International Journal of Refrigeration 133 (2022): 191-200.
- Liu, Haopeng, and Jie Cai. "A robust gray-box modeling methodology for variable-speed direct-expansion systems with limited training data." International Journal of Refrigeration 129 (2021): 128-138.
- Liu, Haopeng, and Jie Cai. "Development of an accumulator liquid-level estimator to enable zero-superheat control and active charge management in vapor-compression systems." International Journal of Refrigeration (accepted).

B.2 Conference paper

- Liu, Haopeng, and Jie Cai. "A Gray-Box Dynamic Modeling Method for Variable Speed Direct Expansion Systems." 18th International Refrigeration and Air Conditioning Conference at Purdue, 2021.
- Liu, Haopeng, and Jie Cai. "Development and validation of an accumulator liquid-

level estimator to enable zero-superheat and active charge control in vapor-compression systems." 19th International Refrigeration and Air Conditioning Conference at Purdue, 2022.

B.3 Presentation

- "Development and validation of an accumulator liquid-level estimator to enable zero-superheat and active charge control in vapor-compression systems",19th International Refrigeration and Air Conditioning Conference at Purdue, July 2022.
- "A Gray-Box Dynamic Modeling Method for Variable Speed Direct Expansion Systems", 18th International Refrigeration and Air Conditioning Conference at Purdue, May 2021.
- "Dynamic modeling for variable-speed HVAC system to support optimal controller design", 39th Oklahoma AIAA/ASME Symposium, The University of Tulsa, April 2019.

References

[1] J. M. Gordon and K. C. Ng, "Thermodynamic modeling of reciprocating chillers", *Journal of Applied Physics*, vol. 75, no. 6, pp. 2769–2774, 1994.

[2] H. Li and J. E. Braun, "On-line models for use in automated fault detection and diagnosis for hvacr equipment", ser. In Proceedings of the 2002 ACEEE Conference on Energy Efficiency in Buildings, Monterey, CA, 2002, pp. 147–158.

[3] M. S. Breuker and J. E. Braun, "Evaluating the performance of a fault detection and diagnostic system for vapor compression equipment", *HVACR Research*, vol. 4, no. 4, pp. 401–425, 1998.

[4] D. J. Swider, "A comparison of empirically based steady-state models for vapor-compression liquid chillers", *Applied Thermal Engineering*, vol. 23, no. 5, pp. 539–556, 2003.

[5] R. Cabello, J. Navarro, and E. Torrella, "Simplified steady-state modelling of a single stage vapour compression plant. model development and validation", *Applied Thermal Engineering*, vol. 25, no. 11-12, pp. 1740–1752, 2005.

[6] F. W. Yu and K. T. Chan, "Modelling of the coefficient of performance of an air-cooled screw chiller with variable speed condenser fans", *Building and Environment*, vol. 41, no. 4, pp. 407–417, 2006.

[7] J. Cai, "Gray-box modeling of multistage direct-expansion units to enable control system optimization", *ASHRAE Transactions*, vol. 121, p. 203, 2015.

[8] M. W. Browne and P. K. Bansal, "Steady-state model of centrifugal liquid chillers: Modèle pour des refroidisseurs de liquide centrifuges en régime permanent", *International Journal of Refrigeration*, vol. 21, no. 5, pp. 343–358, 1998.

[9] M. W. Browne and P. K. Bansal, "An elemental ntu- model for vapour-compression liquid chillers", *International Journal of Refrigeration*, vol. 24, no. 7, pp. 612–627, 2001.

[10] G. H. Lee and J. Y. Yoo, "Performance analysis and simulation of automobile air conditioning system", *International Journal of Refrigeration*, vol. 23, no. 3, pp. 243–254, 2000.

[11] J. S. Jabardo, W. G. Mamani, and M. R. Ianella, "Modeling and experimental evaluation of an automotive air conditioning system with a variable capacity compressor", *International Journal of Refrigeration*, vol. 25, no. 8, pp. 1157–1172, 2002.

[12] L. Fu, G. Ding, Z. Su, and G. Zhao, "Steady-state simulation of screw liquid chillers", *Applied Thermal Engineering*, vol. 22, no. 15, pp. 1731–1748, 2002.

[13] H. Cheung and J. E. Braun, "Simulation of fault impacts for vapor compression systems by inverse modeling. part i: Component modeling and validation", *HVACR Research*, vol. 19, no. 7, pp. 892–906, 2013.

[14] T. M. Rossi, "Detection, diagnosis, and evaluation of faults in vapor compression equipment", Ph.D. dissertation, 1995.

[15] P. Haberschill, L. Gay, P. Aubouin, and M. Lallemand, "Performance prediction of a refrigerating machine using r-407c: The effect of the circulating composition on system performance", *International Journal of Energy Research*, vol. 26, no. 15, pp. 1295–1311, 2002.

[16] D. B. Crawley *et al.*, "Energyplus: Creating a new-generation building energy simulation program", *Energy and Buildings*, vol. 33, no. 4, pp. 319–331, 2001.

[17] S. Bendapudi and J. E. Braun, "Development and validation of a mechanistic, dynamic model for a vapor compression centrifugal liquid chiller", *Report of ASHRAE*, 2002.

[18] B. P. Rasmussen, "Dynamic modeling for vapor compression systems—part i: Literature review", *HVACR Research*, vol. 18, no. 5, pp. 934–955, 2012.

[19] J. Catano, F. Lizarralde, T. Zhang, J. T. Wen, M. K. Jensen, and Y. Peles, "Vapor compression refrigeration cycle for electronics cooling–part ii: Gain-scheduling control for critical heat flux avoidance", *International Journal of Heat and Mass Transfer*, vol. 66, pp. 922–929, 2013.

[20] W. Chen and S. Deng, "Development of a dynamic model for a dx vav air conditioning system", *Energy Conversion and Management*, vol. 47, no. 18-19, pp. 2900–2924, 2006.

[21] B. Li and A. G. Alleyne, "A dynamic model of a vapor compression cycle with shutdown and start-up operations", *International Journal of Refrigeration*, vol. 33, no. 3, pp. 538–552, 2010.

[22] D. Kim, J. Ma, J. E. Braun, and E. A. Groll, "Fuzzy modeling approach for transient vapor compression and expansion cycle simulation", *International Journal of Refrigeration*, vol. 121, pp. 114–125, 2021.

[23] R. G. Kapadia, S. Jain, and R. S. Agarwal, "Transient characteristics of split air-conditioning systems using r-22 and r-410a as refrigerants", *HVACR Research*, vol. 15, no. 3, pp. 617–649, 2009.

[24] A. Beghi and L. Cecchinato, "A simulation environment for dry-expansion evaporators with application to the design of autotuning control algorithms for electronic expansion valves", *International Journal of Refrigeration*, vol. 32, no. 7, pp. 1765–1775, 2009.

[25] Z. R. Huelle, "Heat load influences upon evaporator parameters", ser. 12th International Refrigeration Congress, vol. 2, 1967, pp. 985–1002.

[26] Z. R. Huelle, "Mss line-new approach to hunting problem", *ASHRAE Journal-American Society of Heat Refrigerating and Air-conditioning Engineers*, vol. 14, no. 10, pp. 43–46, 1972.

[27] W. Chen, C. Zhijiu, Z. Ruiqi, and W. Yezheng, "Experimental investigation of a minimum stable superheat control system of an evaporator", *International Journal of Refrigeration*, vol. 25, no. 8, pp. 1137–1142, 2002.

[28] Y. Chen, S. Deng, X. Xu, and M. Chan, "A study on the operational stability of a refrigeration system having a variable speed compressor", *International Journal of Refrigeration*, vol. 31, no. 8, pp. 1368–1374, 2008.

[29] I. W. Eames, A. Milazzo, and G. G. Maidment, "Modelling thermostatic expansion valves", *International Journal of Refrigeration*, vol. 38, pp. 189–197, 2014.

[30] Y. Xia and S. Deng, "The influences of the operating characteristics of an electronic expansion valve (eev) on the operational stability of an eev controlled direct expansion air conditioning system", *International Journal of Refrigeration*, vol. 69, pp. 394–406, 2016.

[31] M. S. Elliott and B. P. Rasmussen, "On reducing evaporator superheat nonlinearity with control architecture", *International Journal of Refrigeration*, vol. 33, no. 3, pp. 607–614, 2010.

[32] Y. Xia, Q. Ding, J. S., X. Zhang, and S. Deng, "A simulation study on the operational stability of an eev-controlled direct expansion air conditioning system under variable speed operation", *International Journal of Refrigeration*, vol. 103, pp. 115–125, 2019.

[33] A. P. H. Outtagarts and M. Lallemand, "The transient response of an evaporator fed through an electronic expansion valve", *International Journal of Energy Research*, vol. 21, no. 9, pp. 793–807, 1997.

[34] M. Elliott, Z. Walton, B. Bolding, and B. P. Rasmussen, "Superheat control: A hybrid approach", *HVACR Research*, vol. 15, no. 6, pp. 1021–1043, 2009.

[35] W. Chen, Z. Xingxi, and D. Shiming, "Development of control method and dynamic model for multi-evaporator air conditioners", *Energy Conversion and Management*, vol. 46, no. 3, pp. 451–465, 2005.

[36] J. B. Marcinichen, T. N. del Holanda, and C. Melo, "A dual siso controller for a vapor compression refrigeration system", 2008.

[37] O. Ekren, S. Sahin, and Y. Isler, "Comparison of different controllers for variable speed compressor and electronic expansion valve", *International Journal of Refrigeration*, vol. 33, no. 6, pp. 1161–1168, 2010.

[38] X.-D. He, S. Liu, and H. H. Asada, "Modeling of vapor compression cycles for multivariable feedback control of hvac systems", *Journal of Dynamic Systems, Measurement, and Control*, vol. 119, no. 2, pp. 183–191, 1997.

[39] X.-D. He, S. Liu, H. H. Asada, and H. Itoh, "Multivariable control of vapor compression systems", *HVACR Research*, vol. 4, no. 3, pp. 205–230, 1998.

[40] B. P. Rasmussen and A. G. Alleyne, "Gain scheduled control of an air conditioning system using the youla parameterization", *IEEE Transactions on Control Systems Technology*, vol. 18, no. 5, pp. 1216–1225, 2009.

[41] H. Niemann and J. Stroustrup, "Gain scheduling using the youla parameterization", vol. 3, IEEE, 1999, pp. 2306–2311.

[42] M. Keir, B. Rasmussen, and A. Alleyne, "Improving energy efficiency in automotive vapor compression cycles through advanced control design", 2006.

[43] J. M. Choi and Y. C. Kim, "The effects of improper refrigerant charge on the performance of a heat pump with an electronic expansion valve and capillary tube", *Energy*, vol. 27, no. 4, pp. 391–404, 2002.

[44] M. Farzad and D. O'Neal, "The effect of improper refrigerant charging on the performance of a residential heat pump with fixed expansion devices (capillary tube and short tube orifice)", ser. Intersociety Energy Conversion Engineering Conference, 1994.

[45] W. Kim and J. E. Braun, "Evaluation of the impacts of refrigerant charge on air conditioner and heat pump performance", *International Journal of Refrigeration*, vol. 35, no. 7, pp. 1805–1814, 2012.

[46] Z. Wu and R. Du, "Design and experimental study of a miniature vapor compression refrigeration system for electronics cooling", *Applied Thermal Engineering*, vol. 31, no. 2-3, pp. 385–390, 2011.

[47] W. Yuan, B. Yang, Y. Yang, K. Ren, J. Xu, and Y. Liao, "Development and experimental study of the characteristics of a prototype miniature vapor compression refrigerator", *Applied Energy*, vol. 143, pp. 47–57, 2015.

[48] J. B. Jensen and S. Skogestad, "Optimal operation of simple refrigeration cycles: Part i: Degrees of freedom and optimality of sub-cooling", *Computers Chemical Engineering*, vol. 31, no. 5–6, pp. 712–721, 2007.

[49] J. P. Koeln and A. G. Alleyne, "Optimal subcooling in vapor compression systems via extremum seeking control: Theory and experiments", *International Journal of Refrigeration*, vol. 43, pp. 14–25, 2014.

[50] B. D. Eldredge, B. P. Rasmussen, and A. G. Alleyne, "Moving-boundary heat exchanger models with variable outlet phase", *Journal of Dynamic Systems, Measurement, and Control*, vol. 130, no. 6, pp. 1–12, 2008.

[51] J. C. Menken, T. Weustenfeld, and J. Köhler, "Experimental comparison of the refrigerant reservoir position in a primary loop refrigerant cycle with optimal operation", ser. 15th International Refrigeration and Air Conditioning Conference at Purdue, 2014.

[52] M. H. Kutner, C. J. Nachtsheim, J. Neter, and W. Li, *Applied linear statistical models*. McGraw-Hill Irwin, 2005.

[53] J. R. Donaldson and R. B. Schnabel, "Computational experience with confidence regions and confidence intervals for nonlinear least squares", *Technometrics*, vol. 29, no. 1, pp. 67–82, 1987.

[54] J. Cai, D. Kim, J. E. Braun, and J. Hu, "Optimizing zone temperature setpoint excitation to minimize training data for data-driven dynamic building models", ser. In 2016 American Control Conference (ACC), 2016, pp. 1478–1484.

[55] L. Ljung, *System identification*. Wiley encyclopedia of electrical and electronics engineering, 1999.

[56] J. Cai and J. E. Braun, "A practical and scalable inverse modeling approach for multi-zone buildings", ser. In 9th International Conference on System Simulation in Buildings, 2014, pp. 1–19.

[57] J. M. Belman, J. Navarro-Esbrí, D. Ginestar, and V. Milian, "Steady-state model of a variable speed vapor compression system using r134a as working fluid. international journal of energy research", *International Journal of Energy Research*, vol. 34, no. 11, pp. 933–945, 2010.

[58] I. H. Bell and A. Jäger, "Helmholtz energy transformations of common cubic equations of state for use with pure fluids and mixtures", *Journal of Research of the National Institute of Standards and Technology*, vol. 121, p. 238, 2016.

[59] C. C. Wang, W. L. Fu, and C. T. Chang, "Heat transfer and friction characteristics of typical wavy fin-and-tube heat exchangers", *Experimental Thermal and Fluid Science*, vol. 14, no. 2, pp. 174–186, 1997.

[60] W. Pirompugd, S. Wongwises, and C. C. Wang, "Simultaneous heat and mass transfer characteristics for wavy fin-and-tube heat exchangers under dehumidifying conditions", *International Journal of Heat and Mass Transfer*, vol. 49, no. 1-2, pp. 132–143, 2006.

[61] K. E. Gungor and R. H. S. Winterton, "A general correlation for flow boiling in tubes and annuli", *International Journal of Heat and Mass Transfer*, vol. 29, no. 3, pp. 351–358, 1986.

[62] M. M. Shah, "Chart correlation for saturated boiling heat transfer: Equations and further study", *ASHRAE Transactions*, vol. 88, 1982.

[63] D. S. Jung, M. McLinden, R. Radermacher, and D. Didion, "A study of flow boiling heat transfer with refrigerant mixtures", *International Journal of Heat and Mass Transfer*, vol. 32, no. 9, pp. 1751–1764, 1989.

[64] J. C. Chen, "Correlation for boiling heat transfer to saturated fluids in convective flow", *Industrial Engineering Chemistry Process Design and Development*, vol. 5, no. 3, pp. 322–329, 1966.

[65] T. L. Bergman, F. P. Incropera, D. P. DeWitt, and A. S. Lavine, *Fundamentals of heat and mass transfer*. New York: John Wiley Sons.

[66] D. M. Admiraal and C. W. Bullard, "Heat transfer in refrigerator condensers and evaporators", *Air Conditioning and Refrigeration Center*, 1993.

[67] T. N. Tandon, H. K. Varma, and C. P. Gupta, "A void fraction model for annular two-phase flow", *International Journal of Heat and Mass Transfer*, vol. 28, no. 1, pp. 191–198, 1985.

[68] M. M. Shah, "A general correlation for heat transfer during film condensation inside pipes", *International Journal of Heat and Mass Transfer*, vol. 22, no. 4, pp. 547–556, 1979.

[69] W. F. Stoecker, *Industrial refrigeration handbook*. New York: McGraw-Hill, 1998.

[70] E. Winandy, C. Saavedra, and J. Lebrun, "Experimental analysis and simplified modelling of a hermetic scroll refrigeration compressor", *Applied thermal Engineering*, vol. 22, no. 2, pp. 107–120, 2002.

[71] D. I. J. D. T. Reindl and P. S. A. Klein, "A semi-empirical method for representing domestic refrigerator/freezer compressor calorimeter test data", *ASHRAE transactions*, 2000.

[72] Y. Chen, N. P. Halm, E. A. Groll, and J. E. Braun, "A comprehensive model of scroll compressors part ii: Overall scroll compressor modeling", ser. 15th International Compressor Engineering Conference at Purdue, 2000, pp. 725–734.

[73] C. Willich and A. J. White, "Heat transfer losses in reciprocating compressors with valve actuation for energy storage applications", *Journal of Energy Storage*, vol. 14, pp. 322–328, 2017.

[74] H. Yu and B. M. Wilamowski, "Levenberg–marquardt training. in intelligent systems", *Intelligent Systems*, vol. 12, pp. 1–12, 2018.

[75] W. Li, "Simplified modeling analysis of mass flow characteristics in electronic expansion valve", *Applied Thermal Engineering*, vol. 53, no. 1, pp. 8–12, 2013.

[76] A. Davies and D. TC, "Single and two-phase flow of dichlorodifluoromethane,(r12), through sharp-edged orifices", 1, vol. 79, 1973, pp. 109–123.

[77] A. Gupta, "Reduced order modeling of heat exchangers using high order finite control volume models", M.S. thesis, 2007.

[78] M. D. Greenberg, *Advanced engineering mathematics*. Prentice Hall, 1988.

[79] I. D. Landau and G. Zito, *Digital control systems: design, identification and implementation*. Springer Science Business Media, 2007.

[80] M. S. Fadali and A. Visioli, *Digital control engineering: analysis and design*. Academic Press, 2013.

[81] O. Katsuhiko, *Modern control engineering*. Prentice Hall, 2010.

[82] J. Cai and J. E. Braun, "Laboratory-based assessment of hvac equipment for power grid frequency regulation: Methods, regulation performance, economics, indoor comfort and energy efficiency", *Energy and Buildings*, vol. 185, pp. 148–161, 2019.

[83] Z. Jiang, J. Cai, and P. S. Moses, "Smoothing control of solar photovoltaic generation using building thermal loads", *Applied Energy*, vol. 277, 2020.

[84] A. Elhefny, Z. Jiang, and J. Cai, "Co-simulation and energy management of photovoltaic-rich residential communities for improved distribution voltage support with flexible loads", *Solar Energy*, vol. 231, pp. 516–526, 2022.

[85] Y. Xia and S. Deng, "The influences of the operating characteristics of an electronic expansion valve (eev) on the operational stability of an eev controlled direct expansion air conditioning system", *International Journal of Refrigeration*, vol. 69, pp. 394–406, 2016.

[86] G. F. Franklin, J. D. Powell, and A. Emami-Naeini, *Feedback control of dynamic systems*. Pearson, 2015.

[87] H. Yan, Y. Xia, and S. Deng, "Adaptive control for degree of refrigerant superheat in a direct expansion air conditioning system under variable speed operation", *Energy Procedia*, vol. 158, pp. 2182–2187, 2019.

[88] Z. Zhou, T. Levin, and G. Conzelmann, "Survey of us ancillary services markets", Argonne National Lab.(ANL), Argonne, IL (United States), Tech. Rep., 2016.

[89] P. N. J. M. Interconnection, *Market-based regulation self-test signals*, https://www.pjm.com/markets-and-operations/ancillary-services.aspx.

[90] R. Tonkoski, L. A. Lopes, and T. H. El-Fouly, "Coordinated active power curtailment of grid connected pv inverters for overvoltage prevention", *IEEE Transactions on Sustainable Energy*, vol. 2, no. 2, pp. 139–147, 2010.

[91] G. Wang, M. Ciobotaru, and V. G. Agelidis, "Power smoothing of large solar pv plant using hybrid energy storage", *IEEE Transactions on Sustainable Energy*, vol. 5, no. 3, pp. 834–842, 2014.

[92] Measurement and I. D. Center, *Oahu solar measurement grid*, https://midcdmz.nrel.gov/apps/rawdata.pl?site=oahugrid;data=Oahu$_G HI; type = zipdata$.

[93] H. Cheung and J. E. Braun, "Component-based, gray-box modeling of ductless multi-split heat pump systems", *International Journal of Refrigeration*, vol. 38, pp. 30–45, 2014.

[94] M. Hoshiya and E. Saito, "Structural identification by extended kalman filter", *Journal of Engineering Mechanics*, vol. 110, no. 12, pp. 1757–1770, 1984.

[95] P. Zarchan, *Progress in astronautics and aeronautics: fundamentals of Kalman filtering: a practical approach*. Aiaa, 2005.

[96] M. R. Rajamani and J. B. Rawlings, "Estimation of the disturbance structure from data using semidefinite programming and optimal weighting", *Automatica*, vol. 45, no. 1, pp. 142–148, 2009.

[97] F. Poggi, H. Macchi-Tejeda, D. Leducq, and A. Bontemps, "Refrigerant charge in refrigerating systems and strategies of charge reduction", *International Journal of Refrigeration*, vol. 31, no. 3, pp. 353–370, 2008.

[98] A. K. Nayak, P. K. Vijayan, V. Jain, D. Saha, and R. K. Sinha, "Study on the flow-pattern-transition instability in a natural circulation heavy water moderated boiling light water cooled reactor. nuclear engineering and design", *Nuclear Engineering and Design*, vol. 225, no. 2-3, pp. 159–172, 2003.

[99] N. Liang, S. Shuangquan, C. Tian, and Y. Y. Yan, "Two-phase flow instabilities in horizontal straight tube evaporator", *Applied Thermal Engineering*, vol. 31, no. 2-3, pp. 181–187, 2011.

[100] G. Ciccarella, M. Dalla Mora, and A. Germani, "A luenberger-like observer for non-linear systems", *International Journal of Control*, vol. 57, no. 3, pp. 537–556, 1993.

[101] J. Davila, L. Fridman, and A. Levant, "Second-order sliding-mode observer for mechanical systems", *IEEE Transactions on Automatic Control*, vol. 50, no. 11, pp. 1785–1789, 2005.

[102] DOE, *Residential cold-climate heat pump technology challenge specification*, https://www.energy.gov/eere/buildings/cchp-technology-challenge-specifications, 2022.

[103] W. Wang and Y. Li, "Intermediate pressure optimization for two-stage air-source heat pump with flash tank cycle vapor injection via extremum seeking", *Applied Energy*, vol. 238, pp. 612–626, 2019.

[104] J. Heo, M. W. Jeong, and Y. Kim, "Effects of flash tank vapor injection on the heating performance of an inverter-driven heat pump for cold regions", *International Journal of Refrigeration*, vol. 33, no. 4, pp. 848–855, 2010.

[105] W. Wei, L. Ni, L. Xu, Y. Yang, and Y. Yao, "Application characteristics of variable refrigerant flow heat pump system with vapor injection in severe cold region", *Energy and Buildings*, vol. 211, p. 109 798, 2020.

[106] C. Arpagaus, F. Bless, J. Schiffmann, and S. S. Bertsch, "Multi-temperature heat pumps: A literature review", *International Journal of Refrigeration*, vol. 69, pp. 437–465, 2016.

[107] H. Qiao, X. Xu, V. Aute, and R. Radermacher, "Transient modeling of a flash tank vapor injection heat pump system–part ii: Simulation results and experimental validation", *International Journal of Refrigeration*, vol. 49, pp. 183–194, 2015.